

Program



Lunar and Planetary Institute 3600 Bay Area Boulevard Houston TX 77058-1113

Planetary Geologic Mappers Annual Meeting

June 12–14, 2018 • Knoxville, Tennessee

Institutional Support

Lunar and Planetary Institute
Universities Space Research Association

Convener

Devon Burr
Earth and Planetary Sciences Department, University of Tennessee Knoxville

Science Organizing Committee

David Williams, Chair
Arizona State University

Devon Burr
Earth and Planetary Sciences Department, University of Tennessee Knoxville

Robert Jacobsen
Earth and Planetary Sciences Department, University of Tennessee Knoxville

Bradley Thomson
Earth and Planetary Sciences Department, University of Tennessee Knoxville

Abstracts for this meeting are available via the meeting website at
<https://www.hou.usra.edu/meetings/pgm2018/>

Abstracts can be cited as

Author A. B. and Author C. D. (2018) Title of abstract. In *Planetary Geologic Mappers Annual Meeting*, Abstract #XXXX.
LPI Contribution No. 2066, Lunar and Planetary Institute, Houston.

Guide to Sessions

Tuesday, June 12, 2018

9:00 a.m.	Strong Hall Meeting Room	Introduction and Mercury and Venus Maps
1:00 p.m.	Strong Hall Meeting Room	Mars Maps
5:30 p.m.	Strong Hall Poster Area	Poster Session: 2018 Planetary Geologic Mappers Meeting

Wednesday, June 13, 2018

8:30 a.m.	Strong Hall Meeting Room	GIS and Planetary Mapping Techniques and Lunar Maps
1:15 p.m.	Strong Hall Meeting Room	Asteroid, Dwarf Planet, and Outer Planet Satellite Maps

Thursday, June 14, 2018

8:30 a.m.	Strong Hall	Optional Field Trip to Appalachian Mountains
-----------	-------------	--

Program

Tuesday, June 12, 2018
INTRODUCTION AND MERCURY AND VENUS MAPS
9:00 a.m. Strong Hall Meeting Room

Chairs: David Williams
Devon Burr

9:00 a.m. Williams D. A. *
Introduction and Welcome

9:05 a.m. Burr D. M. *
Logistics

9:15 a.m. Skinner J. A. *
Report from the U.S.G.S. Planetary Geologic Mapping Coordinator

9:45 a.m. Ostrach L. R. * Mest S. C. Prockter L. M. Petro N. E. Byrne P. K.
2018 Update on the Geologic Map of the Borealis Quadrangle (H-1) on Mercury [#7010]
We present the current mapping progress of the Borealis Quadrangle (H-1).

10:05 a.m. Whitten J. L. * Fassett C. I. Ostrach L. R.
Geologic Map of the Derain (H-10) Quadrangle on Mercury: The Challenges of Consistently Mapping the Intercrater Plains Unit [#7027]
We present the initial mapping of the H-10 quadrangle on Mercury, a region that was imaged for the first time by MESSENGER. Geologic map with assist with further characterization of the intercrater plains and their possible formation mechanism(s).

10:25 a.m. Buczkowski D. L. * McGowan E. M. McGill G. E.
Geology of the Lachesis Tessera Quadrangle (V-18), Venus [#7018]
We present a first draft of the geologic map of the Lachesis Tessera (V-18) quadrangle completed by George McGill.

10:45 a.m. Poster Preview
Each presenter will have one minute to summarize their poster and may present one slide.

11:00 a.m. *Lunch*

Tuesday, June 12, 2018
MARS MAPS
1:00 p.m. Strong Hall Meeting Room

Chair: David Williams

- 1:00 p.m. Weitz C. M. * Berman D. C. Rodriguez A. P. Bishop J. L.
Geologic Mapping and Studies of Diverse Deposits at Noctis Labyrinthus, Mars [#7006]
We are mapping the western portion of Noctis Labyrinthus (–6 to –14°N, –99.5 to –95.0°W) at 1:500,000 scale, which includes some of the most diverse mineralogies identified on Mars using CRISM data.
- 1:20 p.m. Mohr K. J. * Williams D. A. Garry W. B. Bleacher J. E.
Preliminary Volcanic Feature Analysis of Olympus Mons and Ascraeus Mons, Mars [#7007]
Geologic mapping has shown similar volcanic features observed on Olympus and Ascraeus Mons. These features are found on the same flanks, suggesting a similar evolutionary process for formation of the edifices.
- 1:40 p.m. Ackiss S. E. * Campbell A. Suda M. Horgan B. H.
Geomorphologic Mapping of a Possible Hesperian Subglacial Environment in the Sisyphi Montes, Mars [#7011]
Lets map and see if / The Sisyphi Montes, Mars / Could be subglacial.
- 2:00 p.m. Jacobsen R. E. * Burr D. M. Peel S. E. Borden R. M. Boyd A. S.
Understanding the History of a Diverse Inverted Landscape: Summary and Plan for Finishing the 1:500k Geologic Map of Aeolis Dorsa, Mars [#7014]
The Aeolis Dorsa region, Mars, consists of highlands and transitional units of the late Noachian, and aeolian/volcaniclastic deposits interleaved with fluvial and lacustrine deposits formed during the Hesperian and Amazonian periods.
- 2:20 p.m. Berman D. C. * Weitz C. M. Rodriguez J. A. P. Crown D. A.
Geologic Mapping of Mars Transverse Mercator Quadrangles 00042 and 00047 [#7019]
We are conducting geologic mapping of the source region of Shalbatana Vallis, Mars.
- 2:40 p.m. Thomson B. J. * Buczkowski D. L. Crumpler L. S. Seelos K. D.
Geologic Mapping at 1:60k Scale of Western Aeolis Mons, Gale Crater [#7020]
Water flows on ground / Can't move enough sediment / To build a tall mound.
- 3:00 p.m. *Break*
- 3:15 p.m. Skinner J. A. Jr. * Fortezzo C. M.
Final Stages of the 1:24,000-Scale Geologic Mapping of Basin Deposits Exposed in Hadriacus Cavi, Mars [#7022]
This abstract presents a brief summary of the surface and section characteristics of a type area for stratified deposits exposed in Hadriacus Cavi (78.0°E, –27.3°N), Mars based on 1:24,000 scale geologic mapping and stratigraphic analyses.
- 3:35 p.m. Seelos K. D. * Ackiss S. E. Seelos F. P. McBeck J. A. Buczkowski D. L. Hash C. D. Viviano C. E. Murchie S. L.
Mineralogy of Huygens Basin, Mars: A Transect of Noachian Highlands Crust [#7023]
Huygens crater represents a unique probe of the Noachian crust in the Hellas rim region. We have identified four mineralogic units within a morphologic context to understand the ancient martian highlands.

- 3:55 p.m. Garry W. B. * Williams D. A. Dapremont A. M. Shean D. E.
The 1:1,000,000 Geologic Map of Arsia Mons, Mars [#7028]
We have mapped the volcanic and glacial units on Arsia Mons volcano, Mars.
- 4:15 p.m. Mest S. C. * Crown D. A. Michalski J. Chuang F. C. Price Blount K. Bleamaster L. F.
Investigations of Volcanic and Volatile-Driven Processes Northeast of Hellas Basin, Mars [#7029]
We are mapping the geologic units and features in three MTM quadrangles northeast of Hellas basin at 1:1M scale. The area displays evidence for volcanism and widespread volatile-related modification of the surface.
- 4:35 p.m. Huff A. E. * Skinner J. A. Jr.
Completion of the 1:1,500,000-Scale Geologic Map of Western Libya Montes and Northwestern Tyrrhena Terra [#7033]
Final progress report on the 1:1,500,000-scale mapping of western Libya Montes and northwestern Tyrrhena Terra. The final unit names, labels, and descriptions are reported as well as the methodology for age determinations and brief geologic history.
- 4:55 p.m. Discussion

Tuesday, June 12, 2018
POSTER SESSION: 2018 PLANETARY GEOLOGIC MAPPERS MEETING
5:30 p.m. Strong Hall Poster Area

Okubo C. H.

High-Resolution Geologic Mapping in Eastern Candor Chasma: 2018 Status Report [#7002]

This abstract summarizes current results from ongoing large-scale structural and geologic mapping in the northern NIA Mensa region of Candor Chasma in Valles Marineris, Mars.

Crown D. A. Berman D. C. Scheidt S. P. Hauber E.

Geologic Mapping Investigations of Alba Mons, Mars [#7005]

Geologic mapping of the summit region and western flank of Alba Mons at 1:1M-scale is revealing sequences of volcanic, tectonic, impact, and degradation processes that have formed and modified the northernmost of the Tharsis volcanoes.

Keszthelyi L. P. Huff A. E.

Completing the Geologic Mapping of Athabasca Valles, Mars [#7012]

It's baaaack! With some help from more experienced mappers, this highly delinquent map is rapidly approaching submission. And Athabasca Valles and surroundings remain as fascinating as ever.

Wolak J. M. Patterson A. B. Smith S. D. Robbins N. N.

High-Resolution Geologic Mapping of Martian Terraced Fan Deposits [#7015]

This abstract documents our initial progress (year 1) mapping terraced fan features on Mars. Our objective is to investigate the role of fluids during fan formation and produce the first high-resolution geologic map (1:18k) of a terraced fan.

Emran A. King D. T. Jr. Marzen L. J. Coker C. W. Wright S. P.

Remote Sensing Characterization of Siloe Patera, Mars [#7017]

We interpret a variety of surficial geology from combining morphology and thermal inertia of Siloe Patera, Mars.

Peel S. E. Burr D. M.

Enigmatic Sedimentary Deposits Within Partially Exhumed Impact Craters in the Aeolis Dorsa Region, Mars: Evidence for Past Crater Lakes [#7030]

We mapped enigmatic sedimentary deposits within five partially exhumed impact craters within the Aeolis Dorsa Region of Mars. Ten units have been identified and are found to be consistent with deposition within and adjacent to lacustrine systems.

Trautman M. R. Malhotra S. Nainan C. Kim R. M. Bui B. X. Sadaqathullah S. Sharma P. Gallegos N. Law E. S. Day B. H.

NASA's Solar System Treks Image Mosaic Pipeline [#7032]

This study details the efforts of the NASA Solar System Treks project to design a framework for automated systems capable of producing quality mosaics from high resolution orbital imagery. The primary focus is on NAC, CTX, and HiRISE imagery.

Kinczyk M. J. Byrne P. K. Prockter L. M. Denevi B. W. Ostrach L. R. Skinner J. A.

Preparing the First Global Geological Map of Mercury [#7031]

We present the progress made on producing the global geological map of Mercury and in differentiating geological units within the intercrater plains.

Lang N. P. Covley M. T. Beltran J. Rogers K. Thomson B. J.

Geologic Mapping of Impact Craters and the Mahuea Tholus Construct: A Year Three Progress Report for the Mahuea Tholus (V-49) Quadrangle, Venus [#7024]

We are reporting on our year three status of mapping the V-49 quadrangle (Mahuea Tholus). Our mapping efforts over this past year emphasized the 13 impact craters in the quadrangle as well as larger-scale mapping of the Mahuea Tholus construct.

Maue A. D. Burr D. M. Levy J. S. Nathan E.

Updating the Global Map of Titan Fluvial Features and Investigating Downstream Radar Brightness Trends [#7021]

Fluvial features are being mapped for all radar swaths at the end of the Cassini mission. Downstream changes in radar brightness within some fluvial features are being measured as a potential indication of grain size trends.

Cartwright S. F. A. Spudis P. D.

Geology of the Lunar Moscoviense Basin [#7009]

Presents a new geologic map of the Moscoviense Basin and its ejecta deposits, and discusses results from structural mapping and compositional analyses of mapped units.

Robbins S. J. Spencer J. R. Beyer R. A. Schenk P. M. Moore J. M. McKinnon W. B. Binzel R. P.

Buie M. W. Buratti B. J. Cheng A. F. Grundy W. M. Linscott I. R. Reitsema H. J. Reuter D. C.

Showalter M. R. Tyler G. L. Young L. A. Olkin C. B. Ennico K. Weaver H. A. Stern S. A.

Geologic Map of New Horizons' Encounter Hemisphere of Charon, V [#7036]

A pretty much completed geologic map of Charon will be shown.

Wednesday, June 13, 2018
GIS AND PLANETARY MAPPING TECHNIQUES AND LUNAR MAPS
8:30 a.m. Strong Hall Meeting Room

Chair: David Williams

- 8:30 a.m. Jacobsen R. E. Fay C. *
Developing an Application to Increase the Accessibility of Planetary Geologic Maps [#7016]
USGS planetary geologic maps are widely used digital products with text, raster, vector, and temporal data, within a highly standardized design. This tool will augment the user experience by improving accessibility among the various forms of data.
- 8:50 a.m. Golder K. B. * Burr D. M.
Geomorphic Mapping of Lava Flows on Mars, Earth, and Mercury [#7025]
To advance understanding of flood basalts, we have mapped lava flows on three planets, Mars, Earth, and Mercury, as part of three projects. The common purpose of each project is to investigate potential magma sources and/or emplacement conditions.
- 9:10 a.m. Robbins S. J. *
The Fractal Nature of Planetary Landforms and Implications to Geologic Mapping [#7035]
The importance of / Fractals in planetary / Mapping is complex.
- 9:30 a.m. Hunter M. *
Review and Discussion of GIS for Planetary Mapping
- 10:15 a.m. *Break*
- 10:30 a.m. Fortezzo C. M. * Spudis P. D.
Digital Global Geologic Map of the Moon: Analysis Tool for Lunar Research [#7034]
Details the progress made during year two of the project and details for the remaining tasks before the product release.
- 10:50 a.m. Garry W. B. * Mest S. C. Yingst R. A. Ostrach L. R. Petro N. E. Cohen B. A.
Updating the Geologic Maps of the Apollo 15, 16, and 17 Landing Sites [#7013]
Our team is funded through NASA's Planetary Data Archiving, Restoration, and Tools (PDART) program to produce two new USGS Special Investigation Maps (SIM) for the Apollo 15, 16, and 17 missions: a regional map (1:200K) and a landing-site map (1:24K).
- 11:10 a.m. Discussion
- 11:30 a.m. *Lunch*

Wednesday, June 13, 2018
ASTEROID, DWARF PLANET, AND OUTER PLANET SATELLITE MAPS
1:15 p.m. Strong Hall Meeting Room

Chair: David Williams

- 1:15 p.m. Yingst R. A. * Mest S. C. Williams D. A. Garry W. B. Berman D. C.
Geologic Mapping of Vesta: Early Results [#7004]
We are constructing a global geologic map of Vesta at 1:300,000-scale for mapping and digital publication, and 1:1,500,000-scale for the print version.
- 1:35 p.m. Williams D. A. * Buczkowski D. L. Crown D. A. Frigeri A. Hughson K. Kneissl T. Krohn K. Mest S. C. Pasckert J. H. Platz T. Ruesch O. Schulzeck F. Scully J. E. C. Sizemore H. G. Nass A. Jaumann R. Raymond C. A. Russell C. T.
High-Resolution Global Geologic Map of Ceres from NASA Dawn Mission [#7001]
This presentation will discuss the completed 1:4,000,000 global geologic map of dwarf planet Ceres derived from Dawn Framing Camera Low Altitude Mapping Orbit (LAMO) images, combining 15 quadrangle maps.
- 1:55 p.m. Leonard E. J. * Patthoff D. A. Senske D. A. Collins G. C.
The Europa Global Geologic Map [#7008]
The Europa Global Geologic Map reveals three periods in Europa's surface history as well as an interesting distribution of microchaos. We will discuss the mapping and the interesting implications of our analysis of Europa's surface.
- 2:15 p.m. Martin E. S. * Patthoff D. A. Bland M. T. Watters T. R. Collins G. C. Becker T.
Building a Geologic Map of Neptune's Moon Triton [#7026]
Triton serves as a bridge between KBOs and icy satellites, and characterization of its terrains is important for advancing comparative planetological studies. We aim to create a geologic map of the Neptune-facing side of Triton at a scale of 1:5M.
- 2:35 p.m. Poster Viewing
- 3:35 p.m. Discussion and Findings for MAPSIT
- 4:50 p.m. Other Business
- 5:05 p.m. Adjourn

CONTENTS

Geomorphologic Mapping of a Possible Hesperian Subglacial Environment in the Sisyphi Montes, Mars <i>S. E. Ackiss, A. Campbell, M. Suda, and B. H. Horgan</i>	7011
Geologic Mapping of Mars Transverse Mercator Quadrangles 00042 and 00047 <i>D. C. Berman, C. M. Weitz, J. A. P. Rodriguez, and D. A. Crown</i>	7019
Geology of the Lachesis Tessera Quadrangle (V-18), Venus <i>D. L. Buczkowski, E. M. McGowan, and G. E. McGill</i>	7018
Geology of the Lunar Moscoviense Basin <i>S. F. A. Cartwright and P. D. Spudis</i>	7009
Geologic Mapping Investigations of Alba Mons, Mars <i>D. A. Crown, D. C. Berman, S. P. Scheidt, and E. Hauber</i>	7005
Remote Sensing Characterization of Siloe Patera, Mars <i>A. Emran, D. T. King, L. J. Marzen, C. W. Coker, and S. P. Wright</i>	7017
Digital Global Geologic Map of the Moon: Analysis Tool for Lunar Research <i>C. M. Fortezzo and P. D. Spudis</i>	7034
Updating the Geologic Maps of the Apollo 15, 16, and 17 Landing Sites <i>W. B. Garry, S. C. Mest, R. A. Yingst, L. R. Ostrach, N. E. Petro, and B. A. Cohen</i>	7013
The 1:1,000,000 Geologic Map of Arsia Mons, Mars <i>W. B. Garry, D. A. Williams, A. M. Dapremont, and D. E. Shean</i>	7028
Geomorphologic Mapping of Lava Flows on Mars, Earth, and Mercury <i>K. B. Golder and D. M. Burr</i>	7025
Completion of the 1:1,500,000-Scale Geologic Map of Western Libya Montes and Northwestern Tyrrhena Terra <i>A. E. Huff and J. A. Skinner</i>	7033
Developing an Application to Increase the Accessibility of Planetary Geologic Maps <i>R. E. Jacobsen and C. Fay</i>	7016
Understanding the History of a Diverse Inverted Landscape: Summary and Plan for Finishing the 1:500k Geologic Map of Aeolis Dorsa, Mars <i>R. E. Jacobsen, D. M. Burr, S. E. Peel, R. M. Borden, and A. S. Boyd</i>	7014
Completing the Geologic Mapping of Athabasca Valles, Mars <i>L. P. Keszthelyi and A. E. Huff</i>	7012
Preparing the First Global Geological Map of Mercury <i>M. J. Kinczyk, P. K. Byrne, L. M. Prockter, B. W. Denevi, L. R. Ostrach, and J. A. Skinner</i>	7031
Lunar Tectonic Triad Joining Both Hemispheres and Its Terrestrial Analogue <i>G. G. Kochemasov</i>	7003

Geologic Mapping of Impact Craters and the Mahua Tholus Construct: A Year Three Progress Report for the Mahua Tholus (V-49) Quadrangle, Venus <i>N. P. Lang, M. T. Covley, J. Beltran, K. Rogers, and B. J. Thomson</i>	7024
The Europa Global Geologic Map <i>E. J. Leonard, D. A. Patthoff, D. A. Senske, and G. C. Collins</i>	7008
Building a Geologic Map of Neptune’s Moon Triton <i>E. S. Martin, D. A. Patthoff, M. T. Bland, T. R. Watters, G. C. Collins, and T. Becker</i>	7026
Updating the Global Map of Titan Fluvial Features and Investigating Downstream Radar Brightness Trends <i>A. D. Maue, D. M. Burr, J. S. Levy, and E. Nathan</i>	7021
Investigations of Volcanic and Volatile-Driven Processes Northeast of Hellas Basin, Mars <i>S. C. Mest, D. A. Crown, J. Michalski, F. C. Chuang, K. Price Blount, and L. F. Bleamaster</i>	7029
Preliminary Volcanic Feature Analysis of Olympus Mons and Ascræus Mons, Mars <i>K. J. Mohr, D. A. Williams, W. B. Garry, and J. E. Bleacher</i>	7007
High-Resolution Geologic Mapping in Eastern Candor Chasma: 2018 Status Report <i>C. H. Okubo</i>	7002
2018 Update on the Geologic Map of the Borealis Quadrangle (H-1) on Mercury <i>L. R. Ostrach, S. C. Mest, L. M. Prockter, N. E. Petro, and P. K. Byrne</i>	7010
Enigmatic Sedimentary Deposits Within Partially Exhumed Impact Craters in the Aeolis Dorsa Region, Mars: Evidence for Past Crater Lakes <i>S. E. Peel and D. M. Burr</i>	7030
The Fractal Nature of Planetary Landforms and Implications to Geologic Mapping <i>S. J. Robbins</i>	7035
Geologic Map of New Horizons’ Encounter Hemisphere of Charon, V <i>S. J. Robbins, J. R. Spencer, R. A. Beyer, P. M. Schenk, J. M. Moore, W. B. McKinnon, R. P. Binzel, M. W. Buie, B. J. Buratti, A. F. Cheng, W. M. Grundy, I. R. Linscott, H. J. Reitsema, D. C. Reuter, M. R. Showalter, G. L. Tyler, L. A. Young, C. B. Olkin, K. Ennico, H. A. Weaver, and S. A. Stern</i>	7036
Mineralogy of Huygens Basin, Mars: A Transect of Noachian Highlands Crust <i>K. D. Seelos, S. E. Ackiss, F. P. Seelos, J. A. McBeck, D. L. Buczkowski, C. D. Hash, C. E. Viviano, and S. L. Murchie</i>	7023
Final Stages of the 1:24,000-Scale Geologic Mapping of Basin Deposits Exposed in Hadriacus Cavi, Mars <i>J. A. Skinner and C. M. Fortezzo</i>	7022
Geologic Mapping at 1:60k Scale of Western Aeolis Mons, Gale Crater <i>B. J. Thomson, D. L. Buczkowski, L. S. Crumpler, and K. D. Seelos</i>	7020
NASA’s Solar System Treks Image Mosaic Pipeline <i>M. R. Trautman, S. Malhotra, C. Nainan, R. M. Kim, B. X. Bui, S. Sadaqathullah, P. Sharma, N. Gallegos, E. S. Law, and B. H. Day</i>	7032

Geologic Mapping and Studies of Diverse Deposits at Noctis Labyrinthus, Mars <i>C. M. Weitz, D. C. Berman, A. P. Rodriguez, and J. L. Bishop</i>	7006
Geologic Map of the Derain (H-10) Quadrangle on Mercury: The Challenges of Consistently Mapping the Intercrater Plains Unit <i>J. L. Whitten, C. I. Fassett, and L. R. Ostrach</i>	7027
High-Resolution Global Geologic Map of Ceres from NASA Dawn Mission <i>D. A. Williams, D. L. Buczkowski, D. A. Crown, A. Frigeri, K. Hughson, T. Kneissl, K. Krohn, S. C. Mest, J. H. Pasckert, T. Platz, O. Ruesch, F. Schulzeck, J. E. C. Scully, H. G. Sizemore, A. Nass, R. Jaumann, C. A. Raymond, and C. T. Russell</i>	7001
High-Resolution Geologic Mapping of Martian Terraced Fan Deposits <i>J. M. Wolak, A. B. Patterson, S. D. Smith, and N. N. Robbins</i>	7015
Geologic Mapping of Vesta: Early Results <i>R. A. Yingst, S. C. Mest, D. A. Williams, W. B. Garry, and D. C. Berman</i>	7004

GEOMORPHOLOGIC MAPPING OF A POSSIBLE HESPERIAN SUBGLACIAL ENVIRONMENT IN THE SISYPHI MONTES, MARS. S. E. Ackiss, A. Campbell, M. Suda, B. Horgan, Purdue University, Department of Earth, Atmospheric, and Planetary Sciences, West Lafayette, IN 47907 (sackiss@purdue.edu)

Introduction: The Sisyphi Montes region (55-75°S, 335-40°E) is located in the southern highlands between the Argyre and Hellas basins (Figure 1). It is composed of isolated domical features [1, 2] and a unit interpreted to be portions of the ancient Dorsa Argentea ice sheet [3, 4]. While the domes are thought to be volcanic in nature, it is still unclear whether they were formed subglacially or subaerially. [1] proposed that the morphologies seen are consistent with volcanoes that were built and erupted under a more extensive Hesperian-aged ice sheet. [5] conducted a mineralogic study of the edifices using Mars Reconnaissance Orbiter (MRO) Compact Reconnaissance Imaging Spectrometer for Mars (CRISM) to see if the mineralogy of the edifices is also consistent with a subglacial origin. The assemblage found consists of sulfates (polyhydrated and gypsum) and a smectite-zeolite-iron oxide mixture most consistent with palagonite. While this is consistent with a subglacial formation environment, it does not definitively distinguish if the volcanic edifices were subglacial or subaerial in origin. The creation and analysis of this proposed geomorphologic map strives to answer the overarching question: What is the origin/environment of formation of the Sisyphi Montes?

Data Sets and Methods: This region has been previously mapped at the 1:2,000,000 scale [6] using data from Viking and was recently mapped in broad geologic units at a scale of 1:20,000,000 [7] using higher resolution datasets including the MGS Mars Orbiter Laster Altimeter (MOLA) [8], Thermal Emission Imaging System (THEMIS) [9] mid-infrared daytime images, and the MRO Context Camera (CTX) [10].

While the previous maps of this region [7-8] have contributed to the interpretation of the region, there are still some major knowledge gaps that could be answered using a finer-scale, higher-resolution map. We propose to construct a geomorphologic map of this region at scales between 1:600,000 and 1:250,000. Basemap data includes MOLA topographic data (128 pix/deg or ~460 m/pix), THEMIS daytime infrared (18 m/pix), and CTX (6 m/pix) for morphologic data. This map will be supplemented with CRISM hyperspectral targeted images and multispectral mapping strips used to show large outcrops of hydrated and mafic minerals (e.g. sulfates, clays, zeolites, olivine, and pyroxene). Standard geomorphologic contact mapping methods will be utilized. Additionally, mineralogic outcrops observed in CRISM will be mapped where clear spectral signatures are present. Crater counts at the edifice scale (50-100km) will also be conducted and used to verify the age of the

Sisyphi Montes in comparison to the surrounding Sisyphi Planum. Using this scale and the added spectral datasets will combine geomorphologic and spectral data to construct a more complete picture of the Sisyphi Montes region.

Discussion: By correlating the morphology with the mineralogy of this region, we can place constraints on the formation of the edifices. Because of the previous research in this area [1, 2, 4, 5], our preferred hypothesis is that these edifices are subglacial in origin. In volcanic eruptions beneath ice sheets and glaciers on Earth, the combination of heat and large quantities of melt water lead to the production of unique morphologies. These morphologies include “tuyas” or table mountains that are steep sided and flat topped edifices and “tindars” or ridges that are flat-topped and linear. Subglacial mounds, which are conical in shape, are made when the eruption does not breach the ice-sheet [11]. The dominant spectral signatures for this environment are expected to be glass, zeolites, and smectites [5, 12-13]. A possible smectite-zeolite-iron oxide mixture has been recently identified on the edifices using CRISM spectra [5], consistent with a volcanic origin.

We are also considering three other hypotheses for the origin of the high latitude edifices:

(1) Subaerial volcanism: Subaerial volcanism includes stratovolcanoes, complex volcanoes, compound volcanoes, somma volcanoes, shield volcanoes, pyroclastic shields, lava cones, and lava domes [14]. The morphologies of these edifices are typically cone-shaped and on average 5° less steep than glaciovolcanic edifices [15]. The dominant spectral signatures for this environment are expected to be crystalline mafic minerals and a variety of clay minerals [5, 16].

(2) Impact cratering: Because some of the Sisyphi Montes are encircled by local moat-like features with raised rims, [17] hypothesized that the edifices were formed due to a combination of volcanic and impact-related processes. They proposed that the magma that created the structures was sourced from magma bodies intersecting large impact-induced zones of crustal weakness circumferential to the Hellas basin. The magma was then brought to the surface by subsequent small impacts, building edifices in the centers of the smaller impact craters [17]. We can test the hypothesis of volcanism inside impact craters by seeing if all of the edifices are associated with moat-like features. We hypothesize that the expected mineralogy of this environment would be variable because impact craters bring up old crust that is buried in the subsurface [18].

(3) Erosional remnants: Erosional features can form in different landscapes including deserts (e.g. mesas, plateaus, canyons, inselbergs, yardings), glaciated regions (e.g. drumlins and depositional features including moraines and eskers), and karsts (e.g. caves and sink-holes) [19]. The key to mapping erosional remnants is differentiating them from “unaltered” or primary landforms. For example, inselbergs (an isolated hill rising from a plain) and kipukas (an isolated hill surrounded by lava) can look similar from orbit but have very different formation environments. Similarly, mesas (isolated flat-topped, steep-sided hills made of horizontal strata) can resemble tuyas (flat-topped, steep-sided volcanic edifices). We hypothesize that the expected mineralogy of erosional remnants would include clay minerals and carbonates in depressions and stratified layers.

Implications: This research will provide the first comprehensive map comprised of compositional and morphological information of the Sisyphi Montes region at this scale, which we will use to answer the question: What is the origin/environment of formation of the Sisyphi Montes? Because the Sisyphi Montes may record the presence of ice outside of the south polar region, measurements including edifice height and location can provide insights into the extent of the sub-polar paleoicesheet. This will provide regional information about the history of the Dorsa Argentea Formation, as well as surrounding volcanic features such as Pityusa

and Malea Paterae. In particular, it will provide new information pertaining to the martian paleoclimate, possibly helping to address the validity of the current “warm and wet” [20] and “cold and icy” [21, 22] climate models. The results from this study will provide novel insight into regional volcanic and glacial processes.

Acknowledgements: S. Ackiss thanks the Purdue Doctoral Fellowship for support and the staff at USGS Flagstaff for help creating an ArcGIS geodatabase.

References: [1] Ghatan and Head (2002), *J. Geophys. Res. Planets*, vol. 107, p. 5048. [2] Farrand et al., (2008), 39th LPSC, Abstract # 1761. [3] Ghatan and Head (2004), *J. Geophys. Res. Planets*, vol. 109, no. E7, p. E07006. [4] Scanlon and Head (2015), 46th LPSC, Abstract # 2247. [5] Ackiss et al., (2018) in press, *Icarus*. [6] Tanaka, K. L., and Scott (1987), U.S. Geol. Surv., Misc. Investigations (Series Map I-802-C, Scale 1:15,000,000) [7] Tanaka et al., (2014), *Geologic map of Mars: U.S.G.S. Scientific Investigations Map 3292, scale 1:20,000,000*. [8] Smith et al. (2001), *J. Geophys. Res. Planets*, 106(E10), 23689–23722. [9] Christensen et al. (2004), *Space Sci. Rev.*, 110, 85–130. [10] Malin et al. (2007), *J. Geophys. Res. Planets*, 112 [11] Russell et al., (2014), *Quat. Sci. Rev.*, 87, 70–81 [12] Swayze et al., (2002), *Proc. 11th JPL Airborne Earth Space Workshop*, (JPL Publication 03-4). [13] Paque et al., (2016), *Bulletin of Volcanology*, 78, 61. [14] Grosse et al., (2014), *Bulletin of Volcanology*, 76.1, 784. [15] Pedersen and Grosse (2014), *Journal of Volcanology and Geothermal Research* 282, 115-133 [16] Ehlmann et al., (2012), *J. Geophys. Res. Planets*, 117, E00J16, [17] Rodriguez and Tanaka (2006), *LPI Contrib.*, 1323, 8066. [18] Ehlmann et al., (2011), *Nature*, 479(7371), 53–60, [19] Monroe, (1970), U.S.G.S., Water-Supply Paper 1899, 26 p. [20] Craddock and Howard (2002), *J. Geophys. Res. Planets*, 107(E11). [21] Wordsworth et al., (2013), *Icarus*, 222(1), 1–19 [22] Wordsworth et al., (2015), *J. Geophys. Res. Planets*, 120(6), 2015JE004787.

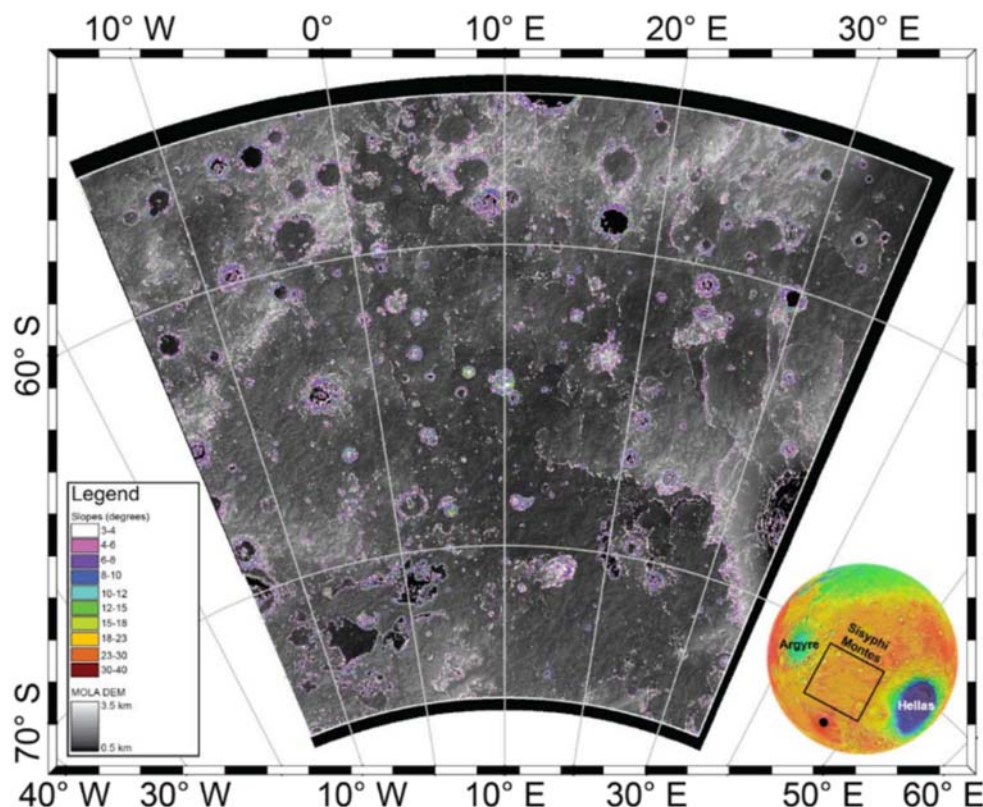


Figure 1. MOLA DEM of the Sisyphi Montes region (white is high and black is low). Slopes are denoted by colored regions, helping to show the multiple edifices and craters in the region. Inset shows global context of the region.

GEOLOGIC MAPPING OF MARS TRANSVERSE MERCATOR QUADRANGLES 00042 AND 00047.

Daniel C. Berman, Catherine M. Weitz, J. Alexis Palmero Rodriguez, and David A. Crown, Planetary Science Institute, 1700 E. Ft. Lowell Rd., Suite 106, Tucson, AZ 85719; bermandc@psi.edu.

Introduction: We are currently producing a 1:500,000-scale USGS geologic map of MTM quadrangles 00042 and 00047 in the Xanthe Terra region of Mars (2.5°S - 2.5°N, 310° - 320°E) (Fig. 1). The map region has been extensively modified by outflow channels and chaotic terrains and contains cratered plains deformed by subsidence [e.g., 1]. The overarching goal of this project is to document the sequence and types of hydrologic processes that developed as a consequence of the melting of subsurface ice, leading to subsidence and collapse. In particular, we examine the history of catastrophic floods in the region linked to these processes.

Geologic mapping is being conducted on a THEMIS IR daytime base mosaic, with CTX and HiRISE images as supplements where available. Geologic contacts, linear features, and surface features have been mapped, and geologic units have been defined (Fig. 1).

Geologic Units and Features: Types of geologic units include plains, crater, vallis, chaos, and surficial units. The boundaries of cratered plains units 1 (*cp1*) and crater plains 2 (*cp2*) are similar to those of *Npl₁* and *Npl₂* as in [2]. The plains units are smooth to mottled in appearance and are disrupted by secondary crater chains, wrinkle ridges, and areas of minor collapse. The ejecta blankets of the numerous large craters are partly eroded and in some cases entirely removed. Cratered plains 2 is similar to cratered plains 1, but with a dark signature in THEMIS day IR (bright in night IR) and some knobs. Crater counts give an age of ~3.8 Ga (Late Noachian) for both plains units, with a possible resurfacing event at ~3.6 Ga.

Crater units include crater material (*c*) and crater fill material (*cf*). Crater material includes ejecta blankets, rims, and floor materials for relatively unmodified bowl-shaped craters. The ejecta blanket of Orson Welles crater has been mantled and subdued by aeolian materials. Crater fill material consists of smooth or fractured infill deposits on flat crater floors.

Many of both the crater and vallis units are characterized by collapse and retreat. Shalbatana and Ravi Valles are characterized by smooth and chaotic floor units. Vallis units are divided into vallis floor material – upper smooth (*vfus*), vallis floor material – lower smooth (*vfls*), vallis floor material – etched (*vfe*) (which comprises the lower floor of Ravi Vallis), and vallis wall material (*vw*), comprised mainly of talus.

Chaos units include chaos material 1 (*ch1*) and chaos material 2 (*ch2*). Chaos material 1 occurs at higher elevations and contains larger, often flat-topped blocks,

whereas chaos material 2 is at lower elevations and mostly comprised of knobby blocks.

Surficial units include dune material (*d*), found on the western floor of Orson Welles crater, landslide material (*l*), found along the retreating walls of Orson Welles crater and Shalbatana Vallis, lava flow material (*lf*), which extends to the southeast from Aromatum Chaos, and light-toned deposits (*lt*) found in several locations on the floors of subsided terrain (smooth floor material and chaos material 2) and craters.

Mapped linear features include crater rims, volcanic and fluvial channels, grooves, grabens, ridges, troughs, pit-crater chains, faults, and scarp crests. We have also mapped surface features including dark ejecta and secondary crater chains. All craters greater than 5 km in diameter have been mapped.

Geomorphic mapping of chaotic and subsided terrains is proceeding, along with related extensional faults south of Orson Welles crater, showing a zone of subsurface evacuation reaching to Ganges Chasma.

Geologic History: The impact that formed Orson Welles crater may have penetrated an aquifer or subsurface ice lens leading to initial outflow and incision of Shalbatana Vallis. Following impact, the plains units were resurfaced with weakly consolidated (potentially ice-rich) materials; Orson Welles and other large craters were infilled and their ejecta and rims were partially to completely removed. Melting of subsurface ice (perhaps by magmatic intrusion) led to the collapse of the infill material, resulting in chaos material 1 [e.g., 3]. The remaining infill material was swept away during resulting catastrophic flooding and outflow, incising Shalbatana Vallis and leaving behind chaos material 2 and smooth floor materials. Subsequent collapse and retreat of the crater walls led to talus deposits on the walls and landslides. Some of the blocks on the floor of chaos material 2 may also be from wall collapse. Dune material was the last to form.

Aromatum Chaos forms the source area of both a lava flow and an outflow channel. The lava flow likely erupted from a fissure parallel to the southern margin of the chaotic terrain that was subsequently destroyed during ongoing collapse and retreat of the canyon wall. Craters that impacted into the lava flow exhibit high thermal inertia ejecta blankets with large boulder deposits. Close examination of the southern wall of Aromatum Chaos in HiRISE images reveals evidence of a sequence of possible buried lava flows that form low-albedo bouldery outcrops. Episodic volcanic activity in the region could have provided high geothermal

conditions conducive to groundwater outburst leading to catastrophic flooding [4].

Flooding in Ravi Vallis inundated plains surfaces above the margins of its grooved floor, where the floods deposited widespread smooth deposits, locally marked by small-scale streamlined landforms. These smooth floors flank the lower scoured sections and their origin might be related to earlier floods that were not topographically constrained within a channel and thus spread (and thinned out) over the intercrater plains, thereby rapidly losing velocity. This scenario indicates a possible transition from non-catastrophic floods (depositional) to catastrophic (erosional) floods.

Crater counts indicate that Ravi Valles and the lava flow both formed in the Early Hesperian, ~3.44 Ga for the channel and ~3.47 Ga for the lava flow, which would be consistent with the magmatic activity acting as a trigger for melting and outflow. The ejecta blanket of Dia Cau crater is bisected by Ravi Vallis, and we date its formation at ~3.61 Ga.

Light-toned deposits: CRISM analyses of the light-toned deposits show evidence for Fe/Mg-smectites and

hydrated silica. Light-toned Fe/Mg-smectite deposits are also observed along the upper wall of one of the craters, indicating the deposits predate the impact. These results are consistent with melting of subsurface ice lenses, with water interacting with and altering subsurface layers to form smectites, which are later exposed due to either impact crater formation or subsidence and collapse.

Conclusions: Geologic mapping, combined with geomorphic and spectral analyses, show that subsurface ice in this region melted, leading to evacuation, collapse, and flooding, leaving behind cavities that have caused further deformation and collapse of surface units.

References: [1] K.L. Tanaka et al. (2014) USGS SIM-3292. [2] S. Rotto and K.L. Tanaka (1995) USGS SIM I-2441. [3] J.A.P. Rodriguez et al. (2015) Nature Scientific Reports, 5, 13404. [4] D.C. Berman et al. (2016) LPSC 47, #2674.

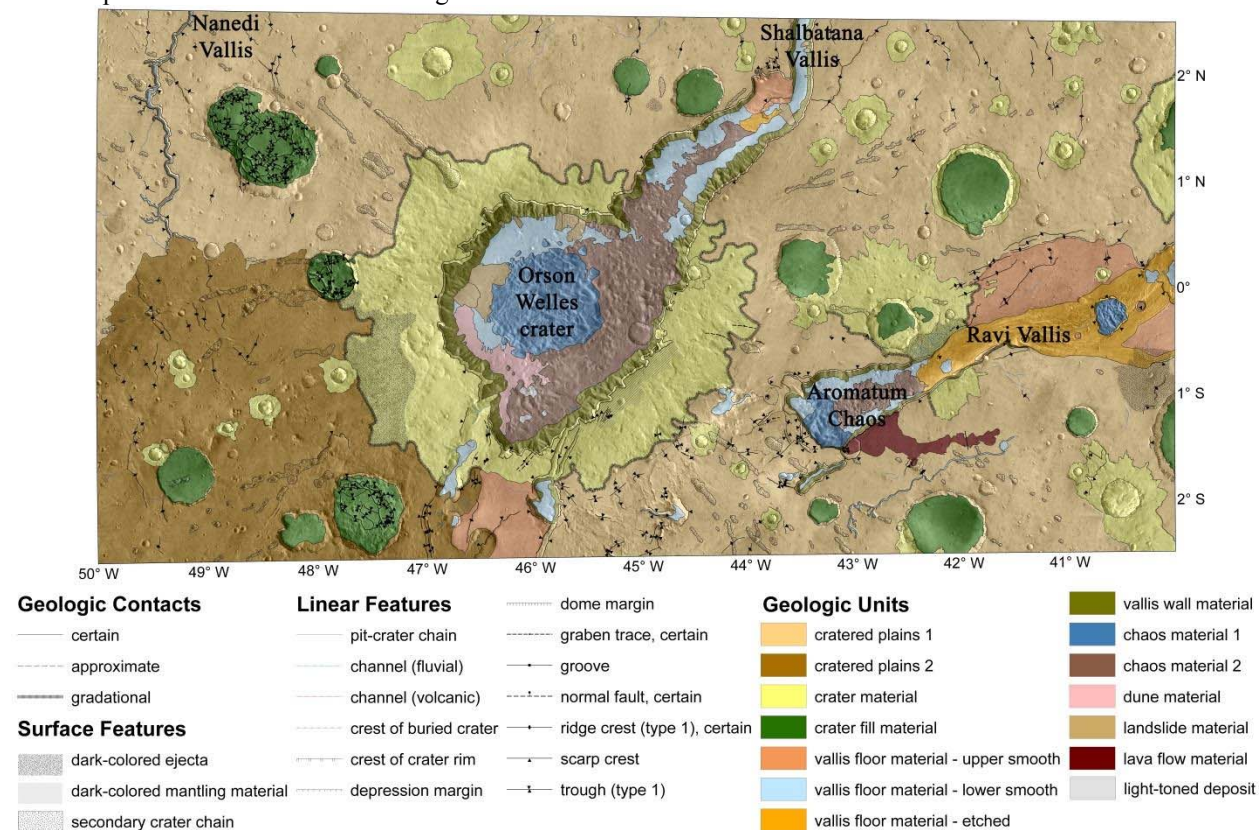


Figure 1. Geologic map of MTM Quadrangles 00042 and 00047 at 1:500,000 scale. THEMIS IR daytime base. Transverse Mercator projection. Map width is ~615 km.

GEOLOGY OF THE LACHESIS TESSERA QUADRANGLE (V-18), VENUS. D. L. Buczkowski¹, E. M. McGowan², and George E. McGill¹ Johns Hopkins Applied Physics Laboratory, Laurel, MD 20723, debra.buczkowski@jhuapl.edu, ²Springfield College, Springfield, MA, ³University of Massachusetts, Amherst, MA.

Introduction: The Lachesis Tessera quadrangle (V-18) lies between 25° and 50°N, 300° and 330°E. We present a first draft of a geologic map of the quadrangle completed by George McGill.

Methods: Mapping was based on a 250 m/pxl Magellan cycle 1 synthetic aperture radar (SAR) mosaic prepared by the U.S. Geological Survey (USGS) planetary team. Most of the mapping was carried out using 75m/pxl FMAPS provided by the USGS in digital format. During the mission, data for the Lachesis Tessera quadrangle were collected in left-looking mode at incidence angles ranging between 43.73° and 32.85°. The final base map is a 1:5,000,000-scale controlled mosaic of SAR data. Topographic information was derived from digital elevation models and from gridded elevation data; the altimetry data were combined with the SAR data by the USGS to create synthetic stereoscopic images.

Geology: The Lachesis Tessera quadrangle includes parts of Sedna and Guinevere Planitiae; regional plains [1] cover approximately 80% of the quadrangle. In addition, the quadrangle includes two deformation belts and embayed fragments of one or two possible additional belts, 3 large central volcanoes, abundant small shield volcanoes and associated flow materials, 13 impact craters, 3 named coronae, and a number of corona-like features [2]. A linear grouping of a prominent structural belt, coronae, and coronae-like structures are located oriented northwest to southeast in the southern half of the quadrangle [2].

Plains: By far the areally most extensive materials are regional plains. These are mapped as two units, based on radar backscatter (“radar brightness”). The brighter unit appears to be younger than the darker unit. This inference is based on the common presence within the lighter unit of circular or nearly circular inliers of material with radar backscatter characteristic of the darker unit. The circular inliers are most likely low shield volcanoes, which are commonly present on the darker unit, that were only partially covered by the brighter unit. Clear cut examples of wrinkle ridges and fractures superposed on the darker unit but truncated by the brighter unit have not been found to date. These relationships indicate that the brighter unit is superposed on the darker unit, but that the difference in age between them is very small. Because they are so widespread, the regional plains are a convenient relative age time “marker”. The number of impact craters superposed on these plains is too small to measure age differences [3], and thus we cannot estimate how much

time elapsed between the emplacement of the darker and brighter regional plains units. More local plains units are defined by significantly lower radar backscatter or by a texture that is mottled at scores to hundreds of kilometers scale. A plains-like unit with a homogeneous, bright diffuse backscatter is present as scattered exposures in the eastern part of the quadrangle. These exposures have been mapped as “bright material”, but it is not clear at present if this is a valid unit or if it is part of the brighter regional plains unit.

Tessera: Tessera terrain is primarily found along the western border of the quadrangle, where Lachesis Tessera refers to the southern exposures, and Zirka Tessera refers to northern exposures. A second tessera unit has been mapped with the symbol “t?”. This unit appears to be deformed by the requisite 2 sets of closely spaced structures, but it is so extensively flooded by regional plains materials that the structural fabric is partially obscured.

Deformation belts: Ridge and fracture belts are both present, but not as extensive as is the case in, for example, the Pandroses Dorsa [4] and Lavinia Planitia [5] quadrangles. As is commonly the case, it is difficult to determine if the materials of these belts are older or younger than regional plains. A recent study using radar properties [6] demonstrated that at least most ridge belts appear to be older than regional plains. The materials of fracture belts probably are also older than regional plains, but the fractures themselves can be both older and younger than regional plains [e.g., 4].

Coronae: Three named coronae are present, but only Zemira Corona has significant associated flows. An interesting nearly linear structure extends from the fracture belt Breksta Linea in the western part of the quadrangle east-southeastward through Zemira Corona to Pasu-Ava Corona. The tectonic significance of this composite structure is unclear at present. A feature named Jaszai Patera is very likely another corona.

Volcanoes and shield flows: Volcanic materials and landforms are abundant in the Lachesis Tessera quadrangle. In particular, small domes and shields are abundant and widespread. In places, small shields are not only exceptionally abundant, but they are associated with mappable materials, and thus help define a “shield flows” unit. Isolated flows are common, and where these are areally large enough they have been mapped as undifferentiated flows. Other volcanic features include two relatively large shield volcanoes, both with complete calderas and with flows extensive enough to map. A number of pancake domes occur in the Lachesis Tessera quadrangle. Various mechanisms

for forming flat-topped domes such as these have been proposed, but none is really satisfactory. This quadrangle is not likely to provide breakthrough evidence for the genetic processes responsible for pancake domes.

Impact craters: The 13 impact craters in the Lachesis Tessera quadrangle range in diameter from 2.4 to 40 km. Four of these are actually doublets. Five of the craters have associated radar-dark halos or parabolas. Only 2 of the 13 craters are significantly degraded. All 13 craters are superposed on either regional plains or on flows that are, in turn, superposed on regional plains.

Discussion: The fragmented record of tessera and some deformation belts suggests that flooding by re-

gional plains materials has had a significant effect on the distribution of materials older than the regional plains. This, in turn, indicates that regional plains must be relatively thin in the Lachesis Tessera quadrangle, or else the tessera and deformation belts exhibit less relief than generally is the case.

References: [1] McGill, G.E. (2000) V-20 quadrangle [2] McGowan E. M. & McGill, G. E. (2011) *LPSC XLII*, abs.1300 [3] Campbell, B.A. (1999) *JGR 104*, 21,951 [4] Rosenberg, E. & McGill, G.E. (2001) V-5 quadrangle [5] Ivanov, M.A. & Head, J.W., III (2001) V-55 quadrangle [6] McGill, G.E. & Campbell, B.A. (2006) *JGR 111*, E12006, doi:10.1029/2006JE002705.

GEOLOGY OF THE LUNAR MOSCOVIENSE BASIN. S. F. A. Cartwright¹ and P. D. Spudis², ¹Middlebury College Department of Geology, Middlebury, Vermont 05753 (sfcartwright@middlebury.edu), ²Lunar and Planetary Institute, 3600 Bay Area Blvd., Houston, TX 77058 (spudis@lpi.usra.edu)

Introduction: Moscoviense is a 640 km diameter, Nectarian-age, multi-ring impact basin on the lunar far side, centered at 26°N, 147°E. It contains the most prominent of the few mare deposits in that hemisphere and has a number of unique features that distinguish it from other lunar impact structures. Perhaps the most noted feature is the apparent offset of its ring structure, which has been proposed to be the result of either a single oblique impact [1] or the overlap of two unrelated impact basins [2]. Additionally, the lunar crust at Moscoviense has been modeled as thinner than anywhere else on the Moon [3], its floor displays large gravity and thorium anomalies [4], and Mg-spinel was identified in its innermost ring [5]. These characteristics illustrate the complexity of the basin's geology and how little is known about the specifics of its formation and modification.

Although Moscoviense has previously been mapped [6], the purpose of this project was to use more recent orbital data to compile an updated geologic map centered on the basin. A particular focus was placed on determining the shape and extent of ejecta deposits and on identifying material variations in the basin floor while separating out materials not related to the basin. Combined with structural mapping and compositional analysis, the map offers a new look at one of the Moon's most enigmatic basins.

Data & Methods: Mapping was completed in ArcMap 10.3.1 using geologic mapping methods outlined by [7] applied to several orthographically projected data sets. These data included a mosaic of LRO Wide Angle Camera (WAC) images, the Global Lunar DTM 100m topographic model (GLD100), and the Clementine Ultraviolet/Visible (UVVIS) color ratio map. Additional data including LRO Narrow Angle Camera (NAC) images were viewed in the online LRO QuickMap tool [8]. Color representations for units used established lunar mapping conventions.

In addition to the geologic map and accompanying correlation chart (Fig. 1), a structural map was made which outlines the rings of the basin and nearby topographic troughs.

In order to determine relative abundances of Fe, Ti, and Th, analyses were carried out in ArcMap using zonal statistics calculations for each mapped unit. The data used in these analyses were from Clementine FeO and TiO₂ maps and Lunar Prospector FeO and Th maps. Additional FeO measurements were collected for the

basin floor and ejecta deposits to better understand peculiarities in the initial results.

Geologic Map: The Moscoviense basin, material from surrounding basins, and overlying craters were mapped as 20 distinct units. Eight units make up the Moscoviense Group, which is divided into interior and exterior units. The basin interior contains massif and floor materials primarily distinguished by texture and albedo. A dark cratered floor unit (Nbfl) and a draped floor unit (Nbfd) inside the innermost ring abut against mare deposits. A light cratered floor unit (Nbfc) and rough floor unit (Nbfr) lie outside the partial inner ring, which itself is composed of massifs (Nbm).

In the outer basin, the rim (Nbr) is defined as the topographic high that constitutes the middle ring while the ejecta (Nbe) is characterized by lineated texture radial to the center of the basin. Though partly masked by heavy cratering on the far side highlands, secondary craters beyond the ejecta were also identified (Nbs). To the east of the basin, these secondaries tend to be in small clusters while to the west they are typically found in linear chains.

Three structural rings of diameters 180, 420, and 640 km were mapped and show a linear offset. A number of quasi-radial topographic depressions were identified around the basin, the largest of which trend to the northeast. These findings are consistent with structural mapping and oblique impact modeling by [9].

Unrelated to the Moscoviense basin impact are ejecta deposits of the older Freundlich-Sharonov (pNb) and younger Mendeleev (Nb) basins, pre- and post-basin crater ejecta (pNc, C, Cc, Cch), and several mare units. These include lower and upper mare lavas (Iml, Imu), pyroclastic dark mantling material (Idm), and units related to fractured deformation of crater floors (Icf, NIf). In addition, swirl deposits (Ims) are evident inside the western inner basin floor.

Interpretation: Compositional analyses of the units mapped yielded some noteworthy results. The dark cratered (Nbfl) and draped (Nbfd) basin floor materials have higher-than-expected concentrations of Fe and Ti, indicating a more mafic composition for the basin melt sheet than suggested by the composition of basin ejecta [10]. It was also found that post-basin craters on Nbfl have ejecta with higher Fe content than the surrounding material, suggesting the presence of more mafic material at depth there. This material may be early volcanic infilling or ultramafic mantle [11] which has since been mixed with Mendeleev ejecta.

Clementine maps show elevated FeO contents to the east and northeast of Moscoviense within the basin ejecta and rim deposits (Nbe, Nbr). A separate compositional analysis was carried out to quantify this difference and it was observed that the impactor that created the crater Steno Q appears to have excavated deep enough (1.7 km [8]) to eject highly anorthositic material from beneath the basin ejecta.

The mapping supports the interpretation that Moscoviense was created by an oblique impact from the southwest by documenting scoured topography to the northeast of the basin, a linear offset of its ring structure, and a compositional asymmetry of its ejecta deposit (Nbe). The maps do not show direct evidence in support for the alternative theory that Moscoviense consists of two distinct, nearly co-located basins.

Conclusions: New geologic and structural maps of the Moscoviense basin were compiled as well as related compositional analyses of mapped units. Basin ejecta

appears similar in bulk composition to the Orientale basin [12] and no unambiguous, unmodified basin melt deposits were found. This mapping project has identified more intriguing characteristics in this unique basin that may warrant further study.

References: [1] Schultz P.H. and Stickle A.M. (2011) *LPSC XLII*, 2611. [2] Ishihara Y. et al. (2011) *LPSC XLII*, 1124. [3] Wieczorek M.A. (2013) *Science* **339**, 671. [4] Thaisen K.G. et al. (2011) *LPSC XLII*, 2574. [5] Pieters C.M. et al. (2011) *JGR* **116**, E00G08. [6] Stuart-Alexander D.E. (1978) USGS Map **I-1047**. [7] Wilhelms D.E. (1972) USGS IR **55**, 47 pp. [8] <http://target.lroc.asu.edu/q3/#> [9] Schultz P.H. and Crawford D.A. (2016) *Nature* **535**, 391. [10] Spudis, P.D. and M.U. Sliz (2017) *Geophys. Res. Lett.* **44**, 1260. [11] Neumann G.A. et al. (2015) *Sci. Adv.* 1:e1500852. [12] Spudis P.D. et al. (2014) *Jour. Geophys. Res.* **119**, 19.

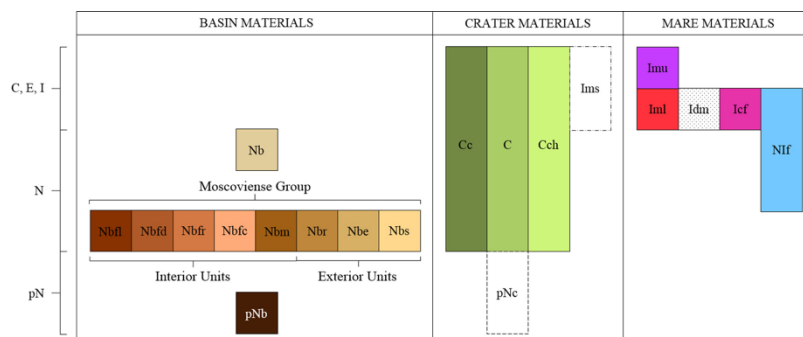
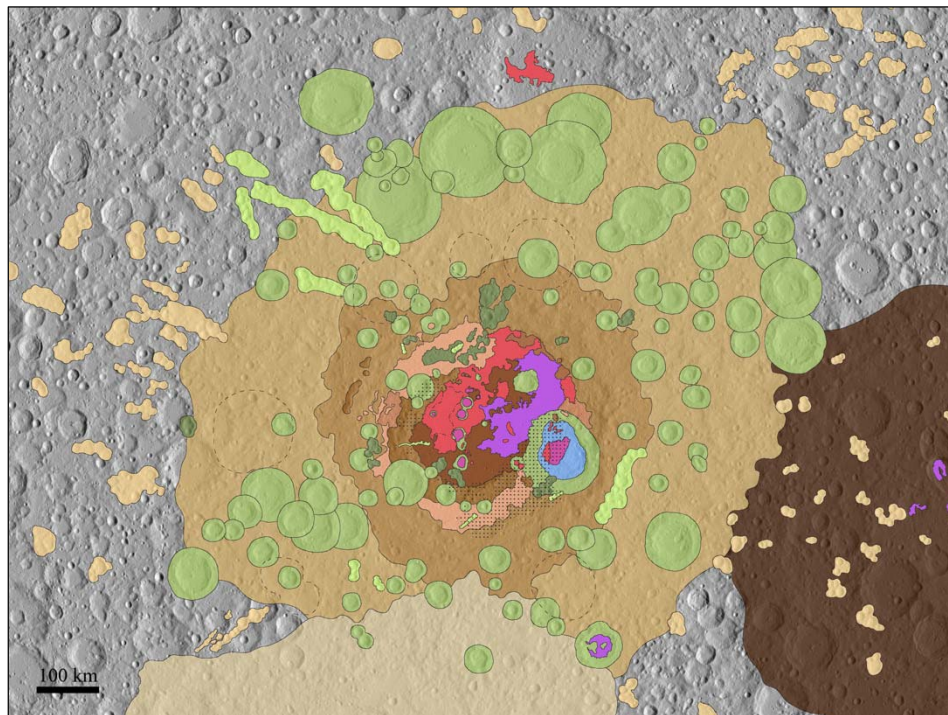


Figure 1 – New geologic map of Moscoviense basin centered on 26°N, 147°E with GLD100 hillshade basemap. Correlation chart at left shows relationships between units; relative ages are indicated to the left: C – Copernican, E – Eratosthenian, I – Imbrian, N – Nectarian, pN – pre-Nectarian.

GEOLOGIC MAPPING INVESTIGATIONS OF ALBA MONS, MARS. David A. Crown¹, Daniel C. Berman¹, Stephen P. Scheidt², and Ernst Hauber³, ¹Planetary Science Institute, 1700 E. Ft. Lowell Rd., Suite 106, Tucson, Arizona 85719 (crown@psi.edu); ²Lunar and Planetary Laboratory, University of Arizona, Tucson, Arizona 85721; ³Institute of Planetary Research, German Aerospace Center, Berlin, Germany.

Introduction: This study is designed to provide new constraints on the volcanic history and geologic evolution of Alba Mons. We are using imaging and topographic datasets to produce 1:1M-scale geologic maps of the summit region (245-255°E, 32.5-47.5°N) and western flank (230-245°E, 37.5-47.5°N). Age constraints for volcanic, tectonic, and erosional processes are being derived from detailed mapping of cross-cutting relationships combined with compilation and assessment of crater size-frequency distributions.

Background: Alba Mons is a large, low-relief volcano (1015 × 1150 km in planform; ~6 km relief) with low flank slopes (~1°) [e.g., 1-5]. Studies using Viking Orbiter images described the summit caldera complex, extensive lava flow fields, and prominent sets of circumferential graben [6-15]. Diversity in Alba Mons' lava flows was recognized in Viking Orbiter images, with a series of different morphologies described [6-7, 14-15]. Dendritic valley networks are observed on Alba Mons' northern flank [8, 16-19].

Data Sets and Mapping Methodology: Geologic mapping utilizes THEMIS, HRSC, CTX, and HiRISE images supported by HRSC and MOLA topography. GIS software and analysis tools are being used for the production of digital and hard copy USGS map products. The map bases includes 12 1:500,000-scale Mars Transverse Mercator (MTM) quadrangles.

Geologic Mapping Results: Mapping to-date [20-24] has utilized THEMIS IR and CTX data and includes: 1) Preliminary mapping of geologic features and examination of cross-cutting relationships in the summit region; 2) Systematic mapping of valleys (of likely fluvial origin) across both map areas; and 3) Systematic mapping of geologic features (volcanic, fluvial, tectonic, and impact) throughout the western flank map area. In addition, MOLA topographic datasets (DEM, slope maps with various baselines, and derived curvature statistics) are being integrated into mapping analyses to enhance topographic aspects of geologic features (lava tubes, valleys) whose primary morphologic/textural characteristics may be obscured by surface degradation.

Compilation of digital map layers that show the distribution of and interactions between volcanic, tectonic, erosional, and impact features have thus far yielded the following results regarding the geology of Alba Mons:

1) Mapping of erosional valleys indicates extensive degradation of the northern and western flanks of

Alba Mons [22]. Elongate drainage systems (with lengths of 300+ km) have dendritic to parallel morphologies. The correlation between valley distribution and local slope, and the occurrence of dendritic networks on the highest local slopes, suggest control by topography rather than variations in substrate properties [22].

2) The western flank of Alba Mons is dominated by numerous lava flows and lava tube systems. Their distribution is consistent with the broad shape of the volcano and local slopes (i.e., at 50 km scale), although flow paths have been deflected by local obstacles, including pre-existing craters and volcanic flows. Although local relationships are complex, lava flows generally seem to post-date adjacent lava tube systems.

3) Individual lava flows are typically elongate with relatively constant widths, although width variations, branching, and broader lobes are observed. Typical flow widths are ~2-10 km and numerous flow lobes extend for 100+ km in length. Lava tube systems can extend for 100s of km, are typically discontinuous, and are delineated by sinuous chains of elongate depressions, which in many cases are located along the crests of prominent sinuous ridges.

4) Cross-cutting relationships show that tectonic deformation post-dates volcanic and fluvial activity in the map area. Fluvial valleys dissect volcanic flanks materials, including specific lava flow surfaces, and frequently follow flow margins. Limited examples of lava flows embaying drainage systems are also evident. Mapped ejecta blankets superpose lava flows in some locations, and craters are observed to both truncate and be dissected by valley segments.

5) Preliminary age constraints from crater size-frequency distributions indicate a large pulse of volcanic activity across the western flank of Alba Mons between ~1.1 and 1.5 Ga. Our database of 12,000+ impact craters with diameters between 250 m and 18.3 km will be used for deriving relative and absolute ages.

References: [1] Pike RJ (1978) Proc. LPSC 9th, 3239-3273. [2] McGovern PJ et al. (2001) JGR 106, 23,769-23,809. [3] Plescia JB (2004) JGR 109, E03003. [4] Whitford-Stark JL (1982) JGR 87, 9829-9838. [5] Watters TR and DM Janes (1995) Geology 23, 200-204. [6] Carr MH et al. (1977) JGR 82, 3985-4015. [7] Greeley RG and PD Spudis (1981) Rev. Geophys. 19, 13-41. [8] Mouginitis-Mark PJ et al., (1988) Bull. Volc. 50, 361-379. [9] Cattermole P (1990) Icarus 83, 453-493. [10] Schneeberger DM and DC

Pieri (1991) JGR 96, 1907-1930. [11] Mouginis-Mark PJ et al. (1992) in Mars, Univ. Arizona Press, 424-452. [12] Hodges CA and HJ Moore (1994) USGS Prof. Paper 1534. [13] Crumpler LS et al. (1996) in Geol. Soc. Spec Publ. 110, 307-348. [14] Lopes RMC and CRJ Kilburn (1990) JGR 95, 14,383-14,397. [15] Peitersen MN and DA Crown (1999) JGR 104, 8473-8488. [16] Carr MH and FC Chuang (1997) JGR 102, 9145-9152. [17] Lehnigk KE (2016) <https://publish.wm.edu/honorstheses/934>. [18] Gulick VC and VR

Baker (1990) JGR 95, 14,325-14,344. [19] Hynek BM et al. (2010) JGR 115, doi:10.1029/2009JE003548. [20] Crown DA et al. (2017) LPSC XLVIII, Abstract #2301. [21] Crown DA et al. (2017) 3rd Planet. Data Workshop, Abstract #7034. [22] Scheidt SP et al. (2018) LPSC XLIX, Abstract #1570. [23] Karimova R et al. (2017) EPSC 2017, Abstract #EPSC2017-207. [24] Crown DA et al. (2018) LPSC XLIX, Abstract #1638.

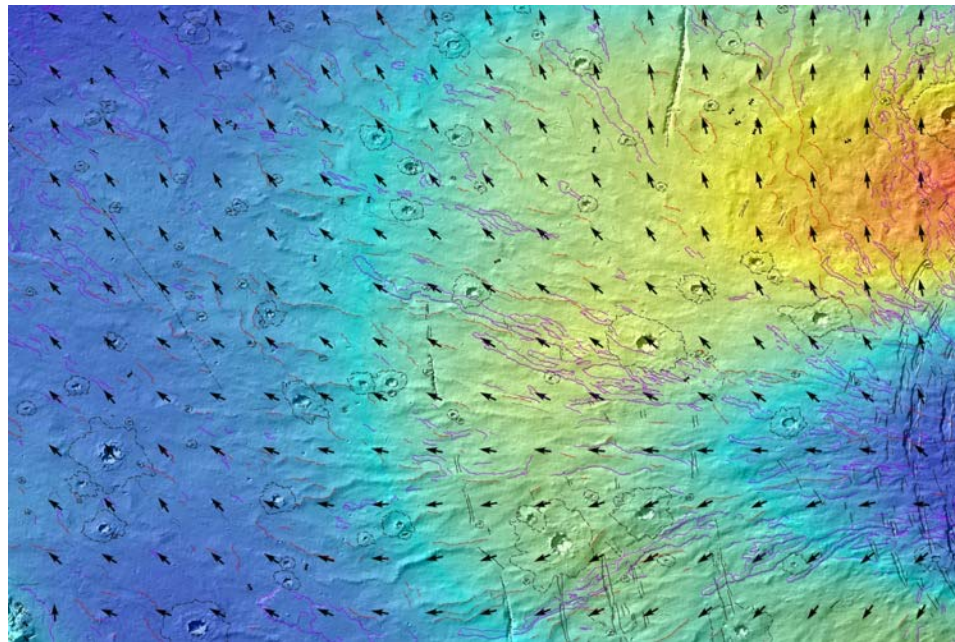
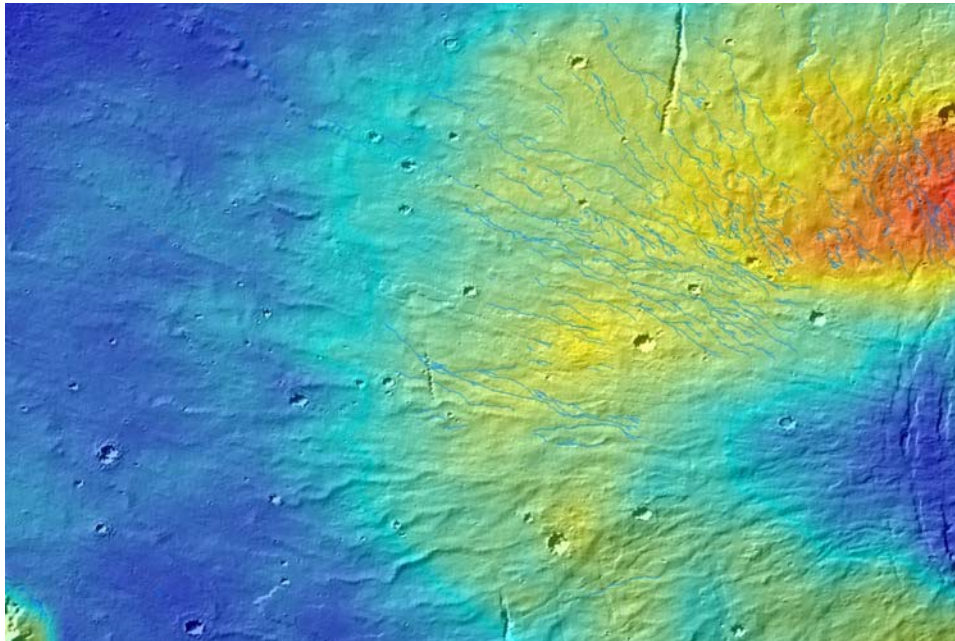


Figure 1. Western Flank of Alba Mons. Top) Average slope (25 km MOLA grid) over MOLA hillshade (463 m/pixel) with fluvial valleys in blue. Bottom) Average slope (50 km slope grid) over MOLA hillshade with mapped geologic features and maximum slope direction arrows. Average slopes values are calculated from resampled MOLA topography. Slope magnitudes and directions are calculated using a 3x3 kernel. Slope range is 0 (dark blue) to 2° (red). Figure widths are ~900 km. Note that locations of fluvial valleys are strongly correlated with higher slopes at 25 km scale (top) and that maximum slope values at 50 km scale (arrows) show strong agreement with lava flows (purple) and lava tubes (red) (bottom).

REMOTE SENSING CHARACTERIZATION OF SILOE PATERA, MARS. A. Emran¹, D. T. King Jr.¹, L. J. Marzen¹, C.W. Coker², and S. P. Wright³, ¹ Department of Geosciences, Auburn University, 2050 Beard Eaves Coliseum, Auburn, AL 36849 (aze0024@auburn.edu), ²EOG Resources Inc., Midland, TX 79706, ³Department of Geology and Environmental Science, University of Pittsburgh, Pittsburgh, PA 15260-3332.

Introduction: Siloe Patera, located on Arabia Terra (6.6° E, 35.2° N) on Mars, is identified as a nested deep depression with a depth of ~ 1,750 m as compared to its surrounding plains [1,4]. It has been characterized as steep-walled depressions linked by arcuate scarps and faults, which is akin to Eden Patera as described by Michalski and Bleacher [1]. A few studies investigated the topography and morphology of the patera and identified a subtle northeast southwest trending depression [1-3]. The southern depression reaches around most 700 m depth [1-4] and interprets it as evidence for sagging due to the demagnetization of crust indicating possible magma chamber at shallow depth [1,5]. Siloe Patera lacks direct evidence of impact ejecta around its structure and central uplift or peak, which are the typical characteristics of impact crater [1-4]. However, it has a southeastern emanating lobate flow, which is thought to be a set of lava or pyroclastic flow from 60 km of the rim [1]. Inside the nested crater, the irregular mound of friable materials is thought to be pyroclastic from volcano or as younger friable deposits of unknown origin [1,5].

However, a rigorous detailed interpretation of morphology coupling with thermal response (e.g. thermal inertia) of the surface materials are yet to be made. Thermal inertia (TI) on the Martian surface is an indicator of surface geological characteristics because surface physical properties, spatial distribution, and transportation of fine materials can be understood from the measurement thermal inertia [6-10]. A lower TI represents unconsolidated loose, fine surface dust, and very few rocks, a medium/intermediate TI means combination of cemented surface, sand sized particles, and a fair number of scattered rocks, whereas a high TI indicates rocky surface and bedrock outcrops [6-11]. In this study we try to interpret more details of surficial geology from combining morphology and thermal response (thermal inertia) of surficial materials of Siloe Patera using available high-resolution orbital dataset of Mars.

Methods: We use the mosaics of Mars Reconnaissance Orbiter (MRO) on boards Context Camera (CTX) [12] and daytime Thermal Emission Imaging System (THEMIS) [13], an instrument on boards the Mars Odyssey spacecraft, as primary base map for identifying surficial geology of Siloe Patera. In addition, MRO on boards the High Resolution Imaging Science Ex-

periment (HiRISE) [14] data and Mars Orbiter Laser Altimeter (MOLA), an instrument on boards the Mars Global Orbiter (MGO) were used as supplementary data, where possible. The study uses Mission Experiment Gridded Data Record (MEGDR) data of 128 pixel/degree for elevation information, which is a topographic map of Mars based on altimetry data acquired by the MOLA instrument and accumulated over the course of MGO mission. The surficial geology was inspected using the Java Mission-planning and Analysis for Remote Sensing (JMARS) program, a geospatial information system (GIS) developed by ASU's Mars Space Flight Facility, and ArcGIS. The thermal inertia is produced from nighttime thermal emission measurements of the Martian surface [15-16]. THEMIS nighttime infrared (IR) image (I37458005) is used to calculate thermal inertia. This study uses MARSTHERM, a thermophysical analysis tool [17], to derive thermal inertia using the method developed by Mellon et al. [18]. We used THEMIS data of higher spatial resolution (100 m per pixel) [13] which has more details spatial coverage than Thermal Emission Spectrometer (TES) (~3 km per pixel). The use of THEMIS enables us to more easily quantify the physical properties of morphologic features observed in high-resolution images since we use HiRISE and CTX on local scales.

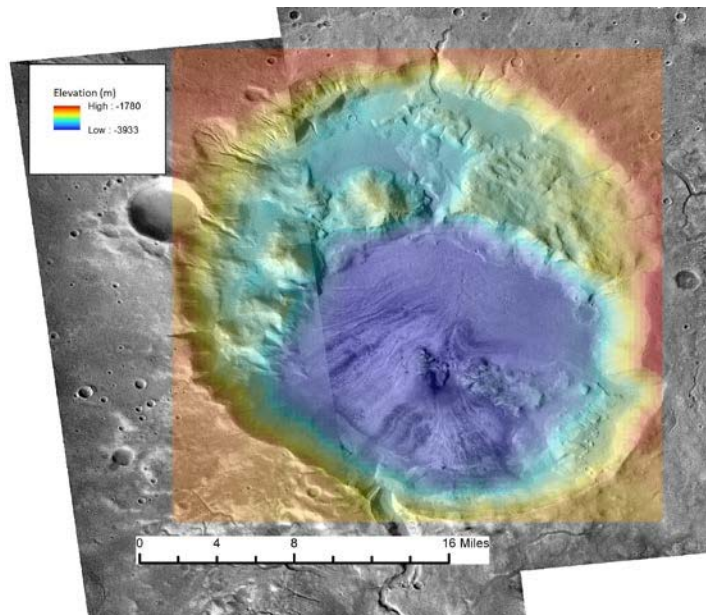


Fig. 1: MOLA elevation map overlain on CTX mosaic.

Results: With the mosaics of THEMIS, CTX, and HiRISE, we interpret Siloe Patera having few irregularly raised mounds along the scarp line of the bench with possible faulting along the north-eastern portion, possible flow features, many nearly parallel channels to its southwestern, east and southeastern, and east and northeastern rims, a large depression to the south, and an elongated mound on the floor of southern depression, referred here as a spire [1-4]. The irregular mounds along the fault scarp with clear individual peaks in MOLA data are thought to be divided by channels (Fig. 1). We assume that along the right side of the bench there is a series of concentric exposures appears to be ring faults which might be degraded and likely covered by layers of dust or ash, leaving little room for rock exposure [4]. The spire located on the floor of southern depression is broken into two parts with one isolated mound and an elongated mound. They extend and grade up in elevation until they connect to the southeastern wall of Siloe Patera (Fig. 1). MOLA elevation data shows that it is higher than the surrounding floor with elevations that rise toward the rim.

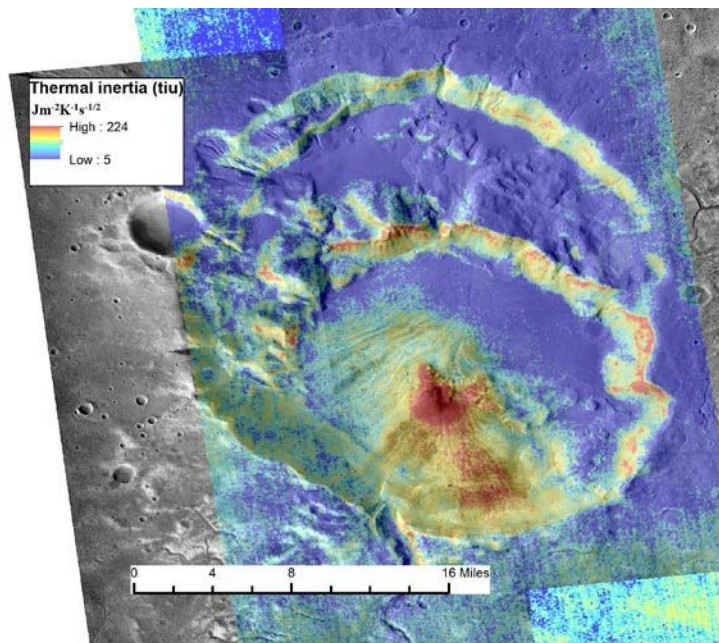


Fig. 2: THEMIS TI map overlain on CTX mosaic.

It appears to be a primary igneous feature, possibly an eroded cone or dike, rather than a clastic sedimentary deposit [4]. We do not find raised rim and any central morphology, like central peaks or central pit craters, which are common in many impact craters. Thermophysical variations (e.g. thermal inertia) often correspond to features identified in high-resolution images (e.g. HiRISE and CTX) and the integration of thermal

inertia enables to attain more robust conclusions [6-10]. Thermal inertia map shows that night time thermal inertia in Siloe Patera has a value minimum of $5 \text{ Jm}^{-2}\text{K}^{-1}\text{s}^{-1/2}$ to maximum $224 \text{ Jm}^{-2}\text{K}^{-1}\text{s}^{-1/2}$ (Fig. 2). Though our calculated thermal inertia from single measurement of THEMIS images and other complex factors e.g. uncertainties in the calibration of the THEMIS instrument which may not result exact quantitative thermal inertia values, the thermal inertia map presented here can be interpreted qualitatively to show the differences in local surficial materials in Siloe Patera. The interpretation is that the lower values areas in Siloe Patera have a lower apparent thermal inertia and likely represent fine particles, such as dust, silt, or fine sand whereas higher apparent thermal inertia surfaces may consist of coarser sand, surface crusts, rock fragments, bedrock, or a combination of these materials [8,18]. The thermal inertia from the surficial materials show distinct characteristics which follows elevation and local topography. We find higher thermal inertia on steep scarp and irregular rounded mounds of nested depression. A comparatively lower thermal inertia is found on most of the floor of depression which representative of dust materials probably from aeolian deposits. However, the higher thermal inertia in the southern depression is probably from the post volcanic lava or lobate deposition from the vent. We assume that the higher thermal inertia in the center of the southern depression is the probable vent of volcano, which might have obscured by surficial materials. The higher thermal inertia in the rounded mound part seems to represent presence of faulting which exposes bed rock materials.

References: [1] Michalski, J. R. and J. E. Bleacher (2013) *Nature*, 502 (7469): 47–52. [2] Wilkes, C.A. et al. (2013) *LPSC*, Abstract# 3034. [3] Wilkes, C.A. et al. (2014) *LPSC*, Abstract# 2271. [4] Wilkes, C.A. et al. (2014) *Unpublished MS thesis*, Auburn University. [5] Michalski, J. R. and J. E. Bleacher (2014) *AGU*, Abstract#P33E-03. [6] Jakosky, B. M. et al. (2000) *JGR*, 105 (E4), 9643–52. [7] Mellon, M.T. et al. (2000) *Icarus*, 148 (2), 437–55. [8] Putzig, N. E. et al. (2005) *Icarus*, 173 (2), 325–41. [9] Kieffer, H. H. et al. (1977) *JGR*, 82 (28), 4249–91. [10] Palluconi, F. D. and Kieffer, H.H. (1981) *Icarus*, 45 (2), 415–26. [11] Putzig, N.E. and Mellon, M.T. (2007) *Icarus*, 191 (1), 68–94. [12] Malin, M. C. et al. (2007) *JGR: Planets*, 112 (E5):E05S04. [13] Christensen, P. R. et al. (2004) *2001 Mars Odyssey*, 85–130. [14] McEwen, A. S. et al. (2007) *JGR: Planets*, 112 (E5):E05S02. [15] Jakosky, B.M. et al. (2006) *JGR*, 111 (E8), E0800. [16] Murphy, N. W. et al. (2007) *JGR*, 112 (E5), E05004. [17] Putzig, N.E. et al. (2013) *AGU*, Abstract #P43C-2023. [18] Mellon, M.T. et al. (2000) *Icarus*, 148 (2), 437–55.

DIGITAL GLOBAL GEOLOGIC MAP OF THE MOON: ANALYSIS TOOL FOR LUNAR RESEARCH. C. M. Fortezzo¹ and P. D. Spudis²; ¹U.S. Geological Survey, Astrogeology Science Center, 2255 N. Gemini Dr., Flagstaff, Arizona 86001 (cfortezzo@usgs.gov); ²Lunar and Planetary Institute, Houston, Texas.

Introduction: In 2013, we completed an initial digital renovation of the six 1:5,000,000-scale lunar geologic maps [1] (near, central far, east, west, north, and south sides) [2-7]. This renovation allows the older geologic maps to be overlain on newer, higher resolution datasets including the Lunar Reconnaissance Orbiter Camera Wide Angle Camera mosaic and the Lunar Orbiter Laser Altimeter digital terrain model. The renovations involved redrafting the line work from the previously published maps, with only minor reinterpretations.

We are currently in the final year of a project to create a seamless, globally consistent, 1:5,000,000-scale geologic map, a global correlation of map units, and their description of map units derived from the six digitally renovated geologic maps. The goal of this project is to create a resource for science research and analysis, future geologic mapping efforts, be it local-, regional-, or global-scale products, and as a resource for the educators and the public interested in lunar geology. Here we present the progress and ongoing efforts to complete this mapping project.

Methodology: Using geographic information system (GIS) software, we matched the boundary areas of the east side, central far side, and west side maps and cleaned the overlapping areas between the poles and near side maps. The east, central far and west maps have abutting boundaries which allowed units to simply be matched across the boundary. The polar maps overlap the boundaries of east, central far, west, and near side maps by 5 degrees. And finally, the near side map overlaps both poles and the east and west side maps to varying degrees given its irregular bounding shape. Within these overlaps, we have created a seamless boundary between the maps that respects the original authors interpretations and fits the concatenated global unit scheme.

There are 203 units across the 6 maps with some units exactly the same, some similar, and some completely unique. We have devised a global unit scheme that will allow us to more consistently stitch together the maps, display the units within the final global product, and correlate the units with respect to time and to each other. The current iteration of the map contains 51 globally consistent units; however, this number is subject to change as we internally review the map.

A NASA Space Grant student mapped the surface features in a consistent manner globally, something the original maps did not do consistently between

maps. These features include crests of crater rims, crests of buried crater rims, basin rings, grabens, mare wrinkle ridges, faults (generic unless type can be determined), rilles, and lineaments (a veritable potpourri of unidentified and/or indistinguishable linear features).

Datasets: The Lunar Reconnaissance Orbiter (LRO) Wide Angle Camera (WAC) global mosaic in the visible range provides 100% coverage, at 100 m/pix [8]. The LRO-Kaguya digital terrain model (DTM) covers from 60°N – 60°S, -180°E – 180°E at 60 m/pix [9]. The Lunar Orbiter Laser Altimeter digital terrain model covers the north and south poles at 20 m/pix [10]. All of these data are used in the stitching and mapping processes.

Year 2 progress: This year, we focused on getting the near side map incorporated. This was the first map that was renovated during the original project [1], and utilized the Lunar Orbiter global mosaic because the WAC mosaic was unavailable. As a result, the contact placement for the near side map has a significantly lower fidelity when compared to the other five rejuvenated maps. We redrafted the near side contacts using the WAC mosaic and LRO-Kaguya DTM. There were ~15,000 contacts in the original map, and between the overlapping areas with the north, south, east, and west side maps and the near side area there were >12,000 lines added. There is also an effort to thin the number of units from the original near side map as the scale of mapped units is incongruent with smaller units within the other five maps. Most of the units to be thinned will be smaller units, mostly craters, inconsequential for interpreting terrain evolution or establishing chronology of its surrounding unit.

The description of map units from each of the maps is also being concatenated into a single, succinct document that describes the unit features and interpretations from multiple authors. The descriptions will include type localities from each of the map areas from which the new unit is derived, will identify the original map's unique units, and will include the range of interpretations from the original maps as well as new interpretations from the existing literature.

The correlation of map units will be completed when the map is near completion and include the new units grouped by type with ages based on the original maps and recent changes documented in the peer reviewed literature.

Linear features mapped during the renovation of the original maps totaled ~1500 individual features,

with over one-third coming from the west side map. We have mapped ~3800 features globally. This consistent mapping will allow for analysis of feature types with geologic units, as well as with raster data sets.

Acknowledgements: This work is funded by a grant from the NASA PDART Program, award number NNH16AC361.

References: [1] Fortezzo, C.M. and T.M. Hare (2013) *Lunar Planet. Sci. Conf.*, Abst. #2114. [2] Wilhelms, D.E. and J.F. McCauley (1971) *Map I-703*,

USGS. [3] Wilhelms, D.E., et al. (1979) *Map I-1162*, USGS. [4] Lucchitta, B.K. (1978) *Map I-1062*, USGS. [5] Wilhelms, D.E. and F. El-Baz (1977) *Map I-948*, USGS. [6] Stuart-Alexander, D.E. (1978) *Map I-1047*, USGS. [7] Scott, D.H. et al. (1977) *Map I-1034*, USGS. [8] Robinson, M.S. et al. (2010) *Space Sci. Rev.*, v. 150, no. 1-4. [9] Barker, M.K. et al. (2016) *Icarus*, v. 273, pp. 346-355 [10] Smith, D.E. (2010), *Geophys. Res. Let.*, 37, L18204.

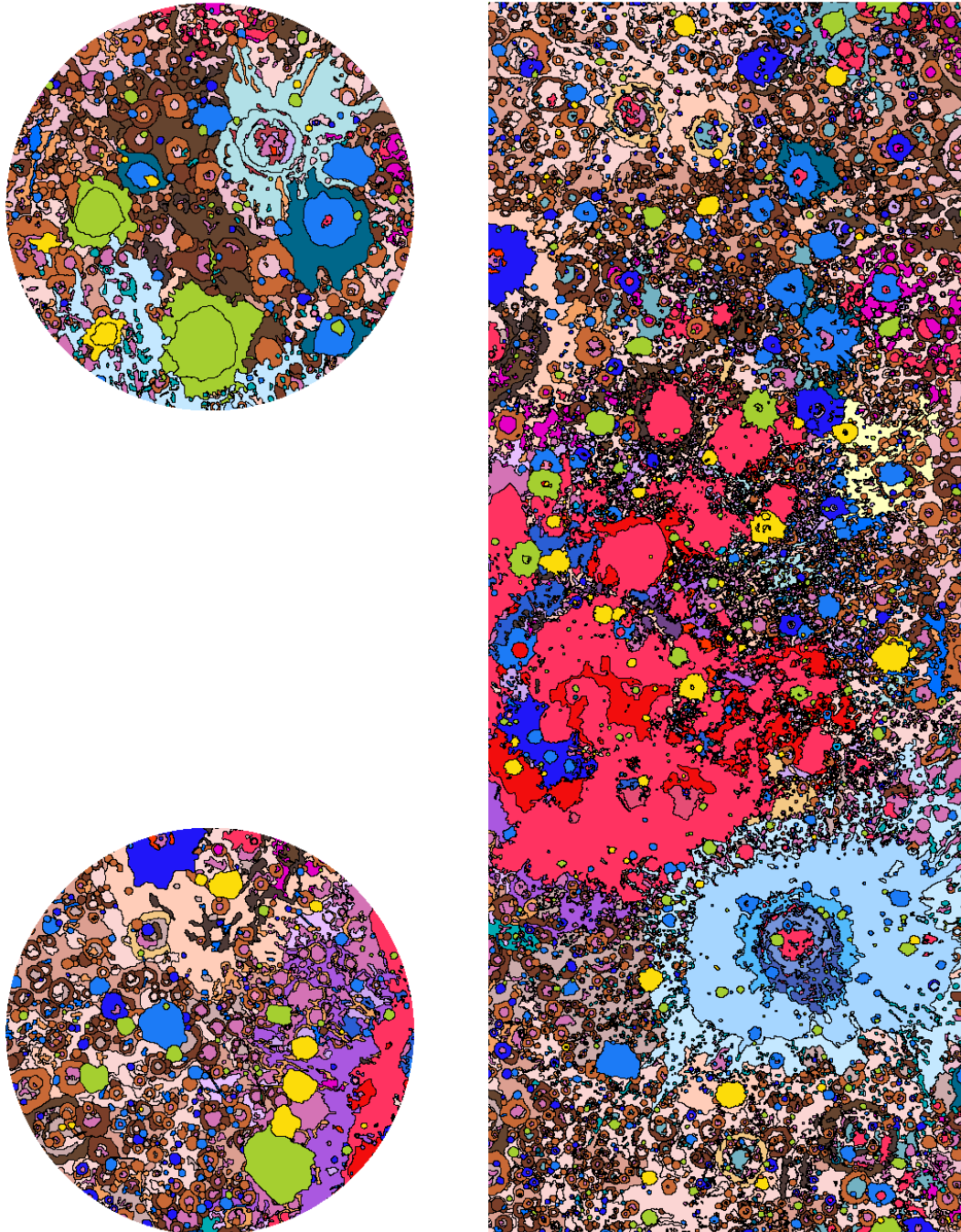


Figure 1: Global Lunar geologic units and contacts presented in Mercator projection with equatorial view from 57°S to 57°N and Polar Stereo Graphic projections showing the polar regions from 55°N-90°N (upper left) and 55°S-90°S (upper right). Mapped for 1:5,000,000 scale. As of the abstract, the map includes ~32,000 contacts and ~12,500 units.

UPDATING THE GEOLOGIC MAPS OF THE APOLLO 15, 16, AND 17 LANDING SITES. W. B. Garry¹, S. C. Mest², R. A. Yingst², L. R. Ostrach³, N. E. Petro¹, B. A. Cohen¹ ¹NASA Goddard Space Flight Center, Greenbelt, MD 20771, brent.garry@nasa.gov, ²Planetary Science Institute, Tucson, AZ, 85719, ³USGS Astrogeology Science Center, Flagstaff, AZ, 86001.

Introduction: Pre-mission geologic maps of the Apollo landing sites preserve a unique moment in the history of human space exploration - the initial interpretations of the lunar surface prior to exploration by the Apollo astronauts. However, these maps have not been formally updated in nearly 40 years despite the wealth of information from the astronauts' observations, post-mission sample analyses, and data from recent orbital missions. Creating new geologic maps that merge surface observations and recent remote sensing data will complete the cycle of exploration [1] initially started by the creation of the pre-mission geologic maps. Our team is funded through NASA's Planetary Data Archiving, Restoration, and Tools (PDART) program to produce two new U.S. Geological Survey (USGS) Special Investigation Maps (SIM) for the Apollo 15, 16, and 17 missions: a regional map (1:200K) and a landing-site map (1:24K).

Project Overview: Our project is 3 years (2018 to 2021) and is comprised of three main tasks:

Task 1. Digitize the pre-mission geologic maps of the Apollo 15-16-17 landing sites. There are no digital GIS files of the pre-mission geologic maps of the Apollo landing sites. The pre-mission geologic maps are historical records of the early thoughts scientists had about the lunar surface. However, there is no efficient way to compare these original maps with new lunar data sets in a registered GIS space. In year 1, we will digitize 8 maps to new LROC basemaps: the Apollo 15, 16, 17 (1:250K and 1:50K) pre-mission maps [2-7] and the Apollo 17 post-mission maps (1:250K and 1:25K) [8]. The GIS-ready files will be archived in the PDS Cartography and Imaging Sciences (IMG) Node in year 2.

Task 2. Create 6 new USGS SIM geologic maps of the Apollo 15-16-17 landing sites. The original USGS geologic maps for the Apollo 15, 16, and 17 missions provide the pre-mission assessment of the landing sites, but they were never systematically updated as a new series of official maps after the missions. We will integrate observations and interpretations from the past 40 years of each mission to make complete and thorough new geologic maps for the Apollo 15, 16, and 17 mission sites. The new regional (1:200K) and new landing site (1:24K) maps will be mapped at higher map scales than the pre-mission maps (1:250K and 1:50K) to take advantage of the resolution of the Lunar Reconnaissance Orbiter Camera (LROC) basemaps. The new map boundaries cover a similar or broader area than the original pre-mission regional geologic maps. For the new landing site maps, we selected map boundaries that are consistent with the post-mission traverse maps (1:25K) which do not include any geologic units, rather than boundaries of the pre-mission geologic maps (1:50K)

(Figs. 1-3). Therefore, the new landing site maps will cover a much smaller area than the pre-mission maps, but allow us to capture details of the surface observations along the traverse in the NAC basemaps. Lead mappers are: Apollo 15 (Garry), Apollo 16 (Mest), and Apollo 17 (Yingst).

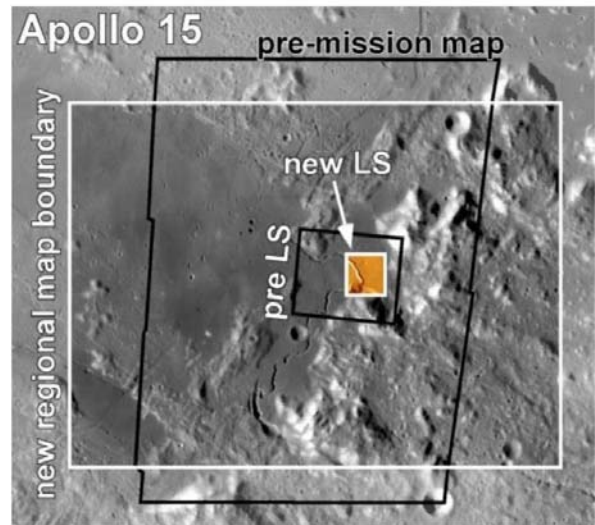


Figure 1. The new map boundaries for Apollo 15 (white boxes) are different than the pre-mission maps (black lines).

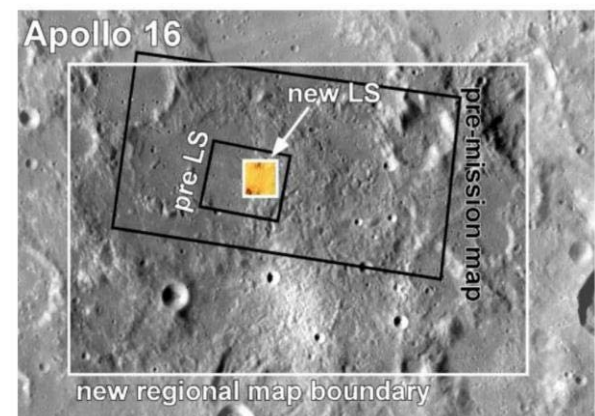


Figure 2. The new regional map boundary for Apollo 16 site covers a broader area than the pre-mission map. Boundaries for the new landing site (LS) map allow features along the traverse and distinct craters (e.g., South ray crater) to be mapped in more detail.

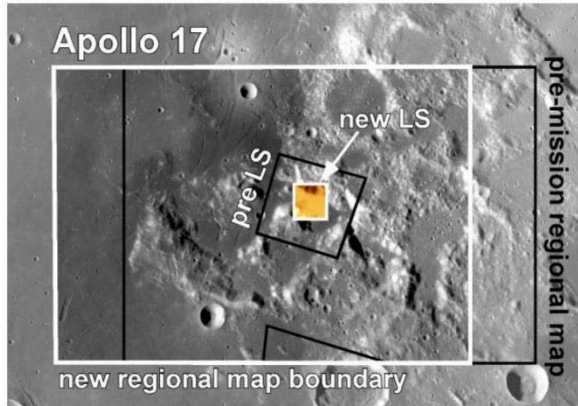


Figure 3. For Apollo 17, the new regional map boundary will cover a similar area as the original pre-mission map, but shifted to the west to cover volcanic units in southeastern Mare Serenitatis. The pre-mission landing site (LS) (black box) and new LS boundary (orange square) are shown in the center.

Task 3. Determine crater-derived ages for the new map units. Relative and absolute model ages of the geologic units mapped for each site will be determined by evaluation of stratigraphic relationships (superposition, embayment, and crosscutting) and through evaluation of crater size–frequency distributions. This task will be led by Co-I Ostrach. Our results will be compared to previously reported ages (crater densities and absolute model ages) [9-12]. We expect any discrepancies with earlier age estimates (i.e., based on pre-LRO images) to result from limitations in image resolution and illumination, which can strongly affect crater measurements [13], in addition to differences in defined count areas [11]. Co-I Ostrach will generate crater size–frequency distribution plots and calculate crater density to characterize crater populations. Crater plots and estimates of absolute model ages will be produced in the Crater-Stats2 software using standard cumulative and differential fit functions [14] in addition to incorporating newer error analysis [15].

Defining Map Units: The main types of geologic units we expect in the map areas are mare materials, highlands/massif materials, and crater materials. These general units are based on previous mapping and the common types of materials that were sampled during Apollo. Geologic units will be defined and characterized on the basis of morphology, albedo and surface textures, and topography.

Mare Materials. Contacts between mare materials will be drawn based on differences in albedo, color boundaries, textures, and crater density. Volcanic features such as sinuous rilles, domes, cones, and pyroclastic material will also be mapped as discrete geologic units or marked with linear attributes depending on the size and scale of the feature.

Highland Materials. Massifs in the mapping regions will be subdivided based on differences in morphologies, elevations, and compositions. Additional highland units will include talus/debris/mantling materials at the base of the mountains and landslides.

Crater Materials. For the 1:200K-scale regional maps, we will map craters down to 500 m. For the 1:24K-scale landing site maps, we will map craters down to 50 m.

Anticipated Results: Creating new maps will update original interpretations about the landing sites that were revised after the missions (e.g., initial interpretation of volcanic domes at the Apollo 16 site) [16]. While some interpretations of the pre-mission maps won't change, we anticipate the following changes in the new maps including the removal and/or addition of geologic units, and improvement in the location of contacts.

Apollo 15. We will use the LROC WAC high sun and the Clementine UV-VIS color-ratio mosaics to identify the distribution of ejecta from geologically fresh craters and subdivide the mare unit. These two data sets can also be used to define freshly disturbed areas on the massifs. On the new landing site map, we anticipate detailed mapping of Hadley Rille to include outcrops, contact of talus, and boulder tracks [17].

Apollo 16. A 1:200K-scale post-mission map [18] will serve as a foundation for our regional map. Several unit boundaries will change to reflect the new understanding of mounds initially interpreted to be volcanic domes that are now interpreted as ejecta deposits from Imbrium basin [16] and mapped as 'rugged terra material' on the post-mission geologic map [18].

Apollo 17. The updated regional map covers a smaller area than the original [6] regional map and changes several contacts and names of the geologic units. For example, three units (Cd, Imp, Im) in the original map located to the south of the Apollo 17 landing site were mapped as a single unit (Ib2) in [8].

References: [1] Hodges K.V. & Schmitt H.H. (2011) *GSA Special Paper*, 483, 17-31. [2] Carr M. H. and El-Baz F. (1971) Apollo 15 pre-mission map (I-723), *USGS* (1:250k). [3] Howard K.A. (1971) Apollo 15 pre-mission map (I-723), *USGS* (1:50k). [4] Milton D.J. (1972) Apollo 16 pre-mission map (I-748), *USGS* (1:250k). [5] Hodges C.A. (1972) Apollo 16 pre-mission map (I-748), *USGS* (1:50k). [6] Scott D.H. & Carr M.H. (1972) Apollo 17 pre-mission map (I-800), *USGS* (1:250k). [7] Lucchitta B.K. (1972) Apollo 17 pre-mission map (I-800), *USGS* (1:50k). [8] Wolfe E.W. et al. (1981) *USGS Prof. Paper 1080*, Plates 1 and 2. [9] Neukum G. (1983) thesis. [10] Neukum G. & Ivanov B.A. (1994) in Gehrels T. et al. *Hazards due to comets and asteroids*, 359 pp. [11] Robbins S.J. (2014) *EPSL*, 403, 188-198. [12] Bugliacchi et al. (2016) *Icarus*, 271, 30-48. [13] Ostrach L.R. (2013) Dissertation, *ASU*, 352 pp. [14] Michael G.G. & Neukum G. (2010) *EPSL*, 294, 223-229. [15] Michael G.G. et al. (2016) *Icarus*, 277, 279-285. [16] Muehlberger W.R. et al. (1972) *NASA SP-315*. [17] Gregg T.K. et al. (2012) *GSA*, abs.224-24. [18] Ulrich G.E. et al. (1981) *USGS Prof. Paper 1048*, 539 pp.

THE 1:1,000,000 GEOLOGIC MAP OF ARSIA MONS, MARS. W. B. Garry¹, D. A. Williams², A. M. Dapremont³ and D. E. Shean⁴ ¹NASA Goddard Space Flight Center, 8800 Greenbelt Rd., Greenbelt, MD 20771, brent.garry@nasa.gov, ²School of Earth and Space Exploration, Arizona State University, Tempe, AZ, 85287, ³Earth and Atmospheric Sciences, Georgia Institute of Technology, Atlanta, GA, 30331, ⁴College of Engineering, University of Washington, Seattle, WA, 98195.

Introduction: Arsia Mons, centered at 8.26°S and 239.1°E, is the southernmost edifice of the three Tharsis Montes volcanoes on Mars. Each volcano has a similar, overall shape and structure [1, 2], but there are distinct spatial distributions of morphologic features that hint each volcano has a slightly different evolution history [3]. To determine the differences between these three Martian shield volcanoes, we present a series of individual geologic maps of Arsia (this map), Pavonis [4], and Ascraeus Mons [5] based on high-resolution data sets to show their similarities and differences.

This 1:1,000,000-scale geologic map of Arsia Mons investigates the spatial distribution of geomorphic units, primarily volcanic and glacial in origin, to provide insight into the evolution of one of the largest and most expansive volcanic structures on Mars and in the solar system [6]. The objectives for our mapping project are 1) determine the areal extent and distribution of different lava flow morphologies across Arsia Mons to provide insight into the identified late Amazonian change in effusive style; 2) determine the areal extent and distribution of any glacial and aeolian deposits on the flanks and nearby plains and investigate their relationship to the lava flows; and 3) characterize the nature of presumed collapse and erosional features, such as rift zone graben and the channel networks, to determine their relationships to mapped volcanic features.

While only a snapshot of a localized region within Tharsis, the geologic map of Arsia Mons provides insight into the broader evolution of the Tharsis Rise and contrasting eruption styles on other volcanoes in the region [7-10], including Olympus Mons [11] and Alba Mons (previously named Alba Patera) [12].

Map Status: The 1:1M geologic map of Arsia Mons, the southernmost shield volcano of the Tharsis Montes on Mars is currently in revision for publication by the U.S. Geological Survey.

Data: Our line work and map units are referenced to the Mars Odyssey (MO) Thermal Emission Imaging System (THEMIS) daytime infrared (100 m/pixel) mosaic [13]. This mosaic reveals the appropriate detail at the published map scale of 1:1,000,000. However, the majority of our contact lines were informed by higher resolution supplementary data products including Mars Reconnaissance Orbiter (MRO) Context Camera (CTX) images (6 m/pixel) [14] and Mars Global Surveyor

(MGS) Mars Orbiter Laser Altimeter (MOLA) topography [15] that reveal morphologic details and spatial relationships appropriate for our mapping purposes.

Mapping Methods: Mapping was completed in ESRI's ArcMap™ 10.2. Line work was drawn at map scales of ~1:100,000 to ~1:50,000 with vertex spacing of 500 m and registered to the THEMIS daytime infrared base map. The final ArcMap project includes location features (points), linear features (lines), geologic contacts (lines), and geologic map (polygons).

Defining the Map Units: Our map of Arsia Mons is considered a morphologic map and not a traditional geologic map that defines litho-chronostratigraphic units of similar origin and time period. For example, we map the boundaries between lava ridges and lava fans on the main flank of Arsia, even though they may have similar ages to the undifferentiated flow fields, instead of defining the contacts based on craters counts/relative ages and origin. Our mapping style and unit definitions are based on the maps of individual HRSC frames that covered portions of all three Tharsis Montes completed by [3]. Map units are grouped based on their spatial distribution on geographic provinces of the volcano (summit caldera, flank, apron, plains, or fan-shaped deposit). The only units not defined to a specific geographic region are the crater units. Several units have essentially the same morphology (e.g., lava ridges mapped on the flanks, rift aprons, and lava plains), but we have created separate units defined by their geographic location.

Geologic History of Arsia Mons:

Noachian (4.1 to 3.7 Ga). There are no units interpreted or modeled as Noachian in age within the mapping area.

Hesperian (3.7 to 3.0 Ga). Based on stratigraphic succession and observations of HiRISE images, the relatively oldest layers in the mapping area are layers exposed within the walls of the summit caldera, the pits and chasms of *Arsia Chasmata*, and a graben at the base of the western flank [16] and are mapped as Asce and Ape. Ages for materials on Arsia have been previously mapped as Hesperian to late Amazonian in age [17, 18]. [18] suggests that main shield building for Arsia may have ended ~3.54 Ga, but their model ages for two locations on the lower flank near *Oti Fossae* are ~2Ga. While the main shield building probably began in the Hesperian, we have not cross-labeled our units as Hes-

perian in age to be more conservative in our interpretation and until a more robust set of crater-model ages can be determined for the main shield.

Amazonian (3.0 Ga to present). Our map units for the flank, apron, plains, glacial, and crater units are assigned early to late Amazonian ages, which may be inconsistent with previous mapping [17] and crater model ages for the main shield [18]. Main shield units are interpreted to have ended by mid-Amazonian, though units exposed in the walls (Asce) may be early-Amazonian in age. Textural differences between the apron and main shield and as well as the crater model ages by [18] suggest an age gap between eruptive episodes that formed the main shield and the plains and rift aprons. Accounting for this age gap, but also for the extensive nature of the rift apron and plains lavas, we interpret the apron and plains to be middle to late Amazonian in age consistent with crater model ages of the apron ~0.1 to 1.0 Ga [18]. Analysis of the glacial units (fan-shaped deposit) suggests the outer ridge units (Agr) are 200 to 745 Ma, which would mean the cold-based mountain glacier would have begun a final retreat during the late Amazonian [19, 20]. Exactly when the glaciers on the Tharsis Montes formed or if there were cycles of glacial and interglacial periods is not well-constrained. The glacial units may have stripped away the western flank of the main shield to reveal the older layers mapped as

the degraded units (Afd₁₋₄), but it is unclear if the glacier was there during eruptive episodes on the main flank as suggested by [21]. The youngest units in the map area are the most recent volcanic activity, late Amazonian in age, and are mapped as the caldera low shield and fissure units which may have been active ~130 Ma [22,23].

References: [1] Crumpler L. & Aubele J. (1978) *Icarus*, 34(3), 496-511. [2] Plescia J. (2004) *JGR*, 109, E3, DOI: 10.1029/2002JE00. [3] Bleacher J.E. et al. (2007) *JGR*, 112(E9), E09005, doi:10.1029/2006JE002873. [4] Garry W.B. et al. (2014) 45th LPSC, Abs. 2133. [5] Mohr K.J. et al. (2018) 49th LPSC, Abs. 2407. [6] Carr M. (1973) *JGR*, 78, 4049-4062. [7] Greeley R. & Spudis P. (1981) *Rev. of Geophys.* 19, 13-41. [8] Wilson L. et al. (2001) *JGR*, E-106, 1423-1433. [9] Bleacher J.E. & Greeley R. (2008) *JGR*, 113, B09208, doi:10.1029/2006JB004661. [10] Hauber E. et al. (2009) *JVGR*, 185, 69-95. [11] Bleacher et al., Olympus Mons map, in revision. [12] Crown et al. (2018) 49th LPSC, Abs. 1638. [13] Christensen P.R. et al. (2004) *Space Science Reviews*, 110, 85-130. [14] Malin M.C. et al. (2007) *JGR*, 112, E05S04, doi:10.1029/2006JE002808. [15] Smith D.E. et al. (1999) *Science*, 284, 1495-1503. [16] Mouginis-Mark P.J. & Rowland S.K. (2008) *Icarus*, 198, 27-36. [17] Scott D.H. & Zimbelman J.R. (1995) *USGS Atlas of Mars*, I-2480, scale 1:1M. [18] Werner S.C. (2009) *Icarus*, 201, 44-68. [19] Shean D.E. et al. (2007) *JGR*, 112(E3), E03004, doi:10.1029/2006JE002761. [20] Kadish S.J. et al. (2014) *PSS*, 91, 52-59. [21] Scanlon K.E. et al. (2014) *Icarus*, 237, 315-339. [22] Neukum et al. (2004) *ESA SP-1240*, 17-36. [23] Richardson J.A. et al., (2017) *EPSL*, 458, 170-178.

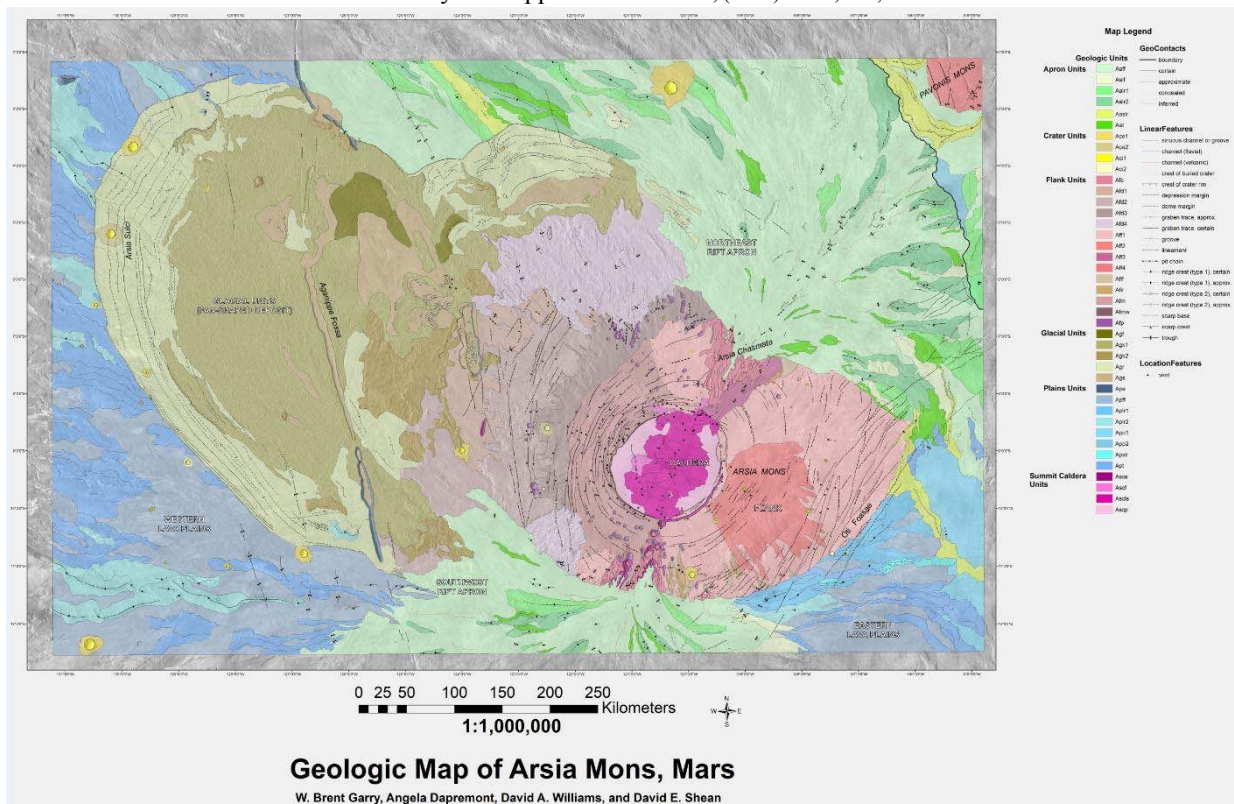


Figure 1. Geologic map of Arsia Mons submitted for review to the USGS in February, 2018.

GEOMORPHIC MAPPING OF LAVA FLOWS ON MARS, EARTH, AND MERCURY. K. B. Golder¹, D. M. Burr¹, ¹University of Tennessee Knoxville, Dept. of Earth and Planetary Sciences, 1621 Cumberland Ave., 602 Strong Hall, Knoxville, TN, 37996 (kgolder@vols.utk.edu).

Introduction: Volcanism has shaped the surfaces of the terrestrial planets, often associated with the emplacement of long lava flows. These flood basalts are typically characterized by extensive, thin sheet-like flows that inundate a large area, resulting in relatively smooth plains with features <100 m in height [1 and references therein], and exhibit a wide range of areal extents and volumes. Understanding the similarities and differences between the lava flows on each planet can offer significant insight into planetary evolution.

To advance understanding of flood basalts, we have undertaken mapping of lava flows on three planets, Mars, Earth, and Mercury, as part of three projects. The common purpose of each project is to investigate potential magma source locations and/or emplacement conditions. The datasets are specific to each body, whereas the technique of geomorphologic mapping is common to all the projects. Together, these projects highlight the utility of mapping across multiple planets.

Martian Magma Migration and Lava Flow Modeling: The focus on the lava flows in the Cerberus region on Mars (Fig. 1A) serves a twofold purpose. The first goal was to infer their magma source(s), through delineating the extent of three 1000+ km long lava flows and use their surface age relationships, derived from crater-counting techniques [2]. The channelized lava flows in Athabasca (AV), Grjótá (GV), and Marte Valles (MV) were emplaced with no discernable directional trend (Table 1), suggesting a magma source directly below the Cerberus region [3].

	GV	MV	AV
Ages collapsed to distal (youngest) age	31 Ma	8 Ma	3 Ma
Ages collapsed to proximal (oldest) age	53 Ma	43 Ma	3 Ma
Emplacement order for both approaches	1 st	2 nd	3 rd

Table 1: Size-scaled model ages and emplacement order for the channelized lavas. Regardless of the size-scaling approach, the emplacement order of these lavas does not change.

The second goal is the development of a cellular-automata based numerical lava flow model [4,5], to determine the controlling parameter(s) on the development of long lava flows on Mars. We will test whether the controls are either intrinsic [e.g., 6] or extrinsic to the lava [e.g., 7-9]. We will compare the modeling outputs to the observed extents of the martian lava flows. Prior to implementation on the martian

flows, we needed to test the model on terrestrial flows.

Terrestrial Analogues: Our work on two lava flows on Earth, the McCartys flow in New Mexico, USA, and the Laki flow in Iceland (Fig. 1B,C), is necessary to make comparisons to martian lava flows with similar inferred eruptive styles and morphologies. These terrestrial flows are typical examples of analogues for martian lava flows, particularly the channelized lavas in AV, GV, and MV [e.g., 1,10,11]. We are using these two flows to calibrate and validate the model prior to full implementation on the target martian lava flows. Early results suggest total erupted volume controls the emplacement of terrestrial and martian lava flows [4].

Origin(s) of Circum-Caloris Lavas: In our third project, we are investigating differences between the interior and exterior plains of the Caloris impact basin (CIP and CEP, respectively), and what these flows can tell us about their magma source(s). The CIP, CEP, and northern smooth plains (NSP) comprise the major relatively young volcanically emplaced features on Mercury [12]. These units are distinct from the more heavily degraded intercrater plains (IP), which are interpreted as an older volcanic unit [13].

The focus of our study is an expanse of smooth plains material northwest of Caloris (Fig. 1D) that exhibits apparent spectral differences associated with the high-reflectance red and low-reflectance blue materials [14,15]. By mapping the boundaries of these units, based on morphological and spectral properties, and age-dating them through crater counts, we seek to unravel their emplacement history, and infer the initial magma source. Initial results show two distinct lava units, based on morphology and spectral differences, though crater-count derived ages overlap.

Summary: Each of these projects relies heavily on accurate geomorphic mapping of lava flows. This mapping provides the foundation for the application of follow-on techniques, including inferring ages and source regions for the lavas.

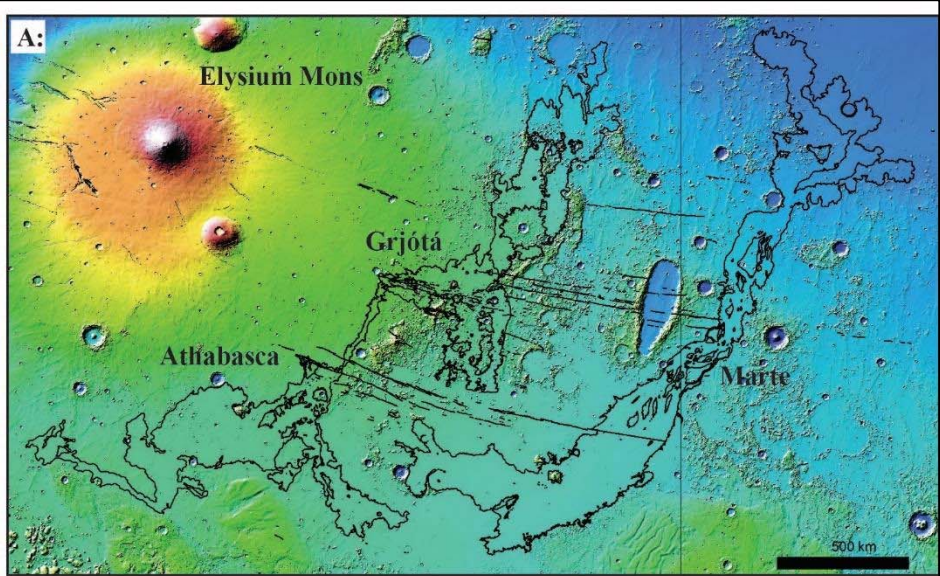
References: [1] Keszthelyi, L., et al. (2000), *JGR: Planets*, 105, 15027-15049. [2] Golder, K.B. and Burr, D.M. (2017) *LPSC XLVIII*, Abstract #2045. [3] Golder, K.B., et al. (2018) *in prep.* [4] Schiff, J.L. (2001) *Cellular automata: a discrete view of the world*. [5] Golder et al. [2018] *LPSC XLIX*, Abstract #1515. [6] Harris, A.J.L. (2013) *Lava flows. Modeling volcanic processes: the physics and mathematics of volcanism*, pp.85-106. [7] Walker, G.P.L. (1973) *Philosophical Transactions of the Royal Society of London*, 274, 107-118. [8] Hulme, G.

(1974) *JGI*, 39, 361-383. [9] Cordonnier, B., et al. (2015) *Geological Society, London, Spec. Pubs.*, 426, SP426-7. [10] Keszthelyi, L. et al. (2004) *GGG*, 11. [11] Bleacher, J.E., et al. (2010), *AGU Abstracts*, 1387. [12] Denevi,

B.W., et al. (2013), *JGR: Planets*, 118(5), 891-907. [13] Whitten, J.L., et al. (2014), *Icarus*, 241, 97-113. [14] Denevi, B.W., et al. (2009), *Science*, 324, 613-618. [15] Watters, T.R., et al. (2009), *EPSL*, 285, 309-319.

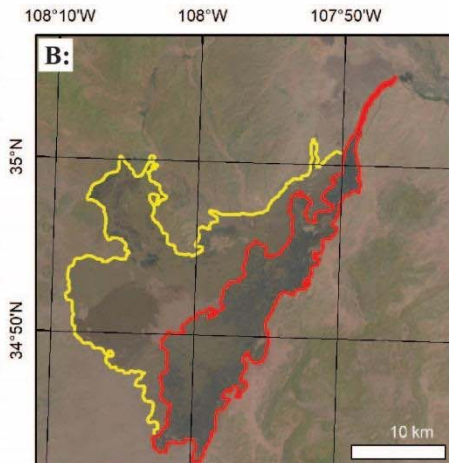
Figure 1:
Mars

A: Map of the channelized lavas in the Cerberus region, Mars. These lavas were studied to determine their age of emplacement, to infer magma migration pathways. Athabasca and Grjótá Valles are the sites chosen for numerical modeling, as their source regions are easily identifiable, and their extents have been well defined. MOLA topography base, where warm colors are highstanding, and cool colors are low-lying.

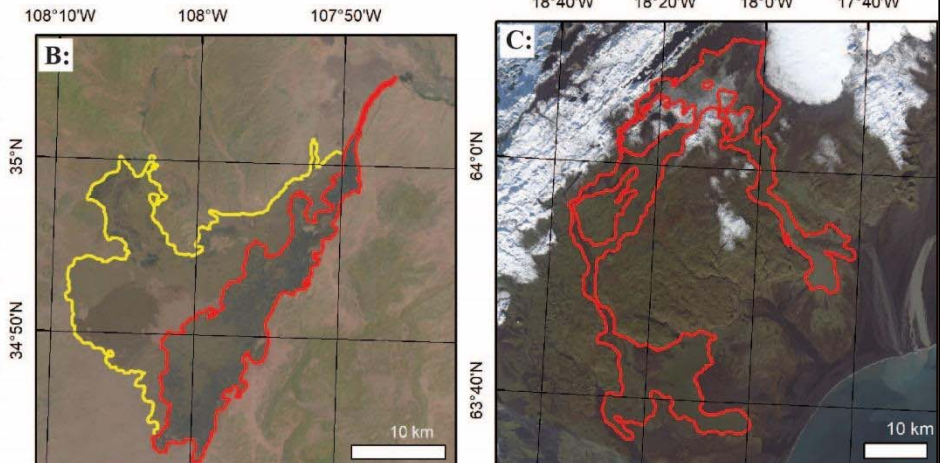


Earth

B: Areal extent of the Zuni-Bandera lava flow field (yellow), with the overlying McCartys flow (red) in New Mexico, U.S. Landsat 7 basemap.



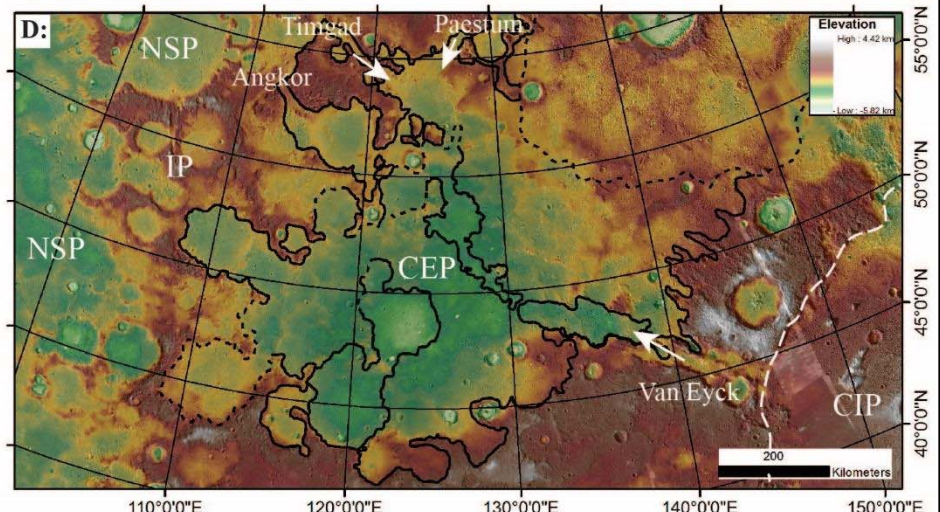
C: Areal extent of the Laki flow field (red) in Iceland. Landsat 8 basemap.



These two flows are the sites used to calibrate and validate the numerical model in development.

Mercury

D: Regional context image, centered on the northwest CEP study area, with unit contacts (black). The CEP are bounded by the NSP and CIP, with possible lava flows paths denoted by white arrows. MLA topography base, where warm colors are highstanding, and cool colors are low-lying.



COMPLETION OF THE 1:1,500,000-SCALE GEOLOGIC MAP OF WESTERN LIBYA MONTES AND NORTHWESTERN TYRRHENA TERRA. A. E. Huff and J. A. Skinner, Jr., U.S. Geological Survey, Astrogeology Science Center, 2255 N. Gemini Dr., Flagstaff, AZ, 86001 (ahuff@usgs.gov).

Introduction: The rugged, densely-cratered terrains of the Martian highlands are separated from the smooth, less-cratered plains of the Martian lowlands by a roughly globe-encircling, ~50 to 600 km wide band of transitional units that define the highland-lowland transition zone (HLTZ) [1]. This transition zone predominately lies in the northern hemisphere and distinctly lacks a defining scarp feature. Instead, the HLTZ is represented by zones of gradation from cratered highlands to fragmented mesas, plateaus, and knobs to detrital plains (type area: Deuteronilus Mensae). The HLTZ deviates from this characteristic morphology in various places. For example, the Tharsis province where the HLTZ is obscured by superposed volcanic deposits, the Nepenthes Mensae where local volcanics have embayed highland knobs and plateaus and lowland plains to extend the HLTZ to 1000+ km, and the Libya Montes region where the Isidis impact has influenced the evolution of the HLTZ by impeding the development of transitional units.

Deuteronilus Mensae, and the common morphologies of the HLTZ, and Nepenthes Mensae have been mapped and documented in the Geologic Map of the Northern Plains of Mars [2] and the Geologic Map of the Nepenthes Planum Region, Mars [3], respectively. To contribute to the understanding of the formation, evolution, and preservation of the HLTZ and its implications for early Mars conditions, we have generated a 1:1,500,000- (1:1.5M-) scale geologic map of the third observed type of the HLTZ in Libya Montes. We mapped the morphology changes from the Martian highlands in northwestern Tyrrhena Terra to the transitional units of western Libya Montes in order to better constrain the influence of the Isidis impact on the evolution of HLTZ geologic units in the area. Our map region includes distal Syrtis Major lava flows that embay Libya Montes and a section of the north-directed, well-integrated channel systems of Zarqa Valles that is sourced from Oenotria Cavi. The cratered terrains of Tyrrhena Terra include low-lying plains (Oenotria Plana) and Isidis-circumferential scarps (Oenotria Scopuli). We mapped at 1:300k using a THEMIS nighttime IR controlled mosaic as the primary map base supplemented with MOLA and CTX data.

Unit Determination: We identified and mapped four groups of geologic units: Transitional Province (1 unit), Volcanic Province (1), Highland Province (8), and Widely Occurring Units (4). The Transitional Province consists of the Zarqa plains unit (HNzp) that

is a smooth, planar unit with isolated and connected channel segments and elongate, smooth interior plateaus; located in interstitial topographic lows between Libya Montes massifs and contains sections of Zarqa Valles. The Volcanic Province consists of the Syrtis volcanics unit (Hsv) that is a planar unit with elongate crenulated-ridges and lobate scarps located in Syrtis Major Planum and which embayed Libya Montes and Zarqa Valles drainages. The Highland Province consists of the Oenotria Cavi unit (Hoc), Oenotria plains 3, 2, and 1 units (HNop₃, Nop₂, and Nop₁), Tyrrhena terra 3, 2, and 1 units (Ntt₃, Ntt₂, and Ntt₁), and Tyrrhena massif unit (Ntm). Unit Hoc is smooth, planar unit with northwest-southeast trending lineaments and is located in Oenotria Cavi. Unit HNop₃ is a planar unit with reticulate troughs and lobate scarps and bounds Oenotria Cavi. Unit Nop₂ is a broadly planar unit that includes interior and marginal lobate scarps, which embays older plains units and higher-standing terra units and is located within Oenotria Plana. Unit Nop₁ is a mottled-tone planar unit with 100's meter-scale swales, scarps, and undulations, and it is an isolated plains unit within and adjacent to terra units. Unit Ntt₃ is a smooth, gently-sloping unit with pervasive narrow downslope linear furrows and channels that formed aprons at massif bases in and around Libya Montes. Unit Ntt₂ is a smooth to hummocky unit above the rugged and heavily dissected unit Ntt₁ which occurs throughout Tyrrhena Terra. Unit Ntm is a topographic promontory unit that grades from equant, dome-like outcrops to elongate outcrops with axial spines and valley-and-spur morphologies and are located throughout Tyrrhena Terra and define Oenotria Scopuli.

The Widely Occurring Units consist of the Crater 3 unit (c₃), Crater 2 unit, Crater 1 unit, and Crater smooth unit (cs). Unit c₃ is an impact basin unit with sharp, continuous, asymmetric ridges bounding bowl-shaped basins that have radial material continuously blanketing the exterior of the ridge. Unit c₂ is an impact basin unit with subdued, semi-continuous asymmetric ridge bounding semi-bowl-shaped basins that have radial material semi-continuously blanketing the exterior of the ridge. Unit c₁ is an impact basin unit with poorly-defined ridges partially bounding a flat-floored basin with no radial material blanketing the exterior of the ridge. Unit cs is a flat unit within unit c₁ that commonly has scarps and ridges.

Age Determinations: We primarily focused on the geologic principle of cross-cutting relationships aug-

mented with relative crater size-frequency distributions (SFDs) in order to determine unit ages in our study area. Contact relationships between geologic units were used to inform relative stratigraphic ages for the correlation of map units (COMU), and crater density measurements were used to assign Martian epochs on the basis of relative model ages.

We identified 2757 primary craters ranging from 0.26 to 92.51 km in diameter which were used to evaluate crater SFDs, per the methods of Werner and Tanaka [4] using the Ivanov chronology [5]. During mapping, associated crater units were mapped for craters larger than 5 km in diameter. To properly determine crater SFDs, the identified crater data points needed to be associated with the geologic unit polygons that was impacted, or else retention of the crater units would have caused the calculated crater SFDs to be anomalously young. Therefore, we merged all four crater units to the surrounding geologic units mapped. In instances where a crater unit was mapped in contact with two or more units, we consistently split units evenly with straight lines depending on extrapolated contact geometries. However, for some craters proximal to unit boundaries, this method resulted in incorrect assignments of geologic units. For example, the location of the crater data point was not on the correct side of a split crater unit or a crater data point was included in a unit that resurfaced the crater. This issue potentially caused the SFDs to report anomalously old relative model ages for the volcanic units (Nop₂ and Hsv). To investigate and counteract this problem, we examined individual craters on the geologic map and adjusted center point locations (used to mark the geologic unit in which the crater formed) or selectively excluded them (for cases where the crater had been subjected to resurfacing) to quantitatively evaluate the impact this problem has on this technique of epoch assignment.

Geologic Summary: Based on the cross-cutting relationships, the correlation of map units (COMU), and crater age determinations, the geologic units and events in this study area span early Noachian to early Amazonian. After emplacement of the ancient Martian highlands during the Early Noachian, the Tyrrhena terra units began amalgamating in the Middle Noachian. The Isidis impact occurred within the Middle Noachian and caused crustal uplift resulting in exposures of highlands materials as massifs (Ntm) and scarps (Oenotria Scopuli). At the onset of the Late Noachian, unit Ntt₃ deposited as aprons surrounding Libya Montes massifs and channelization in the southern map portion of Tyrrhena Terra initiated exposition of older unit Ntt₁. Concurrently, younger plains (Nop₁) were being deposited in fluvial systems within topographic lows throughout

Tyrrhena Terra. In Oenotria Plana, planar units, likely low viscosity lava flows (Nop₂), embayed higher standing terra and scarps, covering most of unit Nop₁ in this area. In the north, the Zarqa Valles channel system was periodically active from the Late Noachian to the Late Hesperian, resulting in pool and riffle sequences within Tyrrhena terra and floodplain deposits and erosional terraces within Zarqa Valles (HNzp). Transitioning from the Noachian to Hesperian, lava or sediment flows, possibly erupted from fissures, were deposited and subsequently modified to form Oenotria Cavi. Early Hesperian distal flows from Syrtis Major embayed Tyrrhena Terra and abutted Libya Montes, and interacted with the Zarqa Valles channel system resulting in a volcanically hijacked fluvial channel that was dissected by later fluvial activity, demonstrating the oscillation (and close association) between volcanism and fluvial activity.

Discussion: The rugged and evolved terrains of the Martian highlands are difficult to map, interpret, and place in geologic context because of extensive cratering, prolonged and varied influences of multiple, simultaneous geologic processes, including impacts and volcanism. Adding to this, the HLTZ lends to the poor preservation of contact relationships between the highlands, transitional, and lowlands unit progressions due to the confluence of highland and lowland deposition and alteration processes. Our mapping characterizes the Isidis-related HLTZ and uses cross-cutting principles and crater age determinations to shed light on the complicated contact relationships and ambiguous correlations between cratering and true surface ages that are characteristic of the Martian highlands and the HLTZ.

References: [1] Tanaka, et al. (2014) *USGS SIM* 3292, 1:20M scale. [2] Tanaka, et al. (2005) *USGS SIM* 2888, 1:15M scale. [3] Skinner and Tanaka (2018) *USGS SIM* 3389, 1:1.5M scale. [4] Werner and Tanaka (2011) *Icarus*, v. 215, pp. 603-607. [5] Ivanov (2001) *Space Sci. Rev.*, v.96, pp. 87-104.

Acknowledgements: This work is supported by NASA's Planetary Geology and Geophysics Program under award No. NNH09AK421.

DEVELOPING AN APPLICATION TO INCREASE THE ACCESSIBILITY OF PLANETARY GEOLOGIC MAPS. R. E. Jacobsen¹, C. Fay² ¹Earth and Planetary Sciences Department, University of Tennessee, Knoxville, TN, 37996 USA (RJacobse@vols.utk.edu), ²Lee University, (cb.fay@icloud.com).

Introduction: Planetary geologic maps published by the United States Geologic Survey (USGS) are widely used digital products for communicating and facilitating scientific analyses of other planets [1]. These maps include text, graphics, raster, vector, and temporal data, all within a highly standardized design (Fig. 1). However, the framework or layout design of these diverse data formats is cumbersome to navigate. We are developing a java-based application to augment the map user's experience and improve accessibility among the rich and diverse forms of data within USGS planetary geologic maps.

Opportunity: The USGS Publication Warehouse is the PDS-equivalent, long-term data archive for USGS planetary geologic maps [1,3]. Numerous planetary geologic maps are available for download as portable document files (pdf) and GIS geodatabases. However, viewing all the rich and diverse information contained within a geologic map is impractical without access to the print version. Often times, the user (e.g., the first author) must repeatedly navigate between the map (raster & vector data) and the Description of Map Units (DOMU, text data) or the Correlation of Map Units (COMU, temporal data) in order to view all the available information. The repeated navigation between the various forms of data represents an opportunity to improve the accessibility among all types of

data on USGS maps.

Tool Concept: Viewing the map base, map units, DOMU, and COMU together would improve accessibility in the map user's experience. To view these data together, we envision a tool that presents the map base and map units. A dynamic legend will show unit information (e.g., box with text) when the cursor is positioned over a geologic unit. Finally, we envision a scroll function for turning on and off units depending on their position in the COMU. This functionality will improve the accessibility of chronological information.

Software design: The application's development process can be broken into three sub-processes:

- 1) Writing "widgets" that give users control of how information is displayed in a browser environment.
- 2) Styling and arranging visual components to be intuitive and aesthetically pleasing to users on any device.
- 3) Establishing a tight and flexible hierarchy that will contain the application's individual components, and facilitate scalability.

The application will be built with Javascript and Python and use a Django web framework.

References: [1] [Skinner et al. \(2018\) USGS](#). [2] Hynek & Di Achille (2017) USGS SIM 3356. [3] USGS Publications Warehouse <https://pubs.er.usgs.gov/>

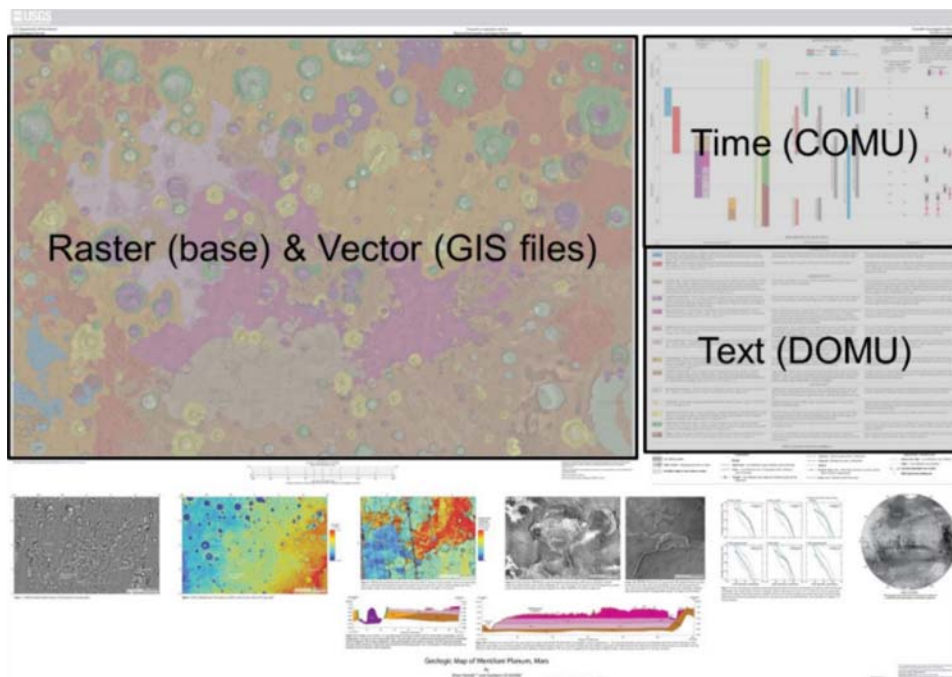


Figure 1: The 1:2,000,000 geologic map of Meridiani Planum, Mars [2] with labels for the various data format on a standard USGS geologic map. The proposed application will help the map user access these various forms of data.

UNDERSTANDING THE HISTORY OF A DIVERSE INVERTED LANDSCAPE: SUMMARY AND PLAN FOR FINISHING THE 1:500K GEOLOGIC MAP OF AEOLIS DORSA, MARS. R. E. Jacobsen¹, D. M. Burr¹, R. M. Borden¹, S. E. Peel¹, and A. S. Boyd¹ ¹Earth and Planetary Sciences Department, University of Tennessee, Knoxville, TN, 37996 USA (RJacobse@vols.utk.edu and dburr1@utk.edu).

Introduction: This abstract summarizes our fourth year's work on a 1:500k USGS geologic map of the Aeolis Dorsa (AD) region, Mars [1-3] and compares the work done to the recently released Planetary Geologic Mapping Protocol-2018 (PGMP) [4; see link]. Finally, this abstract presents a plan for completing the map package for submission and review.

The AD region is located north of the Highland-Lowland Boundary (HLB), ~800 km east of Gale Crater, and south of the Cerberus lavas [Fig. 1A]. The primary focus of the proposed work has been to investigate thousands of sinuous ridges, interpreted to be inverted fluvial features [5,6 and refs. therein]. Fortunately, the great diversity of landforms in AD has motivated additional investigations of geomorphic processes, e.g., lacustrine processes, tectonics/collapse processes [7], and aeolian processes associated with the Medusae Fossae Formation (MFF) [e.g., 8].

Scientific results from mapping: The stratigraphy and paleohydrology of the AD deposits were analyzed to elucidate the history of fluvial activity in the region. The larger Martian hydrologic timeline, is encapsulated in the stratigraphy of Aeolis Dorsa, particularly in the transition from wide meandering fluvial deposits and channel fills to alluvial fans [9-11 and refs. therein]. Close examination of AD deposits and comparisons with terrestrial analogs suggest meandering fluvial and debris-flow deposits formed only in southern AD and in the presence of weathered sediments [10]. The presence of these deposits and weathered sediments in southern areas, and their absence in northern areas, suggests enhanced weathering in the south possibly caused by orographic precipitation near the HLB [5,10]. Results from additional analyses of AD deposits and comparisons with terrestrial analogs improve the accuracy and precision of empirical relationships for estimating paleodischarges on Mars [12]. Results from morphometric analyses of meander scrolls in the AD region and comparisons with terrestrial analogs suggest confounding factors in the interpretations of eroded fluvial deposits [13].

Several craters in the AD region preserve post-impact sedimentary deposition [9]. Close inspection of these intra-crater deposits suggests branching ridges and layered outcrops, among others, are consistent with deltaic deposits and sedimentary deposition in lacustrine and near-lacustrine environments [14].

The AD region hosts numerous tectonic features [7,9]. A large "southern depression" separates AD

from the southern highlands and is interpreted to have formed by extension along the HLB [15]. Wrinkle ridges are observed throughout the AD region and have NE-SE orientations evidencing compressive stresses [16] possibly from loading of lavas at Elysium.

The AD region includes abundant aeolian landforms, e.g., dunes and yardangs [1-3]. Many of these features have been associated with the widespread MFF [8]. However, the relationship between the MFF and dark sands in the AD region is enigmatic. Examination of high-resolution visible-wavelength images suggest that dark sands cluster in the southern depression and adjacent to Aeolis and Zephyria Plana [17]. These locations are consistent with the only two visually confirmed outcrop sources of dark sand, the southern highlands and the MFF [17].

Protocol: The recently released PGMP-2018 presents expectations for standardized geologic maps, published by the USGS [4]. Map packages must include GIS files, a geologic map, Description of Map Units (DOMU), Correlation of Map Units (COMU), Explanation of Map Symbols (EOMS), map text (pamphlet), figures, captions, and tables [4].

Status of map package: The GIS files and the geologic map are nearly complete [Fig. 1B]. GeoContacts, with validated topology, have been placed throughout the map area and outline 19 map units. There are 10 different linear feature types, mapped over crater features, tectonic features [16], and fluvial features [10]. The DOMU and COMU have been drafted [18; [see poster for full unit descriptions](#)].

Mapping results show Noachian to Hesperian-age highlands moderately deformed by impact cratering, and transitional units deformed by extensional tectonics [15]. These units are interleaved with richly stratified plana units of aeolian and volcanoclastic origins (i.e., MFF). Plana, highlands, and transitional units hosted widespread fluvial and lacustrine deposition and waning hydrologic activity during the Hesperian and Amazonian periods [5,10,14,18]. Later, fluvial and lacustrine deposits were repeatedly buried by widespread aeolian and/or volcanoclastic deposition (MFF), and subsequently exhumed by aeolian processes, forming yardangs and aeolian bedforms [8,17].

Finishing the map package: A new basemap built from blended CTX images has been incorporated into the mapping project [19]. A coordinate system file will be included with the new basemap. The locations of some GeoContacts and features need editing to align

with the new basemap. Editing location features and surface features is ongoing. Type locations and additional characteristics are being added to the DOMU. A separate table of stratigraphic contacts and their locations will augment the COMU; and, an EOMS will be drafted this summer.

These edits and changes are being made by REJ. At the end of July 2018, GIS files and the map will be transferred to DMB, who will review the content in dialog with co-authors and write the map text. REJ will assist with map text figures, captions, and tables. DMB will then coordinate with USGS on map package submission, compliance review, technical review, and Map Coordinator review, to be completed in 2019, with a first No Cost Extension to the supporting grant.

References: [1] Burr & Jacobsen (2015) *Planet.*

Mappers Meet., Honolulu, HI. [2] Burr et al. (2016) *Planet. Mappers Meet.*, Flagstaff, AZ. [3] Burr et al. (2017) *Planet. Mappers Meet.*, Flagstaff, AZ. [4] [Skinner et al. \(2018\) USGS](#). [5] Burr et al. (2009) *Icarus*, 200. [6] Burr et al. (2010) *JGR-Planets*, 115. [7] Lefort et al. (2012) *JGR-Planets*, 117. [8] Kerber and Head (2010) *Icarus*, 206. [9] Kite et al. (2015) *Icarus*, 253. [10] Jacobsen & Burr (2017) *Geosphere*, 13. [11] Burr et al. (2016) *LPS XLVII*, #1392. [12] Jacobsen & Burr (2016) *GRL*, 43. [13] Jacobsen & Burr (2018) *Icarus*, 302. [14] Peel & Burr (2018) *LPS XLIX*, #1006. [15] Lefort et al. (2015) *Geomorph.*, 240. [16] Borden & Burr (2018) *LPS XLIX*, #1003. [17] Boyd & Burr (2018) *LPS XLIX*, #2734. [18] Jacobsen & Burr (2018) *LPS XLIX*, #2057 [\[poster\]](#). [19] Dickson et al. (2018) *LPS XLIX*, #2480.

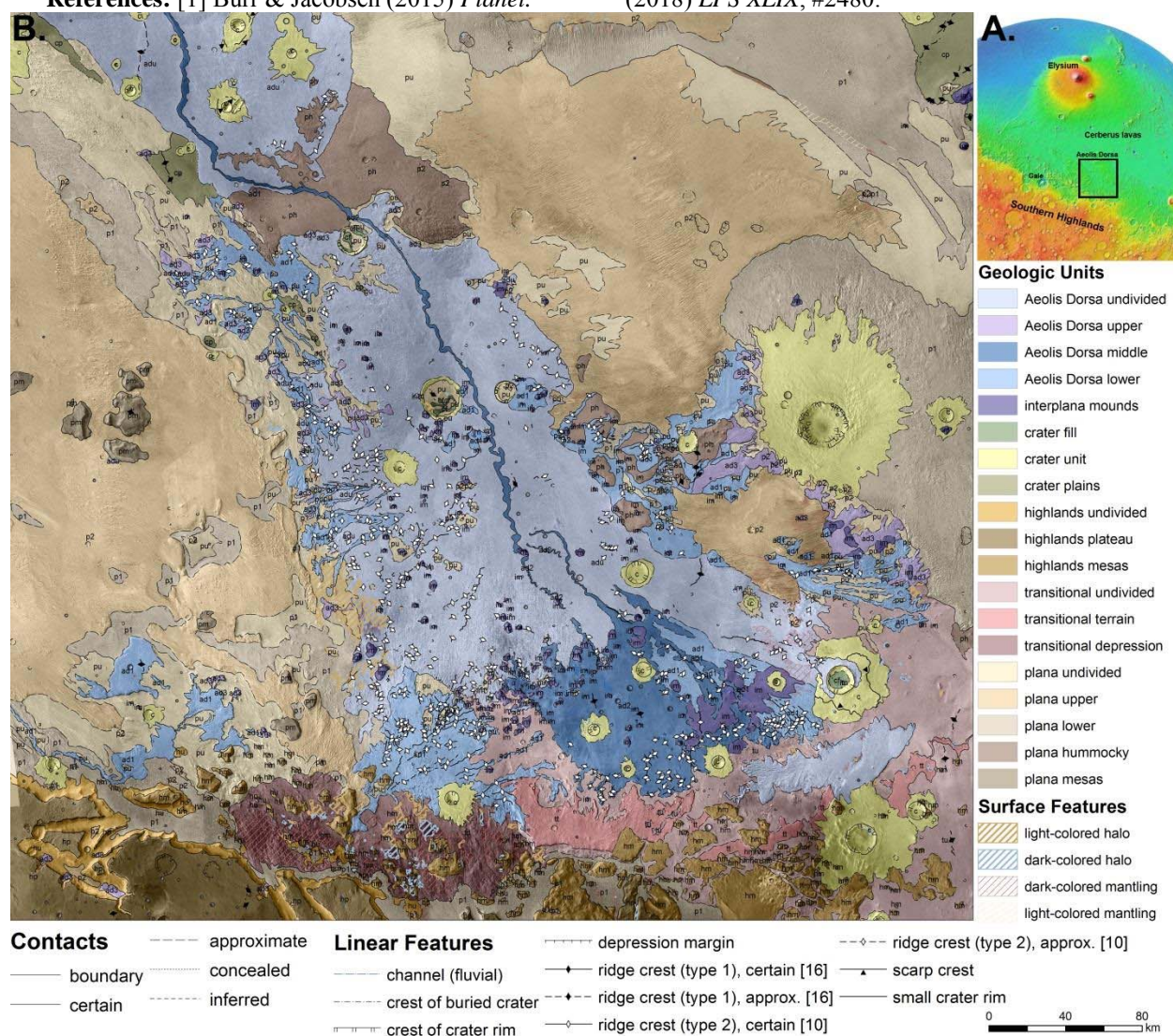


Figure 1: (A) MOLA gridded topography shows the location of the AD map region (black box), between the southern highlands and the Cerberus lavas. (B) Draft of 1:500k map of the AD region [18] overlain on a blended mosaic of CTX images [19].

COMPLETING THE GEOLOGIC MAPPING OF ATHABASCA VALLES, MARS. L. P. Keszthelyi and A. E. Huff, USGS Astrogeology Science Center, 2255 N. Gemini Dr., Flagstaff, AZ. 86001 (laz@usgs.gov).

Introduction: The geologic mapping of the Athabasca Valles region of Mars (MTM quads 05202, 05207, 10202, 10207) was largely completed in 2009. This mapping work pushed the early usage of ArcGIS templates and CTX data, requiring significant unplanned effort (and cost) leaving inadequate resources to produce the four proposed 1:500,000 scale USGS Scientific Investigation Maps (SIM). Instead, the most important scientific insights from the mapping were incorporated into Jaeger et al. [1] and several LPSC abstracts [2-4]. However, NASA's push to resolve "delinquent" maps has provided the opportunity to return to this map. A decade of technological advancements in GIS usage [5] and increased understanding of mapping with HiRISE [6] and CTX data enable this mapping to be completed with only modest effort. The map will be published as a SIM with a single sheet at 1:1M scale.

Mapping Methodology: The scientific focus of this mapping effort is on the latest Amazonian volcanism in Athabasca Valles that borders the southern flank of Elysium Mons. The THEMIS IR basemap used in 2005-2009 had significant location errors when compared to MOLA that are corrected in the new THEMIS IR dataset controlled to MOLA. Consequently, the original linework will need to be cross-referenced with the new base for location accuracy. Mapping on the THEMIS IR basemap was augmented by supplemental data sets, especially MOLA, CTX, and HiRISE. Many of the key lava flow contacts are not resolved in the THEMIS data and are ambiguous even at CTX resolution. Therefore, we used HiRISE data to determine the nature of flow contacts and CTX data to follow them. The bulk of the original mapping linework was done at a 1:50,000 scale on CTX data. However, to produce the 1:1,000,000-scale map we are updating that linework using a more appropriate digital mapping scale of 1:250,000. When a controlled CTX mosaic of the region becomes available, the mapping could be revised at about an order of magnitude higher spatial resolution (1:100,000). However, such detailed mapping is justifiable only for select portions of the map area and is outside the scope of the current effort.

Remaining Work: The nine geologic units we identified and mapped are defined, described, and interpreted below. The stratigraphic correlation of these units is straightforward but new crater counts to place absolute age constraints have not been done as part of this mapping project. Instead, crater statistics from a number of publications [e.g., 7-9] are available. Map symbols adhere to USGS standards.

Map Units. The map units are listed in chronologic order. Minor surficial cover in the form of a patchy dust mantle, areas of sand accumulation, and local talus scarps were mapped at 1:50,000 scale but are not expected to be retained in the 1:1,000,000 scale map. Similarly, we treat unnamed impact craters as structures that modify the target geologic units instead of mapping them as a lithochronostratigraphic unit.

Aav: Amazonian Athabasca Valles Basalt. Turbulently emplaced flood lava detailed in Jaeger et al. [1]. This is the youngest major unit in the map area.

Ath_{a-d}: Lavas from four Amazonian unnamed Tholi. These are designated "A" through "D" with central vent areas and radial flows. The relative ages of the tholi are difficult to determine because their lavas generally do not overlap each other.

Aff₁₋₄: Fissure fed sheet flows. Most fissure vents are oriented parallel to the Cerberus Fossae but some follow wrinkle ridges approximately perpendicular to the Cerberus Fossae. In some cases discrete point sources, i.e., breached lava ponds, have formed along the fissures. While some superposition relations can be made between the fissure-fed flows and those of the different tholi, they are insufficient to construct a complete stratigraphic sequence.

Asf₁₋₄: Sheet lavas with no identifiable source. The vents are buried under lavas from the tholi or fissures. These flows are marginally older than the flows that have visible vents but superposition relations are too sparse to determine a unique stratigraphic order.

AHmf: Amazonian-Hesperian Medusae Fossae Formation. Equivalent to Aam in Tanaka et al. [11] and AHtu and Htu in Tanaka et al. [10]. Subunits with different styles of aeolian erosion are not mapped out.

AHpc: Persbo Crater. As the only named crater in the map area, it seemed appropriate to map its deposits separately.

AHer: Elysium Rise lavas. Equivalent to Tanaka et al. [10] AHEe and Tanaka et al. [11] AHv. This unit is composed of a large number of different lava flows with no good basis by which they can be separated by age or source.

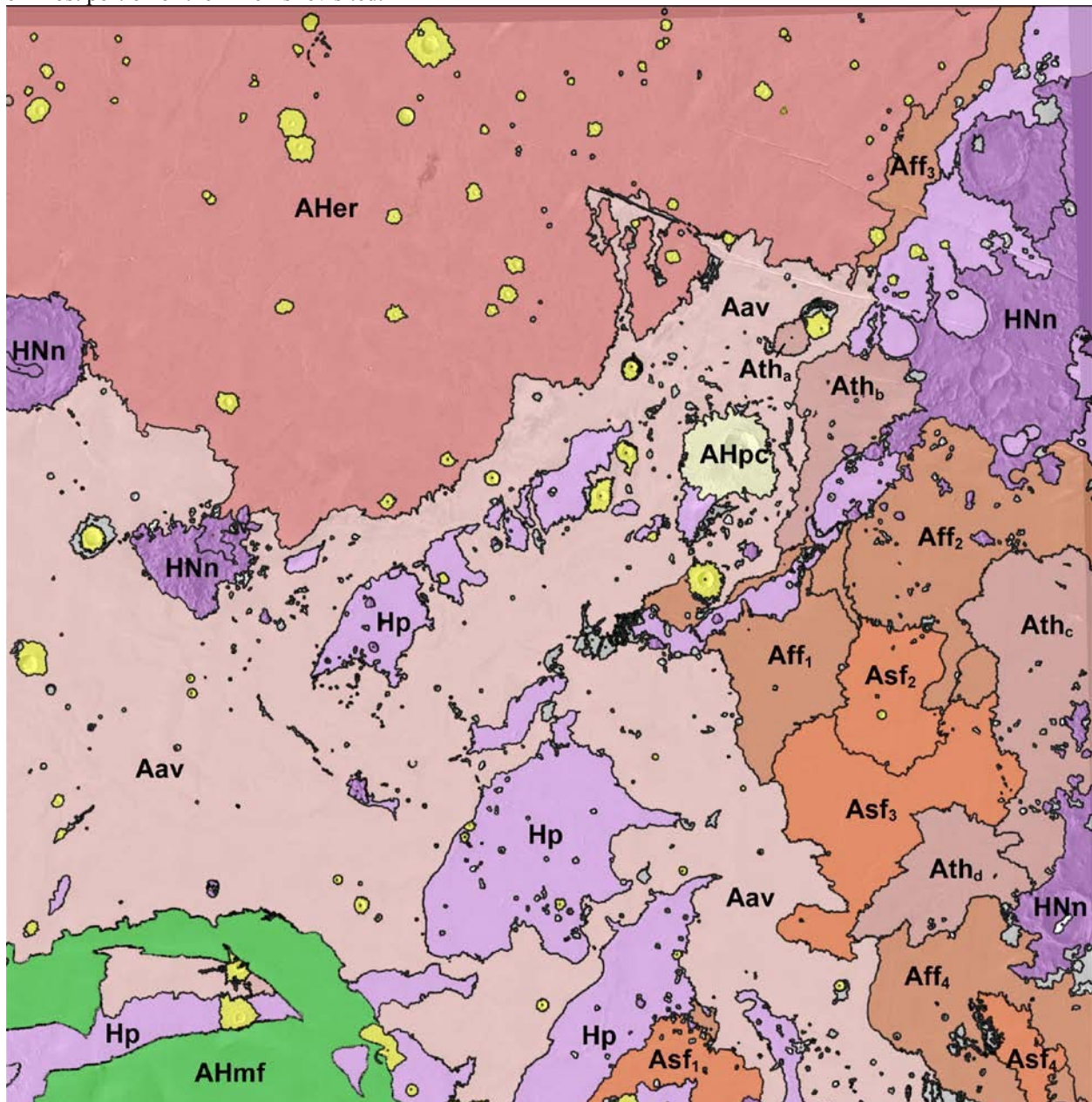
AHp: Amazonian-Hesperian plains. Smooth plains with occasional wrinkle ridges oriented approximately perpendicular to the Cerberus Fossae. These were largely mapped as the Utopia Planitia 2 Unit by Tanaka et al. [5] but are not resolved in the global map [6]. The nature of this unit is uncertain but it is likely to consist largely of colluvium from the erosion of highlands materials.

HNn: Hesperian-Noachian knobs. Equivalent to Nepenthes Mensae Formation of Tanaka et al. [10, 11]. Interpreted as eroded remnants of the ancient heavily cratered southern highlands.

References: [1] Jaeger W. L. et al. (2010) *Icarus*, 205, 230-243. [2] Keszthelyi L. et al. (2017) LPSC 48, Abstract #1755. [3] Keszthelyi L. et al. (2015) LPSC 46, Abstract #2547. [4] Keszthelyi L. et al. (2014) LPSC 45,

Abstract #1683. [5] Hare T. et al. (2015) 2nd Planetary Data Workshop, Abstract #1846. [6] Okubo C. H. (2014) USGS SIM 3309. [7] Burr D. M. et al. (2002) *Icarus*, 159, 53-73. [8] Berman D. C. and Hartmann W. K. (2002) *Icarus*, 159, 1-17. [9] Vaucher J. et al. (2009) *Icarus*, 204, 418-442. [10] Tanaka K. L. et al. (2005) USGS SIM 2888. [11] Tanaka K. L. et al. (2014) USGS SIM 3292.

Figure 1. Current draft of the geologic map of the Athabasca Valles region of Mars. This mapping suggests that the Athabasca Valles Basalt (Aav) followed the contact between the Elysium Rise Unit (AHer) and the Amazonian-Hesperian Plains (AHp, mislabelled as Hp in this figure). This hypothesis will be revisited as the linework of the southernmost portion of the AHer is revisited.



PREPARING THE FIRST GLOBAL GEOLOGICAL MAP OF MERCURY. Mallory J. Kinczyk¹, Paul K. Byrne¹, Louise M. Prockter², Brett W. Denevi³, Lillian R. Ostrach⁴, and James A. Skinner⁴. ¹Planetary Research Group, North Carolina State University, Raleigh, NC 27695. ²The Lunar and Planetary Institute, Houston, TX 77058. ³The Johns Hopkins University Applied Physics Laboratory, Laurel, MD 20723. ⁴U.S. Geological Survey, Astrogeology Science Center, Flagstaff, AZ 86001.

Introduction: The first reconnaissance of Mercury was carried out by the Mariner 10 spacecraft in the 1970s. Three flybys of the planet yielded images of just under half of the globe that were used as the basis for a U.S. Geological Survey (USGS) series of Mercury quadrangle maps [1]. However, the map authors did not follow a uniform set of mapping conventions or units, resulting in inconsistencies across map boundaries and hampering efforts to compare geologic units across multiple regions of the mapped hemisphere.

The Mercury Surface, Space Environment, Geochemistry, and Ranging (MESSENGER) spacecraft orbited Mercury from 2011 to 2015 and imaged the planet in its entirety. A global monochrome image mosaic was released to the Planetary Data System (PDS) in May 2016 at largely uniform viewing geometry and a resolution of ~250 m/pixel [2], providing a comprehensive dataset for geological mapping. This vastly improved data product forms the basis for the first global geological map of Mercury (Fig. 1) [3]. The geological map will facilitate the comparison of units distributed discontinuously across Mercury's surface, thereby enabling a global understanding of the planet's stratigraphy, and providing a guiding basis for future mappers.

Map Status: The map has been prepared for publication at 1:15M scale and will be submitted to a peer-reviewed journal for publication. However, the standards for maps published following USGS guidelines afford detailed community feedback and result in a product that will provide a robust basis for future mappers and missions. The project team is currently in year one of funding through the PDART program to publish the map as a USGS Scientific Investigations Map (SIM) series product.

Geomorphological units for the current map are being delineated on the basis of texture, color, and topographical relief. These units include impact craters, intercrater plains [4], smooth plains [5], and ejecta facies of several large impact basins [6–8], as well as linear/point features such as tectonic landforms [9], hollows [10], and pyroclastic vents [11]. Efforts going forward for the SIM will be focused on improving the state of mapped unit boundaries based on final data products that are publicly available in the final MESSENGER PDS data release [2]. These data will also be used to enhance the map with additional delineated units as warranted.

Mercury's Intercrater Plains: At present, the intercrater plains unit is the most extensive mapped unit on Mercury's surface. It comprises plains materials that lie between large craters and basins and that contain a high spatial density of small superposed craters 5–15 km in diameter [4]. The origin of intercrater plains has been disputed, with proposed mechanisms including effusive volcanism and impact melt pools originating from ancient large impact events [12,13]. Assessing spatial color variation within the intercrater plains could further our understanding of the spatial and temporal differences within this large region on Mercury's surface. Previously, artifacts from temporal variation in responsiveness of the MESSENGER Mercury Dual Imaging System (MDIS) Wide-Angle Camera were as large as or larger than Mercury's true color variations, preventing reliable comparisons of regional color properties. However, recalibrated data now accurately resolve regional color variations within the intercrater plains [13].

Denevi et al. [13] identified an isolated area of intercrater plains with different color properties than the surrounding regions, centered at ~10° N, 270° E. Throughout this region, the intercrater plains have moderate reflectance, and most impact craters with distinct ejecta deposits here expose high-reflectance red material (HRM), defined by a steeper spectral slope and elevated reflectance relative to Mercury's mean. HRM is spectrally equivalent to smooth plains deposits [14], and examples of such material exposed by impact craters [15] were thought to represent older generations of buried volcanic plains. The margins of this area mark a transition to more frequent exposures of low-reflectance material (LRM) within craters and lower overall surface reflectance. This is one of several regions of observed color variations within the intercrater plains.

As part of our work to prepare the Mercury global SIM, we will seek to characterize regional changes in color, topographic, and compositional differences, as well as variations in crater degradation and crater size-frequency distributions, to identify and distinguish subunits within the intercrater plains. The presently available enhanced color mosaic shows evidence that the intercrater plains are not a morphologically or temporally homogeneous unit. Therefore, identifying, resolving, and including these subunits in the Mercury global SIM will provide information critical to future studies of the planet's stratigraphy and early geological history.

Age Estimates for Major Surface Units: Relative and absolute model ages will be determined by evaluating stratigraphic relationships and crater areal densities and size-frequency distributions (SFDs) for units delineated during this work; we will also reevaluate published crater SFDs for previously delineated units. Impact craters ≥ 8 km in diameter will be measured for representative regions of each major mapped surface unit, including possible intercrater plains units, major impact basin-related units (such as the Caloris and Rembrandt units), and select smooth plains units.

By deriving their crater SFDs, we will place each unit into the current chronostratigraphic system for Mercury (i.e., Pre-Tolstojan, Tolstojan, Calorian, Mansurian, and Kuiperian [16]). Representative sections of each unit will be selected on the basis of a spatial randomness analysis [17,18]. Absolute model ages for mapped units will be derived with two modern chronologies for Mercury [19–21].

These tasks will improve the state of the current geological map and will lead to a product that will be consistent in scientific utility with other USGS SIM products.

References [1] Schaber, G. and McCauley, J.F. (1980) USGS Map I-1199; DeHon, R.A. et al. (1981) USGS Map I-1233; Guest, J.E. and Greeley, R. (1983) USGS Map I-1408; McGill, G.E. and King, E.A. (1983) USGS Map I-1409; Grolier, M.J. and Boyce, J.M. (1984) USGS Map I-1660; King, J.S. and Scott, D.H. (1990) USGS Map I-2048; Trask, N.J. and Dzurisin, D. (1984) USGS Map I-1658; Spudis, P.D., and J.G. Prosser (1984), USGS Map I-1659; Strom, R.G. et al. (1990) USGS Map I-2015. [2] Denevi, B.W. et al. (2018) *Space Sci. Rev.*, 214, 1–52 [3] Prockter, L.M. et al. (2016) *LPS*, 27, #1245. [4] Whitten, J.L. et al. (2014) *Icarus*, 241, 97–113. [5] Denevi, B.W. et al. (2013) *J. Geophys. Res. Planet.*, 118, 891–907. [6] Hynek, B.M. et al. (2016) *LPS* 47, #2312 [7] Buczkowski, D.L. et al. (2015) *LPS* 46, #2287. [8] Prockter, L.M. et al. (2009) *LPS* 40, #1758. [9] Byrne, P.K. et al. (2014) *Nature Geosci.*, 7, 301–307. [10] Blewett, D.T. et al. (2013) *Science*, 333, 1856–1859. [11] Thomas, R.J. et al. (2014) *J. Geophys. Res. Planets*, 119, 2239–2254. [12] Wilhelms D. E. (1976) *Icarus*, 28, 551–558. [13] Denevi, B.W. et al. (2016) *LPS* 47, #1624. [14] Head, J.W. et al. (2011) *Science*, 333, 1853–1856. [15] Ernst, C.M. et al. (2010) *Icarus*, 209, 210–223. [16] Spudis, P.D. and Guest, J.E. (1988) in *Mercury*, U. Ariz Press, 118–164. [17] Michael, G.G. et al. (2012) *Icarus*, 218, 169–177. [18] Flatz, T.G. et al. (2013) *Icarus*, 225, 806–827. [19] Marchi, S.A., et al. (2009) *Astron. J.*, 137, 4936–4948. [20] Marchi, S.A., et al. (2013) *Nature*, 499, 59–61. [21] Le Feuvre, M. & Wieczorek, M.A. (2011) *Icarus*, 214, 1–20.

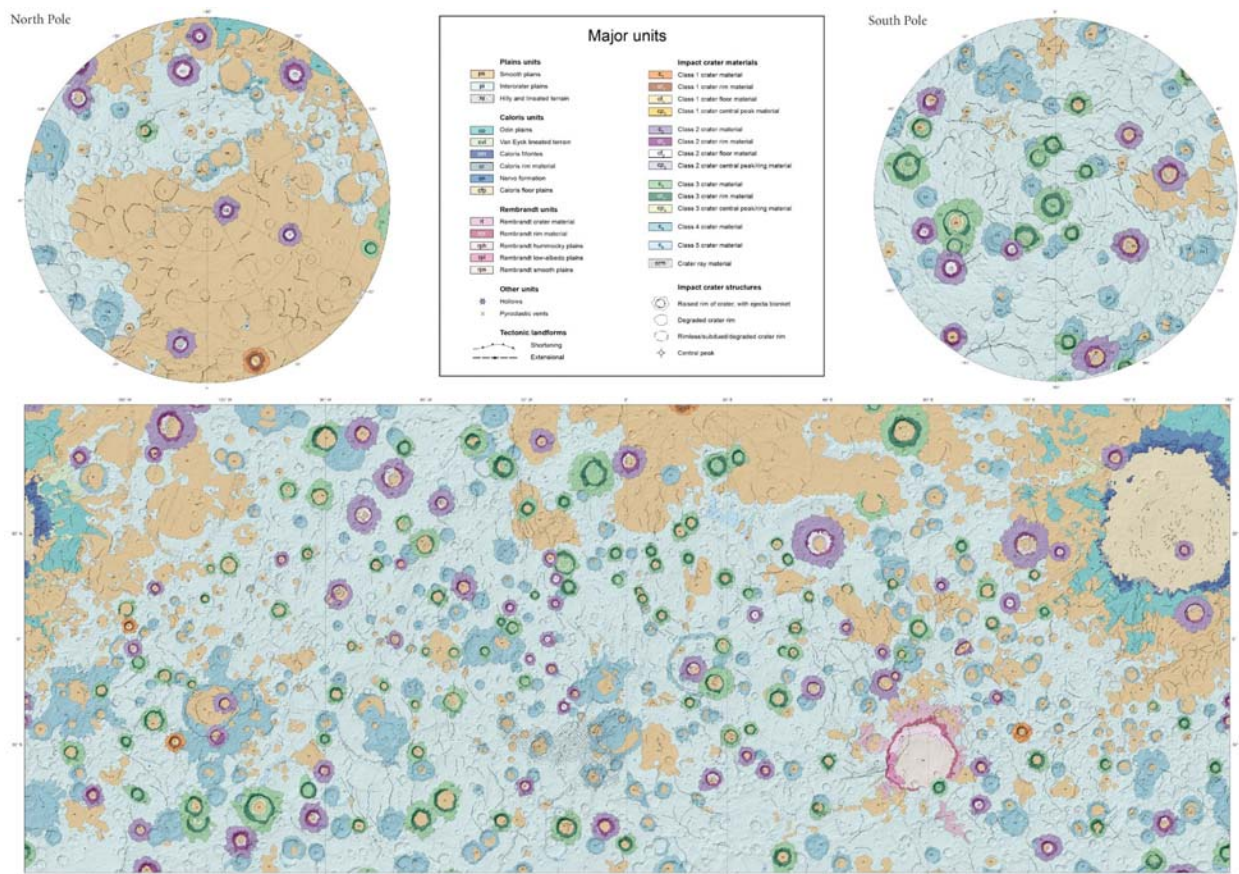


Figure 1. Draft version of the global geological map of Mercury at 1:15M scale, showing major plains units and classified craters ≥ 90 km in diameter.

Lunar tectonic triad joining both hemispheres and its terrestrial analogue; Kochemasov G.G. IGEM of the Russian Academy of Sciences, 35 Staromonetny, 119017 Moscow, Russian Federation, kochem.36@mail.ru

“Orbits make structures” – a main point of the new wave planetology based on one important property of the keplerian elliptical planetary orbits. The ellipticity implies periodical changes of accelerations and, thus, orbital forces structuring cosmic bodies (Fig. 1). Earth and the Moon sharing one circumsolar orbit have similar main structural features [1-3]. Among them are terrestrial Oceans and lunar Basins. Most obvious are two tectonic triads: Pacific Ocean – Malay Archipelago – Indian Ocean on Earth and Procellarum Basin – Mare Orientale – SPA Basin on Moon. Planetary depressions of both bodies are covered with basalts, but basaltic effusions are drastically different in age: the AR on Moon and Mz-Cz on Earth. (Fig. 2). These ages well correlate with the bodies masses. More massive and inert Earth has heated and melted mantle much later (The Newton's law of inertia). Energy of movement transfers to the heat energy.

The both cosmic bodies, as well as other bodies, are tectonically dichotomous. Their subsided hemispheres, for keeping angular momentum of hemispheres equal, are filled with dense basaltic material. But times of the fillings are significantly different. The Earth-Moon system expands with time that it increases its angular momentum. A natural response to it is in slowing down rotation of both bodies diminishing their angular momentum (action - opposite action). Diminishing momenta are compensated by melting and uplifting to surfaces dense basaltic material [3]. But on the Moon it happened much earlier (4.5-3 billion years ago) because of diminished inertia of the small mass satellite. At much larger and massive than Moon Earth – 81 times – it happened much later. (3-4.5 billions) : $81 = 37-55$ million years. According to this calculation, a “peak” of the basaltic reaction of Earth, filling in oceanic depressions by basalts is in the boundary of Mesozoic and Cenozoic.

References:

- [1] Kochemasov G.G. Earth and Moon: similar structures – common origin // NCGT Journal, 2014, v. 2, # 2, 28-38.
 [2] Kochemasov G.G. A lunar “mould” of the Earth's tectonics: four terrestrial Oceans and four lunar Basins are derivative of one wave tectonic process // NCGT Journal, v. 3, # 1, 2015, 29-33.
 [3] Kochemasov G.G. The Moon and Phobos: specific responses of two satellites moving off and nearer their respective planets // DPS 48/EPSC 11, Pasadena, Oct. 16-21, 2016, Bulletin of the American Astronomical Society, 2016, vol. 48, # 7, p. 175, Abstract 318.08, Session 318: Formation and Evolution of Planets and Satellites Posters.

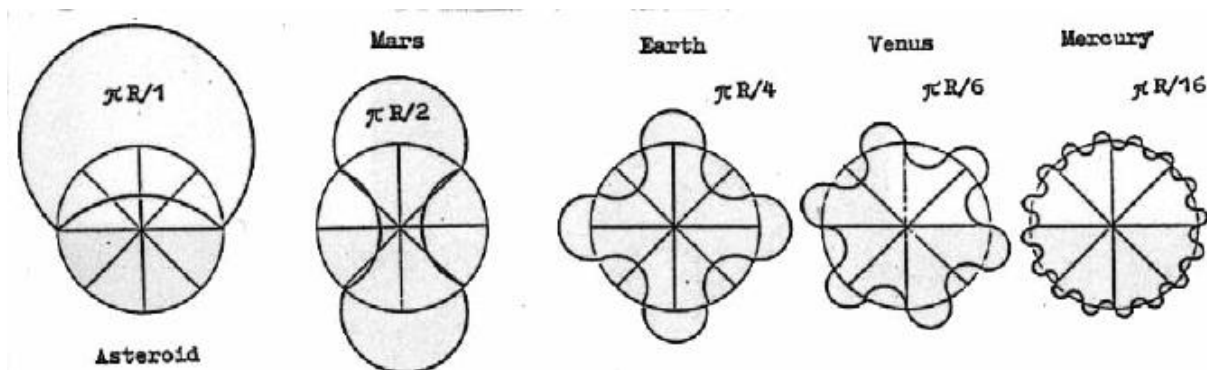


Fig. 1. Schematic demonstration of relation between planets' orbital frequencies and their granular tectonic structures

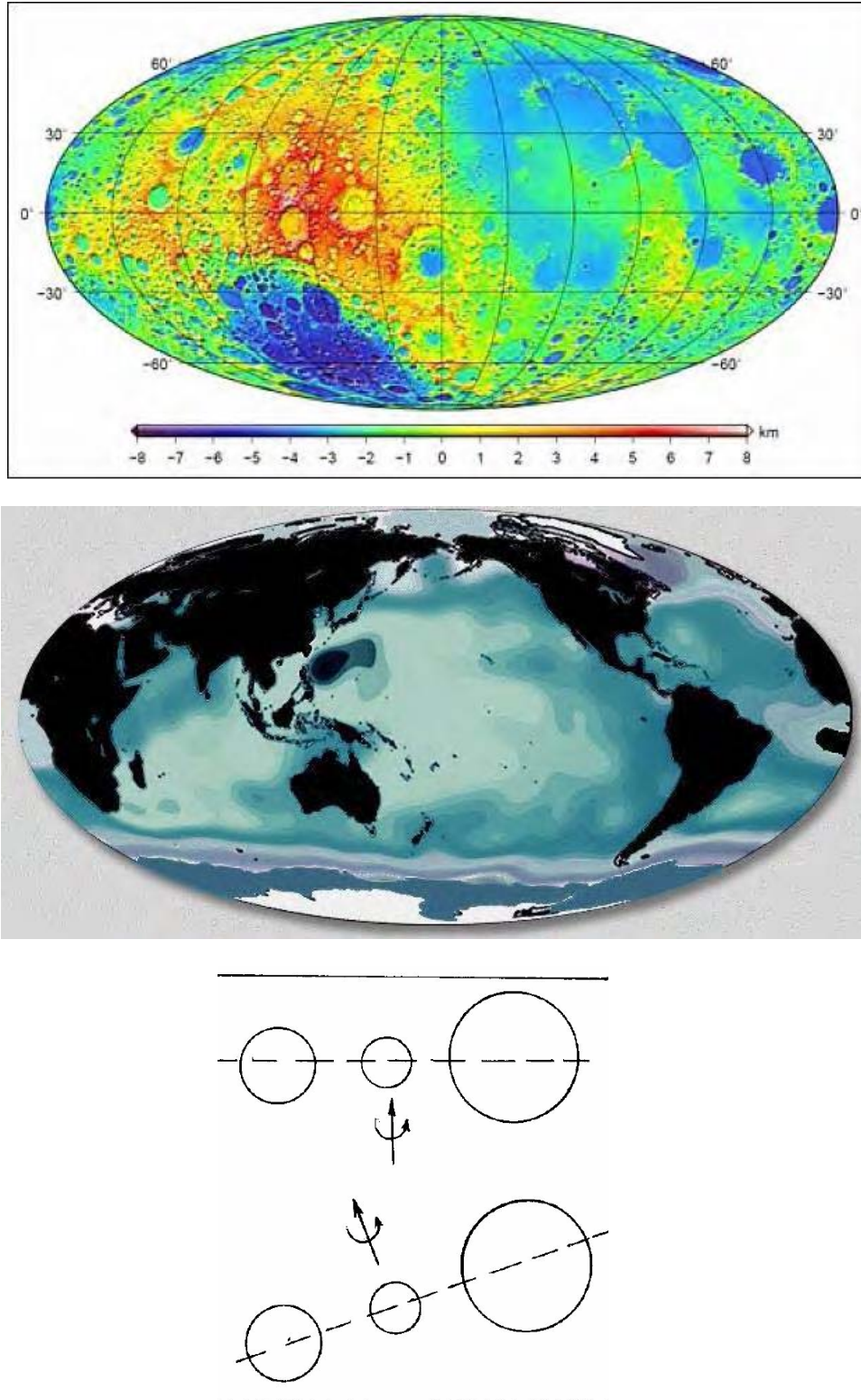


Fig. 2. Tectonic triads. Comparison of Earth's geography and Moon's hypsometry. On the right: Schematic sizes and relative dispositions of terrestrial (above) and lunar wave born tectonic features. Pacific Ocean and Procellarum Ocean on the right - $2\pi R$ structures. Indian Ocean and SPA Basin on the left - πR structures. Malay Archipelago and Mare Orientale at the center - $\pi R/2$ structures. Equators (axis of rotation) positions at present (Earth) and in ancient Moon.

GEOLOGIC MAPPING OF IMPACT CRATERS AND THE MAHUEA THOLUS CONSTRUCT: A YEAR THREE PROGRESS REPORT FOR THE MAHUEA THOLUS (V-49) QUADRANGLE, VENUS. N.P.

Lang¹, M. Covley¹, J. Beltran¹, K. Rogers¹, and B.J. Thomson²; ¹Department of Geology, Mercyhurst University, Erie, PA 16546 (nlang@mercyhurst.edu), ²Department of Earth and Planetary Sciences, University of Tennessee – Knoxville, Knoxville, TN 37996 (bthomso1@utk.edu).

Introduction: The Mahuea Tholus quadrangle (V-49) extends from 25° to 50° S to 150° to 180° E and encompasses $>7 \times 10^6$ km² of the Venusian surface. Moving clockwise from due north, the Mahuea Tholus quadrangle is bounded by the Diana Chasma, Thetis Regio, Artemis Chasma, Henie, Barrymore, Isabella, and Stanton quadrangles; together with Stanton, Mahuea Tholus is one of two remaining quadrangles to be geologically mapped in this part of Venus. Here we report on our continued mapping of this quadrangle. Specifically, over the past year we have focused on mapping and cataloging impact craters located within the quadrangle as well as larger-scale mapping of the Mahuea Tholus construct; those efforts are described in this contribution.

Impact Craters [1]: V-49 contains 13 confirmed impact craters (Table 1). Twelve of the craters occur entirely within V-49 and one crater, Austen, straddles the boundary between V-49 and V-37 to the north. In addition to impact structures, at least four radar dark circular splotches that do not host an impact crater occur within V-49. We interpret these splotches as the result of air burst events that did not create a crater structure; two of these splotches (splotches A and B) are spatially associated with Qarlygha and Kaikilani impact craters and may be tied to their occurrence. Impact craters range from 12-100 km in diameter with an average diameter of ~20 km. All craters are associated with ejecta blankets and at least three craters – Howe, Onissya, and Valadon – also host fluidized ejecta materials. Onissya appears to represent a possible double crater. Located east of Howe, and potentially associated with its formation, is a radar-bright, ‘streaky’ patch that could be either ejecta or additional fluidized material. Seven craters exhibit radar-dark floors. Five craters exhibit a central peak and the occurrence of a central peak is indeterminate for five craters. Ten craters appear to have occurred after tectonism within V-49 and the remaining three craters have been deformed by wrinkle ridges and fractures meaning they predate at least some tectonic activity in V-49.

Mahuea Tholus Construct [2]: The Mahuea Tholus construct (37.5° S, 165° E) is a solitary, intermediate-sized volcano located in the center of V-49. The

edifice is ~100 km in diameter (with all flow materials, Mahuea is ~300 km in diameter), ~0.5 km in height with a ~4 km diameter flattish top, and an erupted volume of ~10³ km³. Mahuea is located within the center of a topographic basin in Zhibek Planitia ~1400 km SE of the main axis of Diana-Dali Chasma-related rifting. The volcano resides at the eastern end of Annapurna Corona-related fractures (Naguchitsa Fossae) and overlies Annapurna-sourced flow material – material previously interpreted as possible pyroclastic deposits sourced from Mahuea Tholus [3]; Annapurna-sourced flows were then subsequently deformed by NE-trending wrinkle ridges, which was then followed by formation of Mahuea Tholus. At least four eruptive events are recorded at Mahuea Tholus and each event is marked by a thick (~100 m), lobate, radar bright flow that records numerous pressure ridges and channel structures; the earliest recorded flow materials are the most extensive with the youngest flows being more localized. Based on mapped relations, we interpret that fractures within Naguchitsa Fossae facilitated eruption of Mahuea Tholus flow material and, therefore, magmatism at this volcano is likely related to magmatism at Diana-Dali Chasma as a whole. Perhaps the location of this volcano off the main axis of rifting caused stalling of magma ascent, which in turn could have facilitated either a slower effusion rate and/or evolution of magma chemistry resulting in the eruption of thick lava flows. Such a prediction may be testable through continued regional mapping of intermediate-sized Venusian volcanoes, in situ spectral analyses by Venusian landers, and further constraints on thickness variations of the Venusian crust.

Future Directions: We are now in the final stages of mapping V-49. Our current efforts are emphasizing cleaning up line work, refining map unit descriptions, creation of a sequence of map units, and writing the map text.

References: [1] Beltran, J., et al. (2017), *GSA Abs w/ Programs*; Vol. 49, No. 6 doi: 10.1130/abs/2017AM-306199. [2] Covley, M.T., et al. (2017), *GSA Abs w/ Programs*, Vol. 49, No. 6 doi: 10.1130/abs/2017AM-306141 [3] Moore, H.J., et al. (1992), *JGR*, 97, E8, 13,479-13,493.

Table 1. Impact features of V-49

Crater name	Latitude (deg N.)	Longitude (deg E.)	Diameter (km)	Halo	Central Peak	Deformation
Austen	-25	168.4	45.1	N	Y	Y
Ayana	-29.2	175.5	13.8	Y	?	N
Howe	-45.7	174.8	38.6	Y	Y	N
Kaikilani	-32.8	163.2	19.9	Y	Y	N
Onissya	-25.6	150.2	8.2	Y	N	N
Pavlinka	-25.5	158.7	7.5	N	N	Y
Philomena	-40.7	151.9	14.8	Y	?	N
Qarlygha	-33	162.9	9.3	Y	N	N
Radhika	-30.3	166.4	7.9	Y	N	N
Whitney	-30.2	151.3	42.5	N	Y	Y
Ulpu	-35.7	179	7	Y	?	N
Valadon	-49	167.7	25.2	Y	Y	N
Yasuko	-26.1	169	10.6	Y	?	N
Zemfira	-46.2	157.7	11.4	Y	?	N
Spotch A	-33.3	161.9	38.1			
Spotch B	-33.4	162.8	19.5			
Spotch C	-36.4	162.5	61.9			
Spotch D	-41.7	158.2	52.9			

THE EUROPA GLOBAL GEOLOGIC MAP. E. J. Leonard^{1,2}, D. A. Patthoff³, D. A. Senske², and G.C Collins⁴
¹University of California, Los Angeles, (erinleonard@ucla.edu), ²Jet Propulsion Laboratory, California Institute of Technology (David.a.senske@jpl.nasa.gov), ³Planetary Science Institute (apatthoff@psi.edu), ⁴Wheaton College (gcollins@wheatoncollege.edu).

Introduction: First discovered by Galileo Galilei over 400 years ago and imaged in detail by Voyager 2 in 1979, Jupiter's icy moon Europa has been a source of intrigue. A range of science investigations suggest it contains the key ingredients for habitability [e.g., 1, 2]. Investigations of Europa's geology show that its surface is geologically complex and, based on the dearth of impact craters, interpreted to be as young as ~60 Ma [3-9]. Establishing the global context of the distribution and timing of European geologic units forms a basis to understand regional and local scale processes, serves as a tool for the planning of future missions, and most of all is essential to gaining insight into the potential habitability of this icy world.

Procedure: Our geologic map is produced following planetary mapping standards [e.g., 10-14] in order to separate observations of characteristics and interpretations thereby ensuring that the objective descriptions of each unit and feature are valid for any future Europa dataset.

Units: The units defined in this map are grouped by morphologic type and named with respect to that type. This is a practice often used for mapping on Europa [e.g., 7-9, 15]. We also base all of the unit names and colors on previous maps of Europa as to preserve heritage and to make this map clearly comparable to other published maps of Europa [7, 9, 16].

Linear Features: Features that are less than ~20 km wide are too narrow to be resolvable as units on the 1:15M map, but can still be prominent because of their length (> 50 km) or albedo contrast. Instead, these structures are mapped with a line which marks the length, location, and trend of the feature. To simplify the map, not all lineaments on Europa's surface are identified. We identify those that are prominent (e.g. longer and wider than most), useful for constraining stratigraphy, or represent the density and distribution of the other lineaments of the area.

Initial Results: We have generated a global map at a scale of 1:15M of Europa (Figure 1) and established seven aerially extensive, geologic map units which we can divide into four categories: (1) crater material (c) and its subunits, continuous crater ejecta (ce) and discontinuous crater ejecta (dce)—materials associated with impact craters including the primary impact crater and its local deposits and farther ranging ejecta material; (2) Various morphological types of chaos materials identified as high albedo chaos (chh),

mottled chaos (chm), low albedo chaos (chl) and knobby chaos (chk)—disrupted terrains whose textures vary and albedos range from high to low with various degrees of mottling; (3) general band forming material (b) and high albedo bands (bha)—linear to curvilinear zones with a distinct, abrupt albedo change from the surrounding region; and (4) ridged plains (pr)—the most abundant unit that is distributed across all latitudes and is characterized by subparallel to cross-cutting ridges and troughs visible at intermediate to high resolution (<100 m/pixel).

In addition to the geologic units, our map also includes a number of structural features including: depression margins (dm), troughs (t), multi-ring structures (mrs), microchaos (mch)—areas of surface disruption that are too small (10-75 km in diameter) to be mapped as a unit at the 1:15,000,000 scale, but whose presence is ubiquitous and significant enough to be identified on the map as a point—cycloids (cy), band linea (bl), ridges (r), and undifferentiated linea (ul).

Relative Ages: Relative ages of geologic units and structures on planetary bodies are determined largely by cross-cutting, or superposition and embayment, relationships. However, determining relative ages of structures or units on Europa is challenging for a variety of reasons including: (1) the overall complexity of the surface, (2) the lack of consistent image resolution at the global scale necessary to determine cross-cutting, and (3) the small number of impact craters. Despite these limitations, we can draw general conclusions about Europa's global surface history.

Chronostratigraphy: We have created a general stratigraphic column of the different units and features identified on Europa (Figure 1) despite the challenges described above. The jagged boundaries on the units and dotted lines on the linear features indicate the complexity and uncertainty of unit relationships.

There appear to be three separate periods in Europa's visible surface history, ~100 Ma [e.g., 17, 18]. The first, or oldest, of these periods is dominated by ridged plains, ridges, and undifferentiated linea indicating that this period was dominated by ridge building processes. We observe this to be the case as there are no units or structures that appear older, or cross-cut, the ridged plains unit.

The second, or middle, period is dominated by Band and High-Albedo Band formation. The Band and High-Albedo Band units always appear younger and

cross-cut the Ridged Plains unit. Cycloids also appear to be formed during this period and can appear similar to ridge or band linea structures and even transform from one to the other along their length, potentially indicating a transition from a ridge-building to a band-forming mechanism (0°, 133° E).

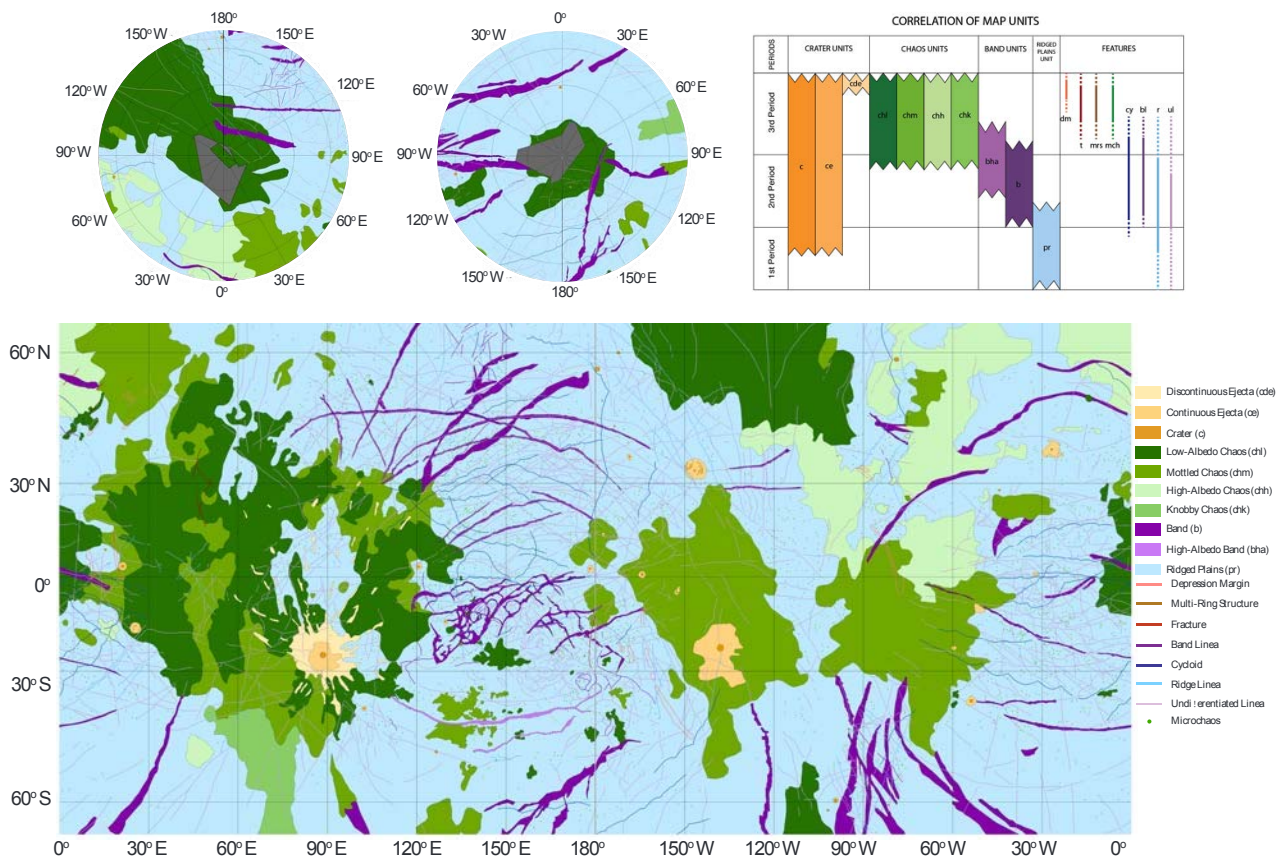
The third, or most recent period, is dominated by chaos terrain formation including microchaos formation. Chaos terrain does not appear to have any cross-cutting units besides craters and their associated deposits, the troughs in the northern leading hemisphere, and potentially depression margins (though this is difficult to determine). Likewise, microchaos is observed breaking up previously formed bands, ridges, cycloids and other features, indicating that as a whole it is younger.

Though three different periods have been identified in Europa's surface history, in agreement with regional mapping by others [e.g., 7], we emphasize that they are still heavily inter-fingered with one another and are not discrete periods. This apparent interfingering could be a result of the complications described previously in this section though we believe that this will hold true even with increased resolution or other age dating techniques.

Initial analysis of the distribution of microchaos suggests that it is not uniformly distributed across Europa, instead, it appears to show an increase in density associated with the bands. We are currently assessing this relation as it implies to disruption of the crust and communication between the subsurface and surface. In this presentation we will discuss the global-scale geologic terrains as well as our preliminary findings regarding the distribution of microchaos.

References: [1] Wackett et al. (2004), A. and E. Microbio., 70, 647-655. [2] Hand et al. (2009), Europa, U of AZ Press. [3] Lucchitta and Soderblum (1982), Satellites of Jupiter. U of AZ Press. [4] Pappalardo et al. (1999), JGR, 104, 24015-55. [5] Bierhaus et al., (2001), Icarus, 153, 264-276. [6] Bierhaus et al. (2009), Europa, U of AZ Press. [7] Figueredo and Greeley (2004), JGR, 105, 22,629-46. [8] Prockter and Schenk (2005), Icarus, 177, 305-326. [9] Doggett, et al. (2009). Europa, U. of AZ Press, 137-159. [10] Wilhelms (1990) Planetary Mapping, Cambridge U. Press, 208-260. [11] Skinner and Tanaka (2003), LPSC XXXIV, Abstract 2100. [12] Tanaka et al., (2005), USGS Map. [13] Wilhelms (1972), Astrogeology, 55. [14] Tanaka et al. (2011), Planetary Geologic Mapping Handbook. [15] Prockter et al. (1999), JGR, 104, 16531-40. [16] Prockter et al. (2002), LPSC XXXIII, Abstract #1732. [17] Zahnle et al. (1998), Icarus, 136, 202-22. [18] Zahnle et al. (2003), Icarus, 163, 263-289.

Figure 1: Global geologic map of Europa, legend (bottom right) and the correlation of map units (top right).



BUILDING A GEOLOGIC MAP OF NEPTUNE'S MOON TRITON. E. S. Martin¹, D. A. Patthoff², M. T. Bland³, T. R. Watters¹, G. C. Collins⁴, T. Becker³, ¹Smithsonian Institution, National Air and Space Museum, Center for Earth and Planetary Studies (martines@si.edu), ²Planetary Science Institute (appatthoff@psi.edu), ³U. S. Geological Survey, ⁴Wheaton College.

Introduction: In 1989, Voyager 2 encountered the Neptune system and returned images of its largest moon (~1350 km radius), Triton, and these images remain the primary data for our understanding of the satellite (Fig. 1). Triton was revealed to be a geologically active moon [1], and its activity has been linked to its dynamical history as a captured Kuiper Belt Object (KBO) [e.g., 2].

Until the New Horizons mission flew by Pluto in 2015, Triton was the only KBO visited by spacecraft; however, Triton's role as our only close-up example of a probable KBO was always dogged by the question of whether its geology was representative of other KBOs, or resulted from its unique history. That question has not yet been rigorously reassessed in the post Pluto-encounter era.

Additionally, Triton bridges a gap between KBOs and icy satellites. As a likely KBO captured into Neptune's orbit [e.g., 2] it contributes to the diverse population of icy satellites, but its origin is unique relative to those of the icy satellites and likely contributes to its young surface and exotic terrains (Fig. 1) [3]. The capture of Triton by Neptune likely resulted in a massive heating event that resulted in resurfacing [4, 5], possibly by cryovolcanism [6, 7]. Crater counts for both Triton [8] and portions of Pluto [9] suggest that both surfaces are exceptionally young, which may indicate that neither Triton nor Pluto retain their original surfaces.

The successful New Horizons flyby through the Pluto system opened the door to another part of the solar system revealing an extraordinary diversity of terrains, renewing interest in the origin, evolution, and diversity of KBOs [9], and by extension, Triton.

To-date, no peer-reviewed, broad-scale, detailed geologic map exists to characterize, classify, and identify geologic surface units and features on Triton. Mapping of Pluto and Charon is in progress [10, 11, 12], but as no comparable geologic map of Triton exists, a direct comparison between these two KBOs cannot be performed at a fundamental level. Furthermore, as Triton serves as a bridge between KBOs and icy satellites, characterization of its terrains is important for advancing comparative planetological studies.

We aim to create an extensive accessible Triton data archive that will recover and restore original data products and provide context for future investigations by creating a geologic map across Triton's Neptune-facing hemisphere.

Previous geologic mapping efforts on Triton include local geologic maps of individual features (Fig. 2a)



Figure 1: Orthographic projection of Triton's Neptune-facing hemisphere. Image No PIA00317

broad-scale terrain maps (Fig. 2b), or cursory maps that lack sufficient documentation (Fig. 2c). The most comprehensive of these maps was initially presented as a sketch map [1] and expanded into Fig. 3 [13]. However, Fig. 3 is not a Scientific Investigations Map (SIM) by the U. S. Geological Survey (USGS), and is not available in a digital format for distribution and use by the community. Detailed descriptions of geologic units are further illustrated with Voyager images of terrains and structures; however, poor printing quality makes it impossible to verify these geologic units. It is necessary for an accessible, digitized, USGS SIM be created to firmly establish the geology of Triton's surface.

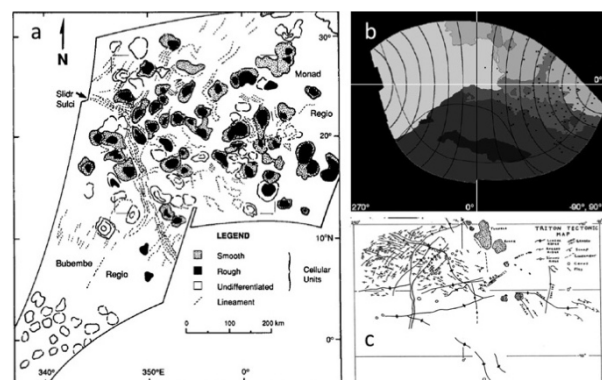


Figure 2: Overview of Triton mapping efforts including a. A local-scale survey of the cantaloupe terrains (Fig. 2 from [3]) b. Crater locations and geologic units (modified from Fig 1 & 5 from [8]) c. Map of Triton's tectonic structures [13].

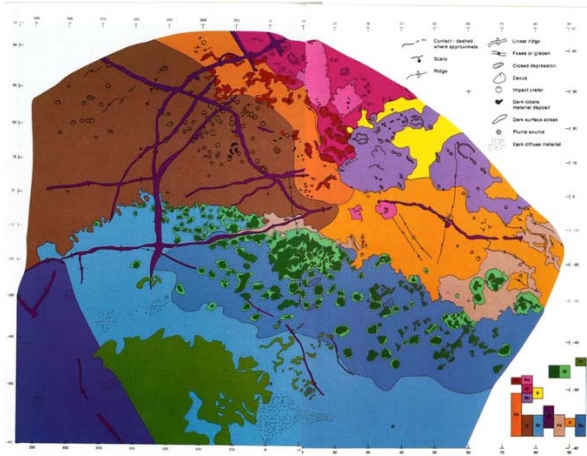


Figure 3: Geologic map of Triton from [13].

Mapping Triton's Geology: Understanding Triton's geologic history is essential to unraveling its origin and evolution. The surface of Triton is estimated to be extraordinarily young [8], not unlike many regions of Pluto [9], which suggests the probability of being heavily modified from their original states. Geological mapping of Triton will allow for identification of geologic units and structures that are recently formed, and those that are ancient, revealing more about Triton's evolution. The production of a geologic map builds a context for understanding the geologic history of a planetary body with a standardized set of criteria that conveys a geologic history in a way that is consistent across planetary bodies. Our mapping of Triton will build upon existing maps of Triton [e.g., 13] by using updated computer-aided digital mapping techniques that enable much finer details to be identified and shared with the community.

We will produce a SIM series geologic map of the Neptune-facing side of Triton at a scale of 1:5,000,000. The printed map product will be produced at 1:5M, however the digital product that will be published by the USGS will be 1:2.5M, higher than any Triton map product to date.

Mapping will occur on the USGS Voyager 2 orthographic color mosaic with a resolution of 600 m/pixel (Fig. 1), however for the purposes of mapping the color will be removed from the gray-scale color mosaic. This mosaic covers approximately 1/3 of Triton's surface from 45° to -60°N latitude and -75° to 90°E longitude.



Figure 4: Triton controlled photomosaic from Voyager 2 with exaggerated color that will be used for mapping.

Our mapping effort will begin by identifying individual feature classes and cataloging characteristics. The first class of features to be mapped and described will be linear features. [13] produced a fracture map of Triton (Fig. 2c) including linear ridges, rugged ridges, sinuous ridges, graben, scarps, and lineaments. The map of these features exists only as a so-called sketch map [13] done at 1:5M. Furthermore, the description of the morphology and classification criteria defining different linear features is not documented.

Geologic mapping is one of the most fundamental practices necessary for understanding the geological history of a planetary body. The resurgence of interest in Triton and KBOs has been motivated in part by the success of the Pluto-system flyby by the New Horizons spacecraft and the approval for New Horizons to flyby a second targeted KBO. Triton is also a unique body because it bridges the gap between icy satellites as an icy KBO captured into Neptune's orbit. This map will provide a framework for future Triton research, future KBO research, and preparation for future missions.

References: [1] Smith B. A. et al. (1989) *Science* 246, 1422-1449. [2] Mckinnon W. B. et al. (1995) *Neptune and Triton*, ed. Cruikshank. P807-877. [3] Schenk P. M. and Jackson P. A. (1993) *Geology*, 21, 299-302. [4] McKinnon W. B. (1984) *Nature* 311, 355-358. [5] Mckinnon W. B. (1992) *EOS* 73, 190. [6] Croft S. K. (1990) *XXI LPSC*, 246-247. [7] Schenk P. M. (1992) *XXIII LPSC*, 1215-1216. [8] Schenk P. M. and Zahnle, K. (2007) *Icarus*, 192, 135-149. [9] Stern, A. S. et al. (2015) *Science* 246, 1422-1449. [10] Moore J. M et al. (2016) *Science* 351, 1284-1293. [11] Robbins, S. J. et al. (2016) *Geologic Mappers Meeting #7026*. [12] White, O. L. (2016) *Geologic Mappers Meeting #7001*. [13] Croft S. K (1995) *Neptune and Triton* ed. Cruikshank, 879-947.

UPDATING THE GLOBAL MAP OF TITAN FLUVIAL FEATURES AND INVESTIGATING DOWNSTREAM RADAR BRIGHTNESS TRENDS. A. D. Maue¹, D. M. Burr¹, J. S. Levy², and E. Nathan², ¹University of Tennessee, Knoxville TN, ²Colgate University, Hamilton, NY; (amaue@vols.utk.edu).

Introduction: Fluvial features are widespread across the surface of Saturn's moon, Titan [1,2]. Global maps of these features have yet to include the most recent Titan flyby data. We identify fluvial morphologies and map their lengths as polylines in all available radar image swaths. As on Earth, the mapped features commonly exhibit branching morphologies and occasionally terminate at lakes [3]. Toward the poles, fluvial features appear radar-dark relative to the surrounding surface, interpreted to reflect the presence of extant liquid hydrocarbons indicated by their smooth surface and emissivity as reported for Titan's liquid methane lakes [3]. These features stand in contrast to those at the mid-to-low-latitudes, where fluvial features are more commonly radar-bright relative to their surroundings—an observation that has been linked to the presence of highly backscattering spheroidal cobbles [4]. To study the processes of fluvial transport and deposition on Titan, we select a subset of the most prominent radar-bright fluvial features to analyze more closely.

In this work, we update the global map of fluvial features to include nearly all image swaths and investigate specific radar-bright fluvial features for possible sedimentological trends.

Titan data: Owing to Titan's dense atmospheric haze, radar wavelengths are used for deriving images of the body's surface. The Cassini RADAR instrument produced Synthetic Aperture Radar (SAR) image swaths, as well as altimetry, scatterometry, and radiometry datasets [5]. We utilize incidence- and noise-corrected SAR images which report pixel values as the unitless radar backscatter, sigma naught (σ^0). Titan SAR images have an optimum spatial resolution of 350 m/pixel, enabling the identification of km-wide features at best. In the Descent Imager/Spectral Radiometer (DISR) images taken at low altitude by the Huygens probe, smaller fluvial features can be seen. These optical images clearly demonstrate the expected fractal quality of natural river networks and thus the prevalence of fluvial activity below SAR resolution [2] that may influence sedimentology. The widespread resolved and sub-resolution fluvial networks, as well as the rounded cobbles seen at the Huygens landing site [6], strongly imply extensive fluvial sedimentary processes across the moon. In addition to global mapping, this work further investigates evidence for fluvial sedimentation in Titan's drainage networks through analysis of σ^0 trends.

Linear mapping: The most recent SAR-based global mapping efforts utilized swaths through Titan flyby T-71, investigating morphologies [1] and relevant fluvial processes [2]. In the former, morphological classifications of 51 networks in SAR and DISR images as commonly rectangular indicated tectonism may be influencing fluvial network structures, although dendritic and parallel networks suggest that such influence is not uniform [1]. An expanded distribution of mapped features has the potential to test these findings and add statistical significance to similar spatial analyses.

Recent updates. The Cassini mission has since reached its conclusion and the final radar images are anticipated to be released in April 2018. With these 14 additional SAR swaths, we will be able to produce a final hydrological map at the end of the Cassini mission.

With fluvial features delineated as polyline networks, morphological attributes can be identified and quantified. One valuable characteristic is the flow direction. For heavily branching networks, the downstream direction is inferred from the direction of tributary confluence (**Fig. 1**). Additional evidence for flow direction comes from inferred downstream depositional sites such as lakes and/or upstream sources such as high-roughness terrain. Finally, slope aspect derived from sparse elevation data [7] can provide more direct evidence for the expected flow direction at present.

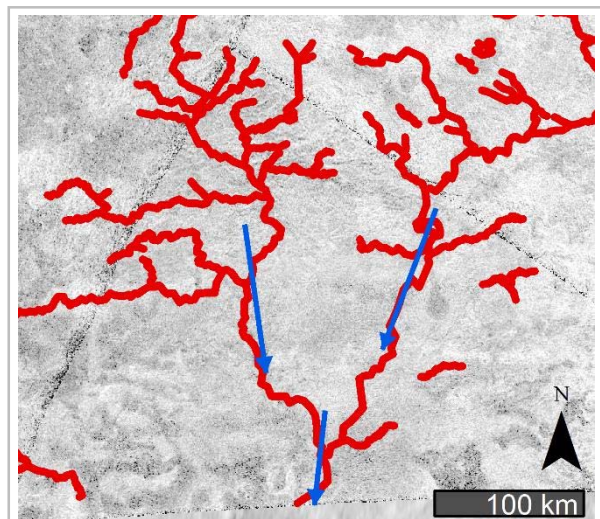


Figure 1. Example of a radar-bright fluvial feature at 140°W, 10°S mapped as polylines (red lines) exhibiting rectangular morphology with inferred flow directions (blue arrows).

Radar brightness trends: Modeling of radar backscatter indicates that radar brightness in some fluvial features southeast of Xanadu correlates to the grain size of transparent cobbles [4]. This effect is greatest for clasts with diameters approximating (or a factor of a few greater than) the wavelength of the reflected microwaves (~ 2 cm). Rounded cobbles (e.g., sediment at the cm-to-dm scale) are expected based on the in-situ surface images of the Huygens landing site [6].

Based on the anticipated link between radar brightness and fluvial cobbles, we isolate select radar-bright fluvial features to examine downstream radar brightness changes that may be indicating grain size trends. Radar-bright fluvial features that are sufficiently wide ($>$ few pixels) and long ($>$ 50 km) are mapped as polygons. Radar-bright pixels are captured in segments moving down the length of the feature (Fig. 2), from which representative values can be calculated.

Conclusions and Future Work: The global map of Titan's fluvial features is being updated using the final radar swaths of the Cassini mission (Fig. 3). The result is a product that can enable the most robust hydrologic analyses of Titan to date and may persist until the arrival of a future spacecraft, possibly decades in the fu-

ture. We will also examine large radar-bright fluvial features for possible radar-brightness trends than can then be put in a global sedimentological context. The measured downstream changes in radar brightness will be related to expected rates of abrasion for icy sediment, as determined with the Titan Tumbler [8,9].

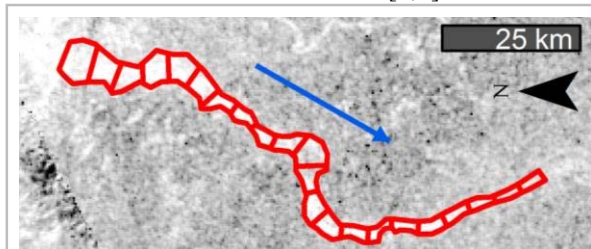
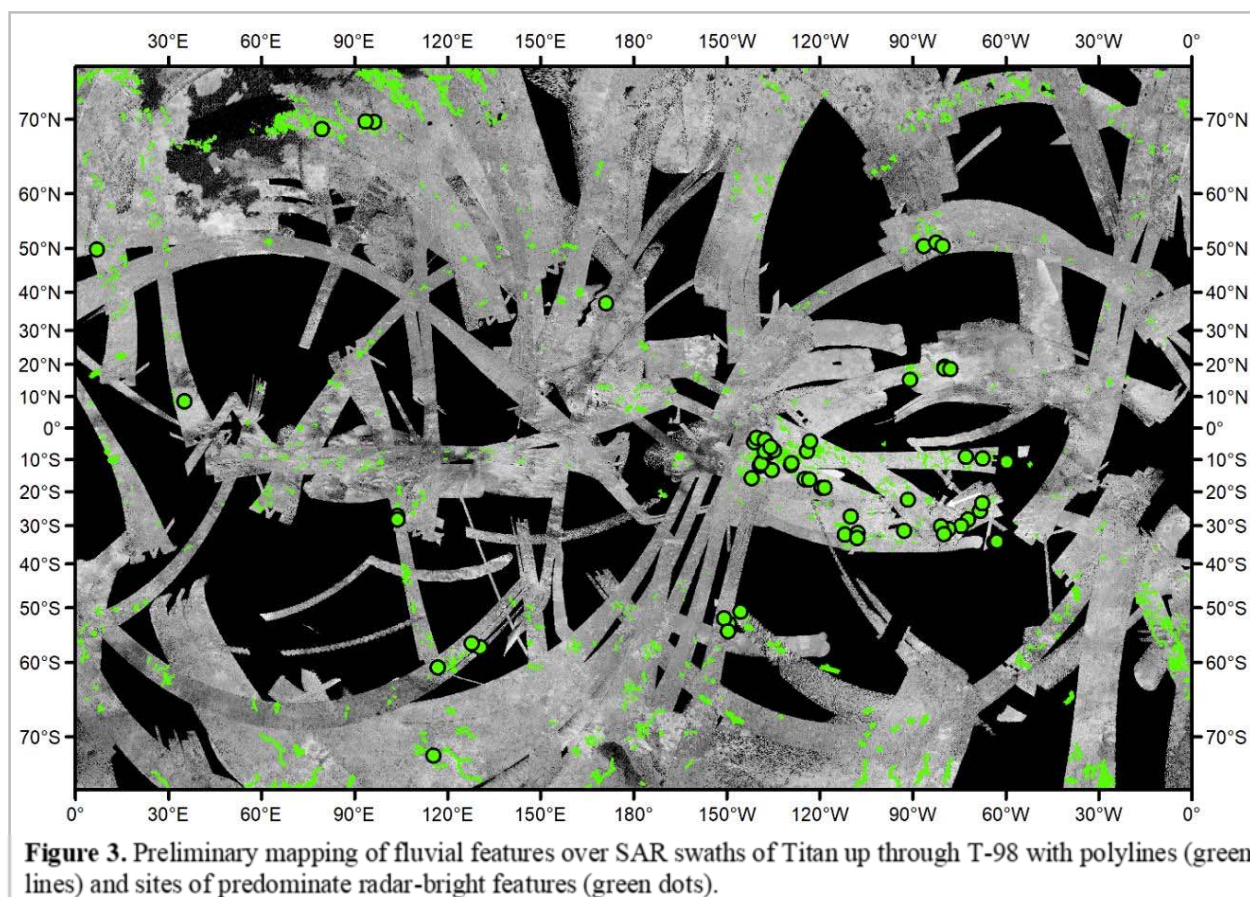


Figure 2. Example a large radar-bright fluvial feature at 119°W , 19°S mapped as polygonal segments (red lines) with inferred flow direction (blue arrow).

References: [1] Burr et al. (2013) *Icarus*, 226. [2] Burr et al. (2013) *GSAB*, 125. [3] Stofan et al. (2007) *Nature*, 445. [4] Le Gall et al. (2010) *Icarus*, 207. [5] Elachi et al. (2004) *Space Sci. Reviews*, 115. [6] Tomasko et al. (2005) *Nature*, 438. [7] Corlies et al. (2017) *GRL*, 44. [8] Levy et al. (2017) *LPSC XLVIII*, Abs. #1105. [9] Maue et al. (2018) *LPSC XLIX*, Abs. #1113.



INVESTIGATIONS OF VOLCANIC AND VOLATILE-DRIVEN PROCESSES NORTHEAST OF HELLAS BASIN, MARS. Scott C. Mest¹, David A. Crown¹, Joseph Michalski², Frank C. Chuang¹, Katherine Price Blount³, and Leslie F. Bleamaster⁴, ¹Planetary Science Institute, 1700 E. Ft. Lowell Rd., Suite 106, Tucson, AZ 85719; ²University of Hong Kong, Hong Kong; ³Texas A&M University-Commerce, Commerce, TX 75428; ⁴Trinity University, San Antonio, TX, 78212. (mest@psi.edu)

Introduction: The eastern rim of Hellas basin and the surrounding highlands preserve a geologic record that spans most of the Martian time-scale [1-12]. Through geologic mapping and morphologic and spectral analyses, this investigation is exploring the geologic and hydrologic histories of this region, where important spatial and temporal relationships between volcanic and volatile-driven processes are preserved. Northeastern Hellas displays a unique confluence of ancient rugged highlands, volcanic terrains of the Tyrrhenus Mons lava flow field and flanks of Hadriacus Mons, the canyons of Dao and Niger Valles, channelled plains, and geologically young volatile-rich mass wasting and mantling deposits.

Data and Methods: We are using a THEMIS daytime thermal infrared (dTIR) brightness temperature mosaic (~100 m/pixel) as our primary mapping base. CTX (~5 m/pixel), THEMIS VIS (~18 m/pixel) multi-band HiRISE (<1 m/pixel), and MOC-NA (~1.5-12 m/pixel) images provide high-resolution views of the surface that allow detailed analyses of mapped units and features. CRISM multispectral (~100-200 m/pixel) and hyperspectral (~18-36 m/pixel) data are being used to show the distribution of primary minerals and their alteration products within surficial materials. Crater size-frequency distribution statistics and stratigraphic relationships are used to determine absolute model ages and relative ages, respectively. Image, topographic, and spectral datasets are compiled in ArcGIS to map geologic units and features in the study region. This effort has produced a 1:1M-scale geologic map of MTM quadrangles -35262, -35267 and -35272 (Fig. 1).

Mapping Results: We are mapping geologic features and units that define highland, volcanic, and plains materials, as well as impact craters that show a range of sizes, morphologies, and ages. Mapping shows that several units display evidence for incorporation of volatiles during formation, such as some ejecta and mass wasting deposits. Mapping also shows that nearly every surface in the map area has been modified to some degree by volatile-driven processes ranging from gullies along highland knobs, crater rims, and valles walls, to single channels and valley networks incised within volcanic and plains materials.

Highland terrains are located in the southeastern and western parts of the map area, and consist of massifs and clusters of rounded knobs and rims of degraded impact craters that are mapped as mountainous material (unit m). Mountainous material consisting of clusters of peaks have intermontane areas that appear smooth in THEMIS images, but show a diversity of pitted, lineated and smooth surfaces in CTX

images. Most intermontane areas are too small to be separated into individual units and are thus mapped as mountainous material.

The surfaces of most units in the map area are coated with mid-latitude mantling deposits [13]. These materials are being modified and/or removed in places via slope processes, deflation or erosion, which is most evident on steeper slopes. The steep slopes of mountainous material, valles walls, and crater rims show evidence for viscous flow and dissection by narrow parallel gullies. Some peaks of mountainous material in the southeastern part of the map area are surrounded by deposits that exhibit lineated surfaces and lobate edges. The orientations of the lineations suggest flow of material from the peaks. These deposits are mapped as debris apron material (unit da), and likely consist of coalesced debris aprons.

The Tyrrhenus Mons flow field (unit tmff) is large lava flow field that extends from the summit region of the volcano and whose distal end lies within the map area. Flow lobes have sinuous planform shapes, and elongate, broad, and digitate morphologies. Lobe margins range from subtle to well-defined, and variations are observed both within an individual flow and between different flows. Surface morphology and stratigraphic relationships observed in CTX images are used to evaluate sequences of flow emplacement. Some narrow channels observed in tmff display leveed margins and are associated with flow lobes; however, many channels in tmff lack these features and appear to be erosional [14,15]. Some fluvial channels are narrow and indicate confined flow; other channels are broad and braided and show evidence for overland flow.

The southernmost extent of the Hadriacus Mons flank material (unit hmf) occupies the north-central part of the map area. Previous studies have shown that these deposits consist of layered pyroclastic materials likely emplaced over multiple eruptive events [11,16-19]. Flank materials exhibit layering and are characterized by numerous broad valleys that radiate from the volcano's summit (north of map area). Most valleys are incised with narrow channels, but some broader valleys contain channels that are sinuous and braided. Wrinkle ridges are oriented parallel and perpendicular to the flank slopes, deform the flank materials, and occur as either broad ridges topped with a narrow crenulated ridge or just a narrow crenulated ridge [20].

Plains materials occupy a large part of the map area. In THEMIS, plains exhibit relatively smooth surfaces of mottled or moderate to low brightness that are dissected by channels and ridges. In CTX, it is apparent that plains units have undergone more

significant surficial and structural modification. Here, we have subdivided the plains into four distinct units: smooth, etched, knobby, and lobate plains.

Smooth plains material (unit ps) is the most widespread plains unit in the map area, and is cut by narrow sinuous channels, wide sinuous canyons, narrow linear valleys, linear fractures, and sinuous chains of pits. In CTX, the surface is pock-marked with low-relief pits and undulations, and scattered low-relief mounds. No primary volcanic features are visible. Wrinkle ridges within ps are oriented radial and circumferential to Hellas basin. The smooth plains forms fractured blocks and mesas where it has collapsed to form sections of Dao and Niger Valles and smaller canyons.

Etched plains material (unit pe) occurs in several small patches in the eastern part of the map area. CTX images show the etched texture is formed by sinuous low-relief ridges and knobs that join to form shallow irregular depressions, and elongated lobate structures that degrade into sinuous ridges and knobs. Some pe deposits are in contact with or in proximity to tmff and moderately degraded ejecta. Some exposures are dissected by sinuous channels.

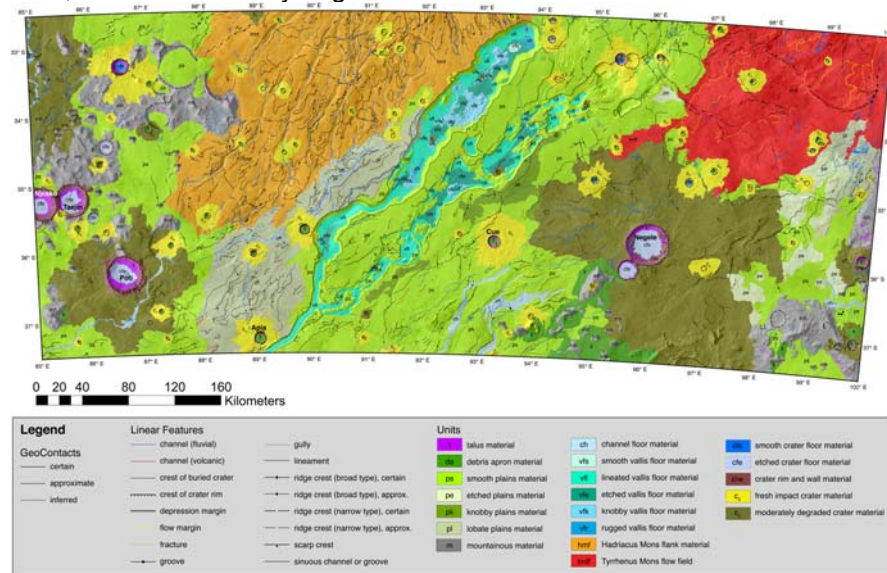
Knobby plains material (unit pk) occurs as two small exposures near the eastern bank of Niger Vallis and adjacent to the Negele ejecta deposit. The knobby plains consist of clustered to scattered low-relief knobs, and larger lobate mesas and sinuous ridges.

Lobate plains material (unit pl) forms one large deposit just west of Dao Vallis and south of hmf, and several smaller deposits just south of tmff. In THEMIS, the lobate plains appear generally moderate in brightness, but appear dark where directly adjacent to downslope terminations of tmff and hmf. Parts of pl contain sinuous lobate structures elongated to the southwest; lobes occur as individual features south of tmff and sequences of overlapping structures south of hmf. Deposits contain linear channels bounded by levees, and are dissected by single and braided channels.

The overall featureless nature of ps suggests it is likely composed primarily of eroded sedimentary materials, but the presence of volcanic channels and pit chains suggests there could be a volcanic component. The morphology, presence of leveed channels and pit chains, and proximity to tmff and hmf suggests pl could be volcanic in nature, possibly representing eroded extensions of tmff and hmf. Surface textures and locations of pe and pk suggest they could consist of eroded or collapsed/sublimated ps or pl or crater ejecta.

Ongoing Work: We are in the process of finalizing crater counts for each unit and will be incorporating these data into a formalized COMU.

References: [1] Schultz, R.A., and H.V. Frey (1990) JGR, 95, 14,175-14,189. [2] Greeley, R., and J.E. Guest (1987) U.S.G.S. Misc. Inv. Ser. Map I-1802-B, 1:15M. [3] Crown, D.A., et al. (1992) Icarus, 100, 1-25. [4] Crown, D.A., et al. (2005) JGR, 110, E12S22, doi:10.1029/2005JE002496. [5] Tanaka, K.L., and G.J. Leonard (1995) JGR, 100, 5407-5432. [6] Leonard, G.J., and K.L. Tanaka (2001) U.S.G.S. Geol. Inv. Ser. Map I-2694, 1:5M. [7] Mest, S.C., and D.A. Crown (2001) Icarus, 153, 89-110. [8] Schultz, P.H. (1984) Proc. Lunar Planet. Sci. Conf., 15th, 728-729. [9] Bleamaster, L.F., and D.A. Crown (2010) U.S.G.S. Sci. Inv. Ser. Map 3096, 1:1M. [10] Moore, J.M., and K.S. Edgett (1993) Geophys. Res. Lett., 20, 1599-1602. [11] Crown, D.A., and R. Greeley (2007) U.S.G.S. Sci. Inv. Ser. Map 2936, 1:1M. [12] Price, K.H. (1998) U.S.G.S. Misc. Inv. Ser. Map I-2557, 1:1M. [13] Mustard, J.F., et al. (2001) Nature, 412, 411-414. [14] Crown, D.A., and S.C. Mest [2014] Lunar and Planet. Sci. Conf. 45th, Abstract 2471. [15] Crown, D.A., and S.C. Mest (2015) Lunar and Planet. Sci. Conf. 46th, Abstract 2122. [16] Greeley, R., and P.D. Spudis (1981) Rev. Geophys., 19, 13-41. [17] Crown, D.A., et al. (1988) Lunar and Planet. Sci. Conf., XIX, 229-230. [18] Crown, D.A., and R. Greeley (1993) JGR, 98, 3431-3451. [19] Williams, D.A., et al. (2007) JGR, 112, E10004, doi:10.1029/2007JE002924. [20] Kortenien, J., et al. (2010) Earth and Planet. Sci. Lett., 294, 466-478.



Acknowledgements: This research is funded by the NASA Planetary Geology and Geophysics Program (PG&G) under grant number NNX13AR15G.

Figure 1. Geologic map of MTM quadrangles -35262, -35267 and -35272. Image base is THEMIS day IR mosaic (100 m/pixel); projection is Mars Transverse Mercator.

Preliminary Volcanic Feature Analysis of Olympus and Ascræus Mons, Mars. K.J. Mohr¹, D.A. Williams¹, W.B. Garry², and Jacob E. Bleacher² ¹School of Earth & Space Exploration, Arizona State University, Tempe, AZ 85282, kyle.mohr@asu.edu, ²Planetary Geology, Geophysics, and Geochemistry Laboratory, Code 698, NASA Goddard Space Flight Center, Greenbelt, MD 20771.

Introduction/Background: Olympus Mons (OM) and Ascræus Mons (AM) are two large shield volcanoes found in the Tharsis province on Mars. Both volcanoes have been recently mapped at a 1:1,000,000 scale using high resolution imagery [1,2]. Mapping of Arsia and Pavonis Montes are still in progress. With the completion of the Olympus and Ascræus Montes maps, direct comparison of volcanic features found on each edifice can be done. Rose diagram analysis shows strong similarities in specific features found on the two large volcanoes, further suggesting a similar formation and evolution.

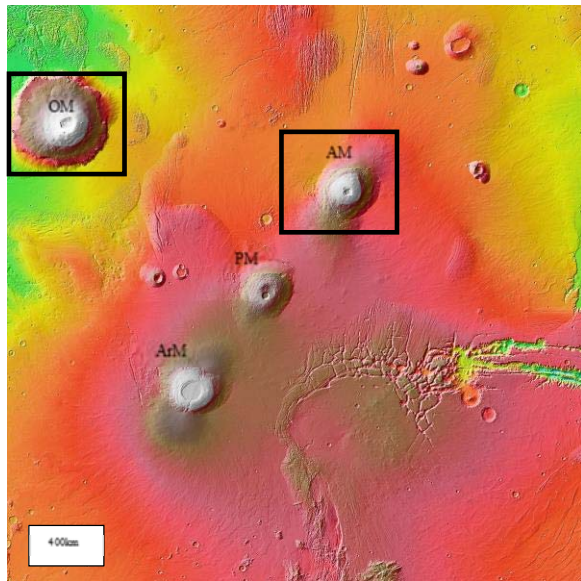


Figure 1. MOLA image of the Tharsis Montes, Olympus Mons and Ascræus Mons are indicated by the black squares.

Data and Methods: Geologic Maps for Olympus and Ascræus Montes were prepared in ArcGIS at a 1:1,000,000 scale using CTX, THEMIS, MOLA, and HRSC imagery. Volcanic features such as geologic units, linear features (rilles, volcanic channels, and graben), and location point features (fan apex, small shields, and flank vents) were mapped.

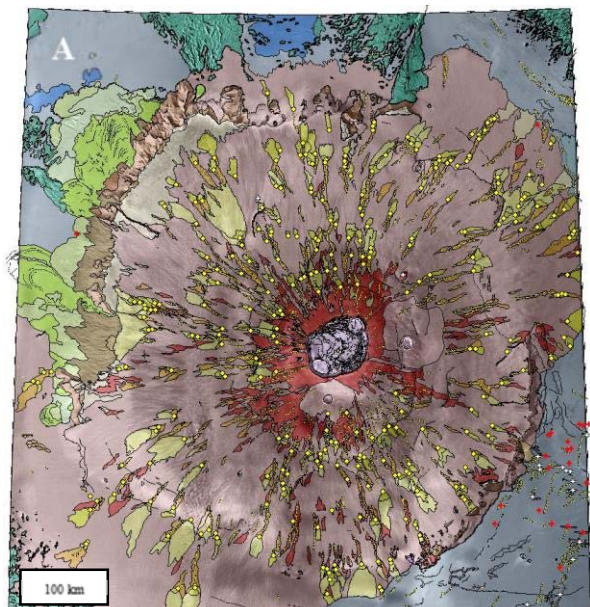
Rose diagrams were then created by first using the Generate Near Tool in ArcGIS to identify where each feature was located from a certain position on the volcano. The center point for each volcano was located at the center of each of the caldera complexes. Flank channel units were not taken into account in the study due to the fact these flows are dominantly found on all flanks of both volcanoes.

Only features observed on the flanks of the volcanoes were used in this study. However, future work will include small shields found on the surrounding plains of each of the Tharsis Montes.

Geologic Observations: Both Olympus Mons and Ascræus Mons are dominated by flank channel flows that embay older flank ridge flows, suggesting a change in lava properties from a less viscous effusive flow to a more viscous effusive flow [1,2]. Lava fans are also observed on both volcanoes, which are fan-like features where a sudden change in slope allowed for a tube-fed flow or vent to extrude lava into a deltaic shape. These lava fans are dominantly found on flank terraces, (sharp breaks in slope towards the base of the volcano) and have a gentle convex topographic profile [3,4].

Lava fans and flank ridge flows are dominantly found on the northwest and southeast flanks of both OM and AM. The NW and SE flanks are also where terraces are more commonly observed [4]. Flank terraces are believed to form by the flexure of the underlying lithosphere due to the overbearing weight of the material comprising the main shields [4,5].

It has been suggested that OM has been spreading apart in a NW/SE orientation [1]. There has been debate over whether or not AM is also spreading in a NW/SE direction [5,6]. Preliminary work using rose diagram analysis of the volcanic features on both volcanoes shows a very strong correlation of where these features



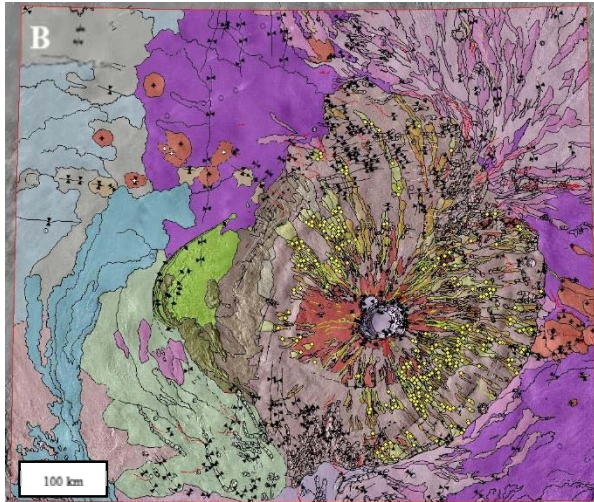


Figure 2. A) 1:1M scale geologic map of Olympus Mons. B) 1:1M scale geologic map of Ascræus Mons. Yellow dots indicate a fan apex.

are observed on the flanks of each volcano. This observation suggests that Ascræus Mons in fact may be spreading similarly to Olympus Mons.

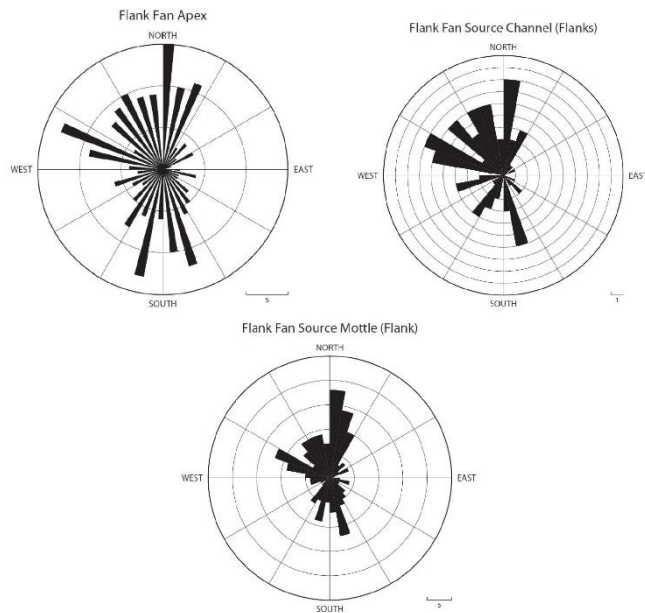


Figure 3. Rose diagrams showing the distribution of features on Olympus Mons. The Fan Apex diagram shows the distribution of all the fan apex on the flank of OM. The Fank Fan Source Channel and Mottle break up the Fan Apex into the two types of fans located on OM.

Discussion: Newly finished mapping of Olympus Mons and Ascræus Mons at a 1:1,000,000 scale allows for a direct comparison analysis for the volcanic features observed on both volcanoes. The similarities in location where many of these features are found on each volcano further suggests that a similar evolution and formation process for the two volcanoes. Future

investigation of the two volcanoes will include low shield volcanoes located off the NW and SE flanks of the two volcanoes. The dense location of these low shields, as well as the superposition ages of these features, suggests that they may have formed due to overbearing weight of the flanks causing pre-existing dikes to propagate off the flanks and onto the surrounding plains. When mapping is finished for Arsia and Pavonis Montes a similar study will be done to compare the four large Tharsis volcanoes.

References: [1] Bleacher J. E. et al. (2007) JGR, 112, E04003, doi:10.1029/2006JE002826. [2] Mohr et al. (2017) LPSC 48 #1306. [3] Thomas et al. (1990), JGR 95, 14345-14355. [4] Byrne et al. (2009) Earth and Planetary Science Letters 281, 1-13. [5] Byrne et al. (2012) JGR, 117, E01004, doi:10.1029/2011JE003825. [6] McGovern and Morgan (2009) Geology, 37, 139-142, doi:10.1130/G25180A.1.

HIGH-RESOLUTION GEOLOGIC MAPPING IN EASTERN CANDOR CHASMA: 2018 STATUS REPORT. C. H. Okubo, US Geological Survey, 1541 E. University Blvd., Tucson, AZ 85721, cokubo@usgs.gov.

Introduction: This abstract summarizes current results from ongoing large-scale structural and geologic mapping in the eastern Candor Chasma region of Valles Marineris, Mars. The goal of this work is to advance current understanding of the coupled structural evolution of eastern Candor Chasma and the sedimentary deposits within it through a campaign of geologic unit and structural mapping at spatial resolutions that are at least an order of magnitude finer than has been achieved by previous studies in this part of Valles Marineris. Work is occurring in two map areas on and adjacent to Nia Mensa (Fig. 1). Mapping is most mature in the northern Nia Mensa map area and is the focus of this abstract.

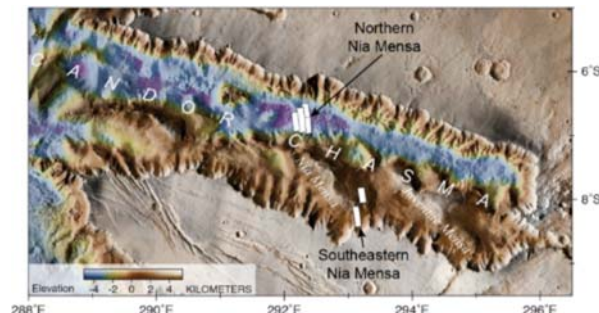


Figure 1. Location map of the northern and southeastern Nia Mensa map areas in eastern Candor Chasma. Image base is MOLA colorized elevation merged with THEMIS day IR.

Current results from the northern Nia Mensa map: This map area is defined by four overlapping High Resolution Imaging Science Experiment (HiRISE) stereo pairs and encompasses the contact between the northern flank of Nia Mensa and the lowlands to the north (Figs. 1 & 2). The area also contains a terraced fan-shaped landform on the lower slopes of Nia Mensa and also covers part of Nia Chaos, a small area of chaotic terrain within Candor Chasma.

This map area was initially planned to encompass only two HiRISE digital elevation models (DEMs). However, the local geologic history revealed by the initial mapping contained significant knowledge gaps with respect to the processes associated with development of the fan-shaped landform and Nia Chaos. Therefore an additional two HiRISE DEMs were added, and work over the past year has focused on mapping the two newly-added areas, integrating these new results with the mapping that had already been done in the initial map area, and ensuring that all areas were mapped consistently. Furthermore, the now larger map extent necessitates a change in the planned published map scale from 1:18,000 to 1:24,000.

Mapping is complete, and current efforts focus on finishing the various supporting map elements (map text, COMU, DOMU, EOMS, figures, etc.). A brief description of the select units and associated geologic events is provided below to summarize these findings.

The oldest observed bedrock in the map area is the Nia Mensa north variably layered (NM_{NVI}) unit, which underlies many of the knobs in the northwestern, central and southeastern portions of the map area. This unit is stratified, with layers that vary in thickness from ~1–10 m. Layer surfaces appear even and parallel, and numerous pinchouts and angular unconformities are present. Unit NM_{NVI} is interpreted as shallow lacustrine and/or eolian sediments (sand/mudstones and evaporites). All exposures of unit NM_{NVI} reveal inclined bedding of up to ~75°, indicating that this unit experienced post-depositional faulting and block rotation.

The Nia Mensa north rubbly unit (NM_{NR}) buries unit NM_{NVI}. Unit NM_{NR} appears massive and contains abundant meter-scale boulders within finer-grained matrix. Exposures of this unit have characteristically rough and rugose surfaces. Unit NM_{NR} is interpreted as matrix-supported breccia derived through landsliding of the chasma wall rocks.

The Nia Mensa north hummocky unit (NM_{NH}) buries units NM_{NR} and NM_{NVI}. Unit NM_{NH} comprises stratified materials wherein layer surfaces appear even to wavy and non-parallel. Exposures of unit NM_{NH} have a characteristically hilly terrain morphology and contain high fracture densities. Unit NM_{NH} is interpreted as lacustrine or aeolian sediments modified by post-depositional soft sediment deformation, and/or desiccated niveo-aeolian deposits.

The Nia Mensa north thickly layered unit (NM_{NTH}) buries units NM_{NS}, NM_{NH}, NM_{NR} and NM_{NVI}. Unit NM_{NTH} is characteristically well stratified, with layer surfaces that are even and parallel and lacks observed unconformities. Layers are ~2–10 m thick and internal cross-stratification is not apparent within individual layers. This unit is deformed by several large open folds and large fractures. Unit NM_{NTH} is interpreted as deep-water lacustrine sediments (sand/mud/siltstones) that were modified by post-depositional folding and fracturing.

The Nia Mensa discontinuously stratified unit (NM_{DS}) buries units NM_{NTH}, NM_{NS}, NM_{NH}, NM_{NR} and NM_{NVI}. Unit NM_{DS} is massive to weakly stratified, and its surface exhibits a characteristic mesh-like pattern of dark intersecting lines against a high-albedo bedrock. Unit NM_{DS} generally expresses the highest albedo of all the units in the map area and contains occasional sub-

horizontal layers of moderate albedo material. This unit forms steep to overhanging cliffs in the southern portion of the map area, and exfoliation sheets are common along cliff faces. Unit NM_{ds} is interpreted as duststones with minor interbedded aeolian sandstones.

The Nia Mensa north weakly stratified unit (NM_{Nws}) buries units NM_{ds} and NM_{Ntl} . Unit NM_{Nws} is massive to weakly stratified, and its layer surfaces are discontinuous, curved and non-parallel. Unit NM_{Nws} makes up the bulk of the fan-shaped landform in the southwestern portion of the map area. The middle- to lowest-elevation exposures of unit NM_{Nws} contain benches. Some of these benches continue laterally onto the adjacent rocks of unit NM_{ds} , implying that these benches are erosional in origin. The slope of the upper fan surface, above bench-modified section, is $\sim 5^\circ$, consistent with terrestrial arid-region alluvial fans [1] and arguing against a fluviially-dominated origin. Unit NM_{ds} is interpreted as sand/mudstones in a sand-dominated alluvial fan, and its prominent benches are interpreted as the result of paleo-shoreline incision.

The Nia Mensa north corrugated unit (NM_{Nc}) buries the northern-most occurrences of unit NM_{Nws} . The upper surface of unit NM_{Nc} exhibits characteristic subparallel, discontinuous ridges spaced ~ 5 – 15 m apart. Unit NM_{Nc} is interpreted as sandstones deposited in subaerial or subaqueous linear dunes.

The Nia Mensa north smooth mantle unit (NM_{Nsm}) buries units NM_{Nc} , NM_{Nws} , NM_{ds} , and NM_{Ntl} . Unit NM_{Nsm} is massive and its upper surface exhibits a smooth texture (at HiRISE scale) with mottled albedo. This unit covers much of the fan-shaped landform associated with unit NM_{Nws} and occasionally occurs in linear to irregularly-shaped deposits downslope of and subparallel to some benches. Unit NM_{Nsm} is interpreted as sands and finer-grained beach sediments derived from wave erosion of older units and reworking of derived sediments. Unit NM_{Nsm} was largely generated during lacustrine transgression and then locally eroded and reworked into beach ridges and bars during regression.

The Nia Mensa north squamose unit (NM_{Nsq}) buries units NM_{ds} , NM_{Nr} and NM_{Ntl} and occurs exclusively in the Nia Chaos portion of the map. Unit NM_{Nsq} is discontinuously stratified, with an upper surface that is characteristically platy, with some areas that have a smooth texture (at HiRISE scale). Unit NM_{Nsq} forms raised rims

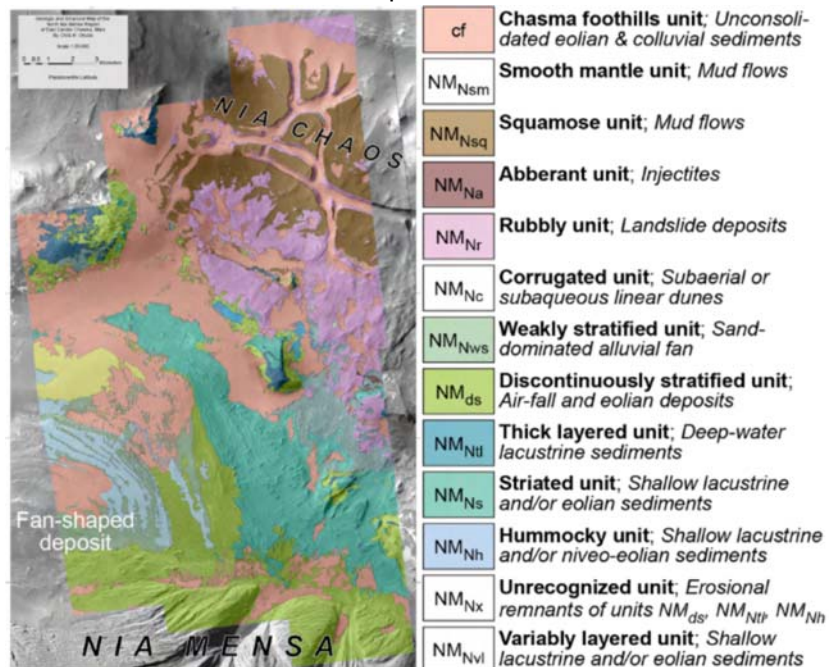
along the troughs of Nia Chaos and exhibits lobate to digitate distal margins that roughly conform to the preexisting terrain. This unit also derives fine-grained colluvial deposits along cliff faces. Unit NM_{Nsq} is interpreted as mudflows consisting of sands and finer-grained sediments derived from mobilization of water-saturated sediments within the subsurface. The formation of raised rims along the troughs of Nia Chaos suggests that this unit erupted out of those troughs from below the chaos—thus Nia Chaos formed due to subsurface sediment mobilization similar to Candor Chaos [2].

The Nia Mensa north aberrant unit (NM_{Na}) crosscuts units NM_{nds} , NM_{Ntl} , NM_{Nh} , and NM_{Nr} and does not appear to bury any units. Unit NM_{Na} is massive and forms seams and irregularly-shaped mounds that are commonly rounded with a pitted surface texture. Unit NM_{Na} is interpreted as injectites consisting of sands and finer-grained sediments derived from mobilization of water-saturated subsurface sediments.

Summary: Rocks of the northern Nia Mensa region record a rich geologic history reflecting sedimentation within a progressively deepening lacustrine environment, punctuated by mass wasting, subsurface sediment mobilization and chaos formation. Also significant is the preservation of paleo-shorelines and beach ridges on the alluvial fan and lower slopes of Nia Mensa, which provide evidence for late-stage lacustrine transgression and regression within this sedimentary basin.

References: [1] Blair T. C. and McPherson J. G. (1994) *J Sedimentary Res*, A64(3), 450–489. [2] Okubo C. H. (2016) *Icarus*, 269, 23–37.

Figure 2. (below) Thumbnail summary of the northern Nia Mensa map area.



2018 UPDATE ON THE GEOLOGIC MAP OF THE BOREALIS QUADRANGLE (H-1) ON MERCURY. Lillian R. Ostrach¹, Scott C. Mest², Louise M. Prockter³, Noah E. Petro⁴, and Paul K. Byrne⁵, ¹U.S. Geological Survey Astrogeology Science Center, Flagstaff, AZ, lostrach@usgs.gov, ²Planetary Science Institute, Tucson, AZ, ³Lunar and Planetary Institute, Houston, TX, ⁴NASA Goddard Space Flight Center, Greenbelt, MD, ⁵North Carolina State University, Raleigh, NC.

Introduction: We are drafting a new geologic map of the northern polar region of Mercury (H-1 Borealis Quadrangle) with MESSENGER observations at 1:5M map scale. Our mapping leverages the 1:15M-scale global geologic map [1–3], which provides context for mapping in the H-1 quadrangle and also serves as one of several bases for geologic unit and feature definition. Importantly, the new H-1 map will be among the first USGS Scientific Investigations Map (SIM) series quadrangle maps published using MESSENGER data—and thus provides an opportunity to establish basic standards and practices for quadrangle mapping of Mercury in conjunction with the global map and other quadrangle efforts now being prepared for USGS publication.

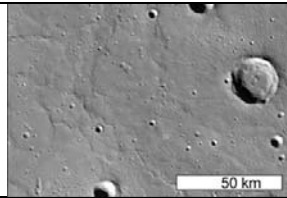
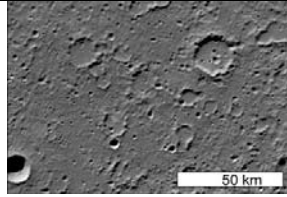

Mapping Progress: In 2018 (Project Year 2), we are focused on determining relative ages for units and features through the use of stratigraphic relationships and crater analyses. Our strategy relies on a combination of measured crater densities and crater size–frequency distributions for those geologic units with sufficient areal extent, coupled with evaluation of stratigraphic relationships for features (and feature classes) and spatially limited geologic units. We are classifying impact structures ≥ 20 km in diameter and their related materials according to degradational state, applying the methods used in the new global geologic map [e.g., 4]. We continue to refine geologic unit definitions to best represent our mapping; at the same time, we are striving for con-

sistency with the units identified and described by previous and ongoing mapping efforts, such as those from the original H-1 quadrangle map [5], the current global map [1–3], recently NASA-funded quadrangles [e.g., 6], and other quadrangles mapped as part of planning activities for the upcoming ESA BepiColombo mission [e.g., 6, 7].

In the map we identify three types of impact craters: pristine, degraded, and buried [Fig. 1]. Additionally, we take a conservative approach to mapping ridges and show the best-expressed ridge crests [Fig. 2]. We have identified three plains units [Table 1]: smooth plains (unit ps) and two intercrater plains units, intercrater plains (younger) and (older) (units pi1 and pi2, respectively), distinguished primarily on the basis of superposed crater areal density.

Acknowledgments: This work is funded by the NASA PDART Program under grant number NNN16AD15I awarded to L.R. Ostrach.

References: [1] Prockter, L.M. et al. (2016) LPS 47, Abst. 1245. [2] Kinczyk, M.J. et al. (2016) PGMM, Abst. 7027. [3] Kinczyk, M.J. et al. (2017) 3rd Planetary Data Workshop, Abst. 7116. [4] Kinczyk, M.J. et al. (2017) LPS 48, Abst. 2717. [5] Grolier, M.J., Boyce, J.M. (1984) Map I-1660, Misc. Investigations Ser., USGS. [6] Whitten, J.L. et al. (2018) PGMM, this volume. [7] Galluzzi, V. et al. (2016) J. Maps 12, 227–238. [8] Rothery, D.A. et al. (2017) LPS 48, Abst. 1406.

Unit	Description	Definition	Image
ps	smooth plains	Flat to gently rolling plains, sparsely cratered, occurring in topographically low areas (Borealis Planitia) and within some basins. Stratigraphically younger than other plains materials. Contacts with older units observed to be sharp with distinct boundaries in some locations or exhibiting a gradational contact (where older terrain was embayed).	
pi1	intercrater plains (younger)	Lie between large craters and basins, contains fewer superposed craters (~5–15 km diameter) than pi1 and more than ps, appear to have lower albedo than ps and pi2. Texturally intermediate between ps and pi2: rougher than ps and smoother than pi2. Embayment relations with ps gradual without a distinct contact. Boundaries with pi2 uncertain; approximate contact.	
pi2	intercrater plains (older)	Lie between large craters and basins, contains highest areal density of superposed craters (~5–15 km diameter) of plains units, hummocky texture. Contacts with pi1 indistinct and uncertain. Some contacts with ps distinct, whereas others gradational.	

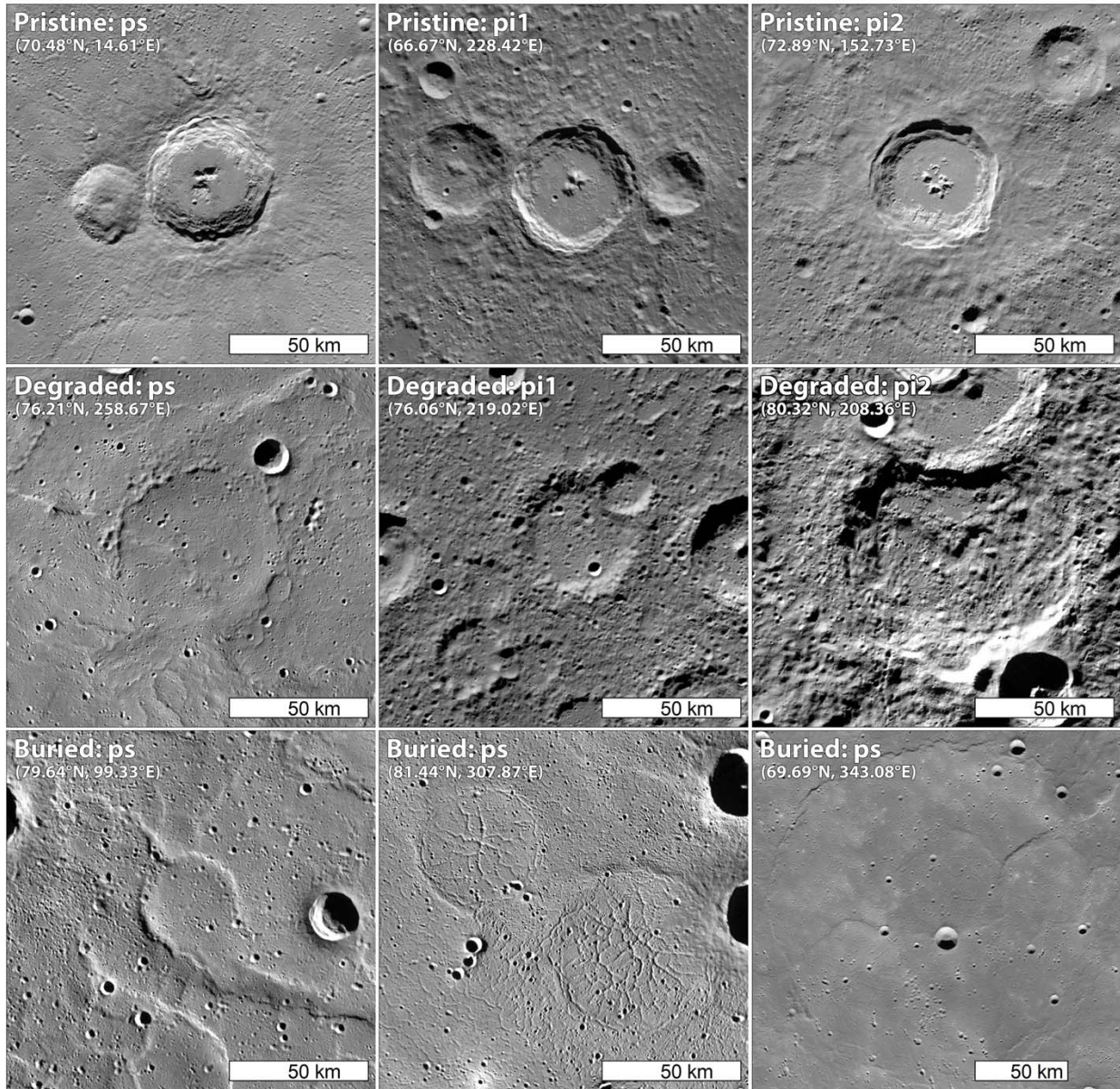


Fig. 1 (above). Three types of impact crater are currently identified on the map: pristine, degraded, and buried. For now, craters ≥ 20 km in diameter are shown on the map.

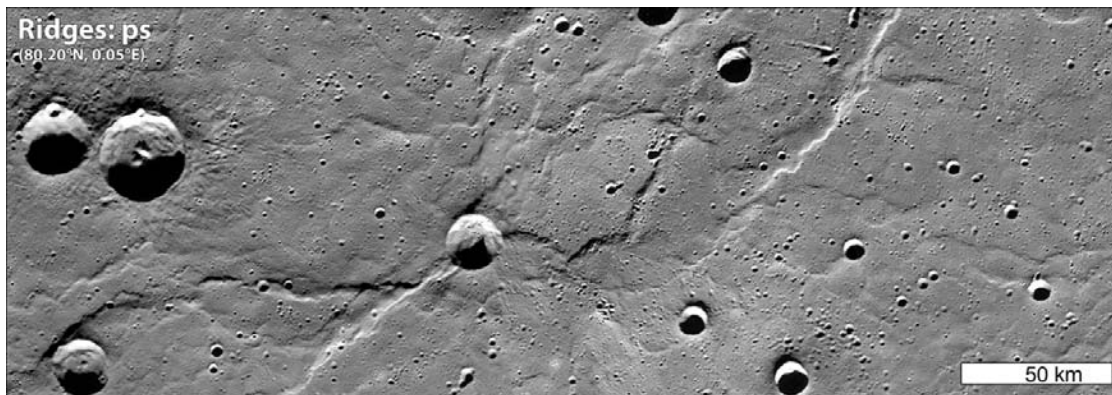


Fig. 2 (left). Ridges are a prominent landform type in the smooth plains unit. For clarity, we do not map those ridges interpreted to be rim crests of buried craters.

ENIGMATIC SEDIMENTARY DEPOSITS WITHIN PARTIALLY EXHUMED IMPACT CRATERS IN THE AEOLIS DORSA REGION, MARS: EVIDENCE OF PAST CRATER LAKES. S. E. Peel¹ and D. M. Burr¹, ¹Department of Earth and Planetary Sciences, University of Tennessee, Knoxville (speel1@vols.utk.edu).

Introduction: The Medusae Fossae Formation (MFF) on Mars is an expansive sedimentary deposit of uncertain origin [e.g., 1-6, and citations therein] located west of Tharsis and east of Gale Crater. Within the westernmost extent of the MFF are a plethora of sinuous ridges interpreted as inverted fluvial deposits formed through the removal of previously overlying and adjacent material [e.g., 7-9]. These features are spatially concentrated within the depression between the two high-standing plana (Aeolis and Zephyria Plana), a region called Aeolis Dorsa (Fig. 1).

As part of a larger mapping effort within this area [10-11], we have mapped enigmatic sedimentary deposits found within partially exhumed impact craters (Fig. 1) using CTX [12] and HiRISE [13] images in ArcGIS [14]. Here, we give brief descriptions (Fig. 2) and preliminary interpretations for these intracrater deposits, as well as possible correlative stratigraphy (Fig. 3).

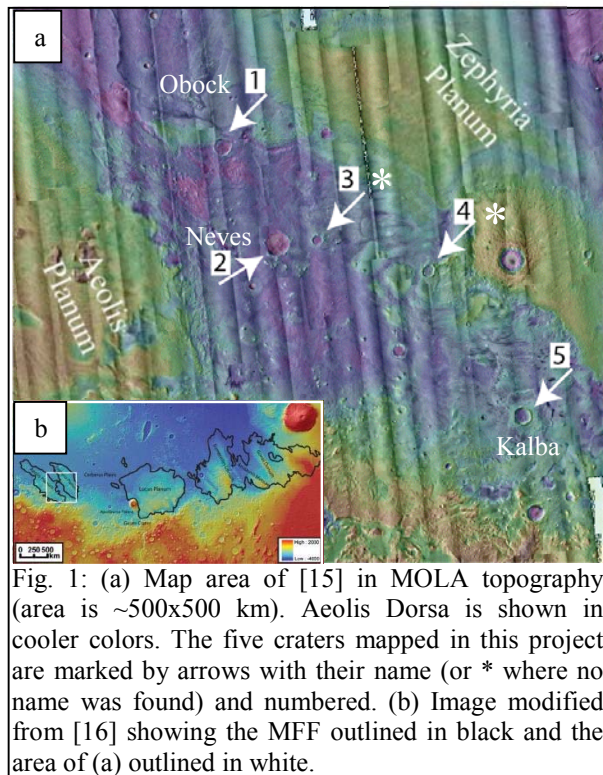


Fig. 1: (a) Map area of [15] in MOLA topography (area is ~500x500 km). Aeolis Dorsa is shown in cooler colors. The five craters mapped in this project are marked by arrows with their name (or * where no name was found) and numbered. (b) Image modified from [16] showing the MFF outlined in black and the area of (a) outlined in white.

Unit Descriptions and Interpretations:

Branching Unit (b) – Fine-grained with surfaces that smoothly transition to different elevations over large areas, forming an overall branching appearance.

Interpretation: paleo-fluvial deposits.

Concentric Ringed Unit (cr) – Layered with upper surface broken by concentric rings of irregularly to sinuously edged, pock-like depressions. Cliff-forming boundaries common. *Interpretation:* fine-grained deposits of lacustrine or aeolian origin.

Crater Floor Unit (cf) – Largely smooth surface with many occurrences of linear and sinuous ridges and irregular high-standing features. *Interpretation:* Impact melt or fine-grained sedimentary deposits with hydrothermally deposited minerals likely.

High-standing Unit (h) – High-standing, semi-connected to disconnected mounds with serrated appearance to edges. Upper surfaces often form amphitheater pattern of stepped rings. *Interpretation:* lacustrine or aeolian deposits with fine layering common.

High-standing Ridged Terrain (hr) – High-standing with approximately uniform elevation throughout and cliff-forming boundaries. Upper surface has similarly striking ridges. Occurs over wide areas and as separate ridges (mapped separately). *Interpretation:* delta sedimentary fan and inverted fluvial features.

Irregular Pocked Unit (ip) – Rough surface broken up by depressions of variable size. Irregular peaks and mesas that erode into large blocks with or without cliff-forming edges common. *Interpretation:* fine-grained deposits of lacustrine or aeolian origin.

Knobby Unit (k) – Preserved as approximately circular or elongate knobs, usually striking NW. Internal layering of coarse and fine materials common. *Interpretation:* cyclic origin likely, possibly within a lake.

Lineated Unit (l) – Arcuate to swirling lineations of light and dark materials. Alternates between protruding and recessive expressions over steep slopes. *Interpretation:* lacustrine or aeolian deposits with subsequent chemical alteration likely.

Sinuuous Unit (s) – Sinuous ridges that smoothly transition or abruptly jump in elevation. Rarely occurs with branching planview. *Interpretation:* inverted fluvial features.

Sinuuous Mesa Unit (sm) – High-standing with irregular, discontinuous, and undulating surfaces. Cusped, cliff-forming edges common. Fine-grained material that erodes into blocks in some areas. *Interpretation:* sediment transported and deposited by wave action in standing water. Long troughs are suggestive of ice-wedge marine scours.

Fig. 2 (left column): Examples of each of the mapped intracrater units. The labels correspond with their descriptions and are used in Figure 3.

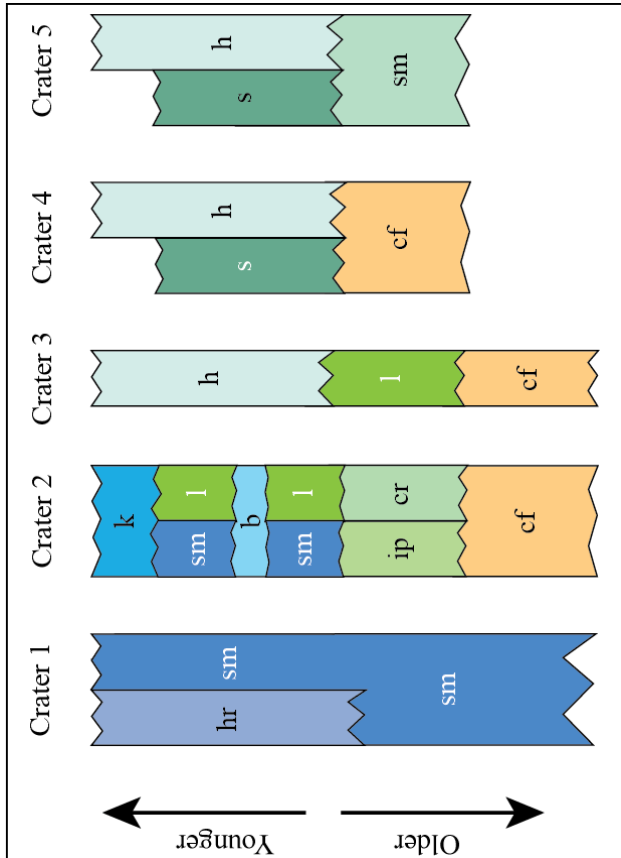
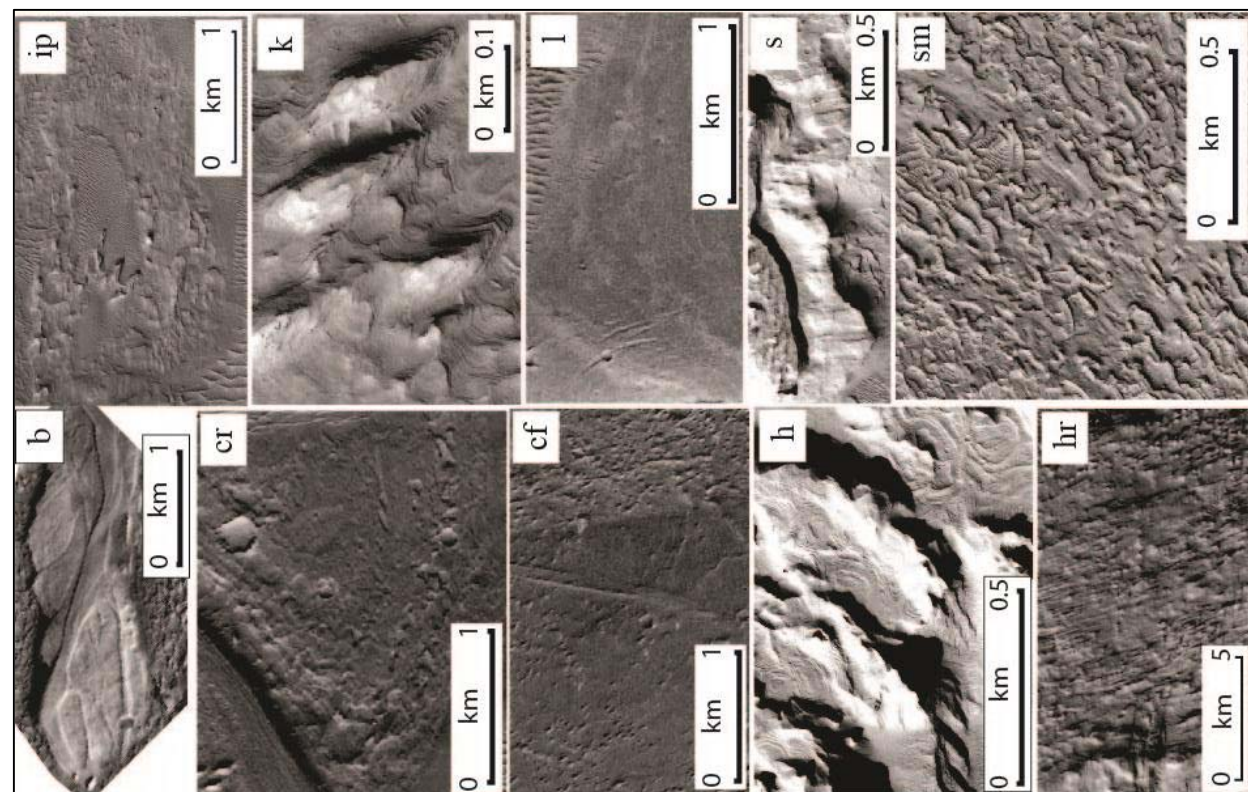


Fig. 3: Possible correlative stratigraphy of the mapped intracrater units. The unit labels are those used in the unit descriptions and in Figure 2.

References: [1] Scott, D.H., Tanaka, K. L. (1986) USGS, IMAP 1802-A. [2] Greeley, R., Guest, J. (1987) USGS, IMAP 1802-B. [3] Watters et al. (2007) *Science* 318, 1125-1128. [4] Mandt et al. (2008) *JGR Planets*, 113, E12011. [5] Harrison et al. (2010) *Icarus*, 209, 405-415. [6] Kerber et al. (2011) *Icarus* 216, 212-220. [7] Burr, D. M. et al. (2012), *JGR: Planets*, 117.E3. [8] Lefort, A. et al. (2015), *Geomorph.* 240 121-136. [9] Jacobsen, R. E., Burr, D. M. (2015) LPSC 46, abs.1832. [10] Burr, D. M. et al. (2017) *PGMM*, abs.7010. [11] Burr, D. M. et al. (2016) *PGMM*, abs. 7013. [12] Malin, M.C. et al. (2007) *JGR: Planets* (1991-2012) 112(E5). [13] McEwen, A. S. et al. (2007) *JGR: Planets*, 112, E05S02. [14] ESRI (2011) ArcGIS Desktop: Release 10.1. Redlands, CA: Environmental Systems Research Institute. [15] Jacobsen, R. E., et al. (2018) *this meeting*, abs. 7014. [16] Kerber, L., Head, J. W. (2010) *Icarus* 206, 669-684.

THE FRACTAL NATURE OF PLANETARY LANDFORMS AND IMPLICATIONS TO GEOLOGIC MAPPING. S.J. Robbins^{0,1}. ⁰stuart@boulder.swri.edu, ¹Southwest Research Institute, 1050 Walnut Street, Suite 300, Boulder, CO 80302.

Introduction: The primary product of planetary geologic and geomorphologic mapping is a group of lines and polygons that parameterize planetary surfaces and landforms. Many different research fields use those shapes to conduct their own analyses, and some of those analyses require measurement of the shape's perimeter or line length, sometimes relative to a surface area. There is a general lack of discussion in planetary science of the fact that perimeters of many planetary landforms are not easily parameterized by a simple aggregation of lines or curves, they instead display complexity across a large range of scale lengths; in fewer words, many planetary landforms are fractals.

Because of their fractal nature, instead of morphometric properties converging on a single value, those properties will change based on the scale used to measure them. Therefore, derived properties can change – in some cases, by an order of magnitude or more – just when the measuring length scale is altered. This can result in significantly different interpretations of the features. In this abstract, and at the Planetary Mappers' Meeting, I will discuss applications of fractals to problems of planetary mapping, interpretation, and related scientific investigations.

Application to Impact Crater Ejecta: The extent of crater ejecta can be an important component of mapping, but researchers who study crater ejecta typically want to characterize it further. Morphometric properties are almost exclusively derived from tracing the perimeter and deriving different metrics from that perimeter trace. These properties include: Perimeter, area, lobateness (Γ ; perimeter divided by the circumference of a circle with the same area), extent of the continuous ejecta from the rim, and ratio of that extent to the crater's size. Except area, all these metrics are affected by the fractal nature of the ejecta.

Figure 1a shows a simulated example of a complex pattern that has some similar properties to a real ejecta deposit. Figure 1b shows the measured perimeter and area of the shape (vertical axes) as different measuring length scales were used (ϵ , horizontal axis). Area converges to a single value, but there is no steady-state perimeter; in fact, the perimeter increases significantly at the smallest measuring lengths due to the extra complexity at those small scales. Therefore, Γ (Fig. 1c) also changed depending on ϵ , and that change was non-linear, not predictable, nor easily parameterized.

An additional problem of changing ϵ is two features that are identical in every way except scale, such as hypothetical ejecta from a 1 km diameter crater versus 10 km diameter crater, will have different perimeter versus area properties when measured with the same length scale. This is because more intricate features resolved at 10 m for the larger crater will not

resolve at 10 m for the smaller crater. Figure 1b illustrates this result with the example feature scaled up by a factor of 10, but keeping ϵ the same (the perimeter results are scaled to have identical values for $\epsilon \approx 0.3$, and the areas are scaled to have the same asymptotic values). The general trend is the surface area converges more quickly, but the perimeter again has non-linear behavior. (Non-linear behavior occurs at different ϵ because the shape is not a true fractal.) Therefore, Γ (Fig. 1c) is different for a given ϵ despite the identical nature of the underlying shape.

Application to One-Dimensional Features Studied in Two Dimensions: Valley networks and properties associated with them also should be considered in the context of fractals, such as stream order (branching complexity, known in mathematics as the Strahler number or Horton-Strahler number), stream length, and drainage density (valleys per unit area). These three properties have important implications for the valley network and the environment in which it formed. From Viking-era imagery, [1] produced maps of the valley network distribution on Mars. From a new generation of spacecraft, [2] identified many more, smaller valleys that were not visible in previous imagery, resulting in 8× more valleys, 2× more length, 2× higher stream order, and in some cases over 10× higher drainage density. The limiting factor here was primarily image resolution and quality, but the difference in detail one observes when examining fractals at finer scales. This emphasizes the need to remember “scale-based geologic mapping” is scale-based for a reason, and all interpretations and conclusions must be couched in caution due to this limiting scale and potentially a lack of higher quality data.

Application to Two-Dimensional Features Studied in Two Dimensions: Ballistic and flow processes – such as lava emplacement – often display fractal-like perimeters. The fractal nature of lava flows were studied extensively in the 1990s [3], and they demonstrated that plotting the measured perimeter versus measuring scale length yielded different and potentially diagnostic power-law fits, thus giving a diagnostic tool for differentiating between lava flow types simply from analyzing the fractal nature of the mapped units – and therefore a tool for understanding the underlying material properties and geophysics.

Issue of Data Scale and Resolution: A problem with remote sensing data is data fidelity: Whatever data are being analyzed exist at a finite resolution, and in practice this will limit the extent of the analyzable scales. Fractal characterization requires analysis at a range of scales, but that may not be possible given the data scale or resolution. There are significant practical

issues here, where it is possible that one may not be able to recognize whether a feature displays fractal-like characteristics. In such cases, it is the recommendation that researchers acknowledge this potential deficit. This was described above with respect to valley networks, but it also applies to such investigations as slopes (limiting fidelity of an elevation model can soften slopes), thermal inertia (a pixel is the average of all thermal inertia properties of exposed material in that pixel), and other studies.

Suggestion— Compute Fractal Dimension: Fractal dimension provide a simple metric to characterize the inherent complexity of a shape, and there are many methods to calculate $\frac{D}{\epsilon}$. A simple linear example starts by using $\epsilon = 1$. One might measure a river as having a length of $N = 3$ (length = “N” in fractal studies). If the length scale is decreased by $3\times$ ($\epsilon = 1/3$), one would expect the same $N = 3$, but instead $N = 4$ due to the meandering nature of the river. The fractal dimension can be calculated in two ways. The first method uses only the data at that point: $\frac{D}{\epsilon} = -\log(N) / \log(\epsilon) \approx 1.262$. Alternatively, one can graph $\log(N)$ versus $\log(\epsilon)$, and the fractal dimension is 1–slope, where “slope” is the slope of a best-fit line. In this example, the plotted values would be $x = \{\log(1/3), \log(1)\} \approx \{-0.477, 0\}$ and $y = \{\log(4), \log(3)\} \approx \{0.602, 0.477\}$, such that the best-fit line is $y \approx 0.477 - 0.262 \cdot x$, and the fractal dimension $\frac{D}{\epsilon} \approx 1 - (-0.262) \approx 1.262$, in agreement with the other method.

Conclusion: A final consideration is a practical one: Despite the examples described, the most common component of mapping in the planetary science community is the basic identification and tracing of physiographic units at a certain, singular scale, and how fractal considerations apply or could be applied may not be clear. In practice, one can take a mapped unit and compute the fractal properties. For purpose, it is my opinion that the fractal nature of units will rarely affect the actual process of mapping, for most mappers are interested in the area covered by units, and areas converge quickly to a single result. However, mappers often care about the perimeter of units, and in that measurement fractal considerations are important. Additionally, mappers usually want other researchers to use their product, and those other researchers may need to conduct analyses where the fractal nature of landforms will affect results. Additionally, as referenced with types of lava, directly characterizing the fractal nature of the perimeter can lead to important conclusions in themselves, which can affect the interpretation of mapped units.

The community should consider revisiting the fractal implications to mapping and especially to studies that rely on morphometric properties of those mapped units.

References: [1] Carr (1995) doi:10.1029/95JE00260. [2] Hynek et al. (2010) doi:10.1029/2009JE003548. [3] Bruno et al. (1992) doi:10.1029/91GL03039.

Funding: This work was funded in part by MDAP award NNX15AM48G.

Publication: This work has been accepted for publication: Robbins, S.J. (in press) “The Fractal Nature of Planetary Landforms and Implications to Geologic Mapping.” Earth & Space Sci.

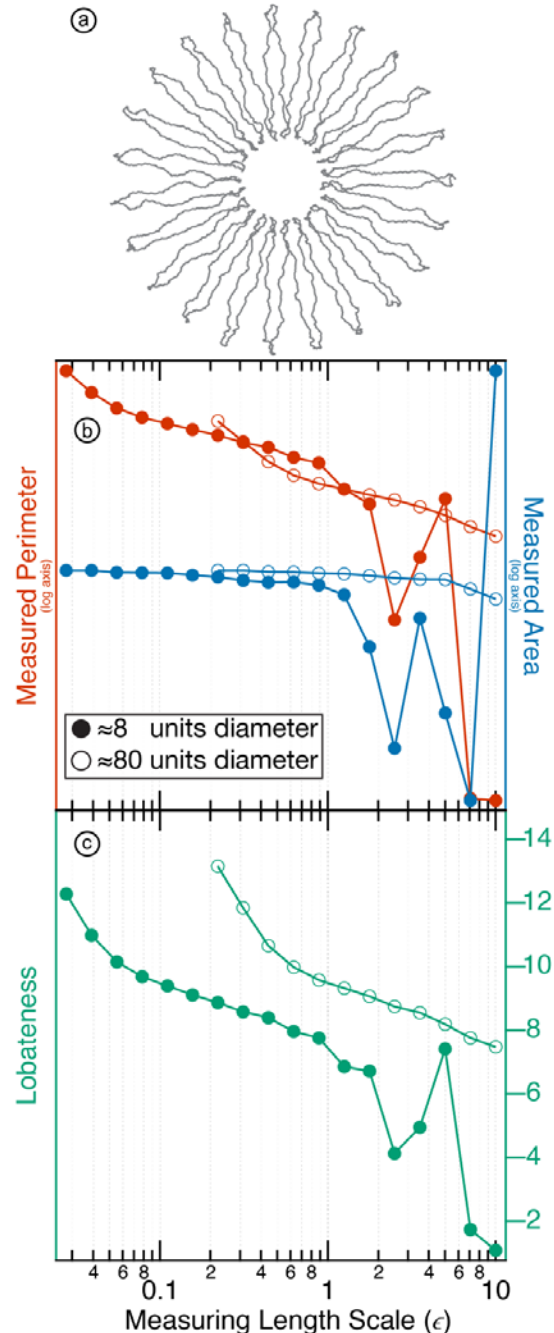


Figure 1: Simulated complex shape (a), the unitless measured perimeter and measured area (b), and derived lobateness (c) when shape is scaled from a large (open circles) to small (filled circles) size. The shape was created once, and the measuring length scale was adjusted in software (one can derive $\frac{D}{\epsilon}$ done with the original perimeter by using software).

GEOLOGIC MAP OF NEW HORIZONS' ENCOUNTER HEMISPHERE OF CHARON, V. S.J. Robbins^{0,1}, J.R. Spencer¹, R.A. Beyer^{2,3}, P. Schenk⁴, J.M. Moore³, W.B. McKinnon⁵, R.P. Binzel⁶, M.W. Buie¹, B.J. Buratti⁷, A.F. Cheng⁸, W.M. Grundy⁹, I.R. Linscott¹⁰, H.J. Reitsema¹¹, D.C. Reuter¹², M.R. Showalter², G.L. Tyler¹, L.A. Young¹, C.B. Olkin¹, K. Ennico³, H.A. Weaver⁸, S.A. Stern¹, the New Horizons GGI Theme Team, New Horizons Pluto Encounter Team, New Horizons LORRI Instrument Team, and New Horizons MVIC Instrument Team. ⁰stuart@boulder.swri.edu, ¹Southwest Research Institute, 1050 Walnut Street, Suite 300, Boulder, CO 80302. ²Sagan Center at the SETI Institute. ³NASA Ames Research Center, Moffett Field, CA 84043. ⁴Lunar and Planetary Institute, Houston, TX. ⁵Washington University in St. Louis, St. Louis, MO. ⁶Massachusetts Institute of Technology, Cambridge, MA. ⁷NASA Jet Propulsion Laboratory, California Institute of Technology, Pasadena, CA. ⁸The Johns Hopkins University, Baltimore, MD. ⁹Lowell Observatory, Flagstaff, AZ. ¹⁰Stanford University, Stanford, CA. ¹¹Bal Aerospace (retired), Boulder, CO. ¹²NASA Goddard Space Flight Center, Greenbelt, MD.

Introduction: NASA's New Horizons spacecraft revealed diverse landscapes on both Pluto and Charon during its July 2015 flyby, and we are undertaking geomorphologic mapping efforts [1,2] to better understand the different landforms, how they may have formed, and relative timing. The work herein focuses on Charon, and images from the spacecraft have revealed a variety of features [3,4] that include hundreds of tectonic manifestations [5] and vast but diverse plains [6]. We present progress in mapping the hemisphere that New Horizons best imaged during its flyby and will present a finished map, as submitted for peer-review, at the Meeting.

Available Data: Data taken directly by New Horizons relevant for geomorphologic mapping come from LORRI (LOng-Range Reconnaissance Imager) [7], MVIC (Multi-spectral Visible Imaging Camera) [8], and LEISA (Linear Etalon Imaging Spectral Array) [8]. LORRI is panchromatic and provided images of Charon at up to 160 m/px, MVIC 4-color images are up to 620 m/px, and LEISA spectral cubes are up to 5 km/px. Figure 1 shows the fractional coverage of Charon at panchromatic (LORRI and MVIC) wavelengths. Additional, derived data useful for mapping includes craters (useful for ages and as units if large enough) [9], reconstructed topography from stereo and photodolometry [10], and mineralogy maps (produced by the team). Our primary dataset for geomorphologic mapping of Charon is the panchromatic map reconstructed from LORRI and MVIC data.

Areas Identified for Nomenclature: For ease of communication, the New Horizons team developed informal names used herein. On Charon, these include two dark macula, 39 impact craters, seven chasmata, and three large montes. In addition, the very broad area north of a large tectonic belt has been termed "Oz Terra" and the smoother plains generally south of the belt are "Vulcan Planum."

Tectonic Features Mapping: Initial geomorphologic mapping focused on tectonic features in support of Beyer et al. [5]. This map was originally made without topography input but is in the process of being finalized with the PDS-released topography. Beyer et al. [5] found the majority of tectonic features are aligned northeast-southwest; this parallels the massive tectonic belt implying these features are likely related.

Based on superposed, large impact craters, we estimate the majority of the larger tectonic features formed ~4 Ga. However, crater density maps [9] show a deficit of craters in some areas that are possibly due to disruption by tectonic features, indicating that some tectonic activity may be significantly younger.

Vulcan Planum Mapping: Vulcan Planum is a younger region than Oz Terra [2,4,6,9], indicated by the spatial density of large craters. In topography, it shows a "moat" at its margins, possibly indicating a frozen viscous fluid flow [4,6]. We are in the process of studying this region [6] and the geomorphologic map has revealed only two primary types of landscape: smooth plains (Sm), and patterned ground (Pg1 and Pg2) which resembles an elephant skin-like texture. Near its southern margin, it also shows numerous broad warps that may represent upwelling.

Primary Ongoing Work: We are in the process of finalizing the map for submission to peer-review in a science journal. The primary work effort is currently focused on redrafting all line art with the final SPICE solution and basemap, for all original work is distorted on the latest maps. Additionally, we are focusing on the COMU (stratigraphy) of the units to piece together Charon's relative surface history.

References: [1] White, O.L. et al. (2017). [2] Singer, K.N. et al. (in rev). [3] Stern, S.A. et al. (2015). [4] Moore, J.M. et al. (2016). [5] Beyer R.A. et al. (2017). [6] Beyer R.A. et al. (in prep). [7] Cheng, A.F. et al. (2008). [8] Reuter, D.C. et al. (2008). [9] Robbins, S.J. et al. (2017). [10] Schenk, P. et al. (2016, in rev).

Funding: This work was funded by the New Horizons mission within NASA's New Frontiers program.

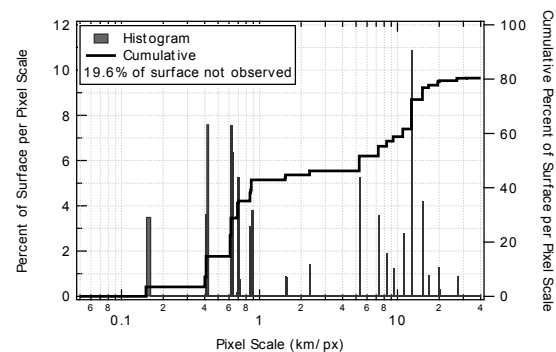


Figure 1: Pixel scale and fractional global coverage of New Horizons panchromatic imaging of Charon.

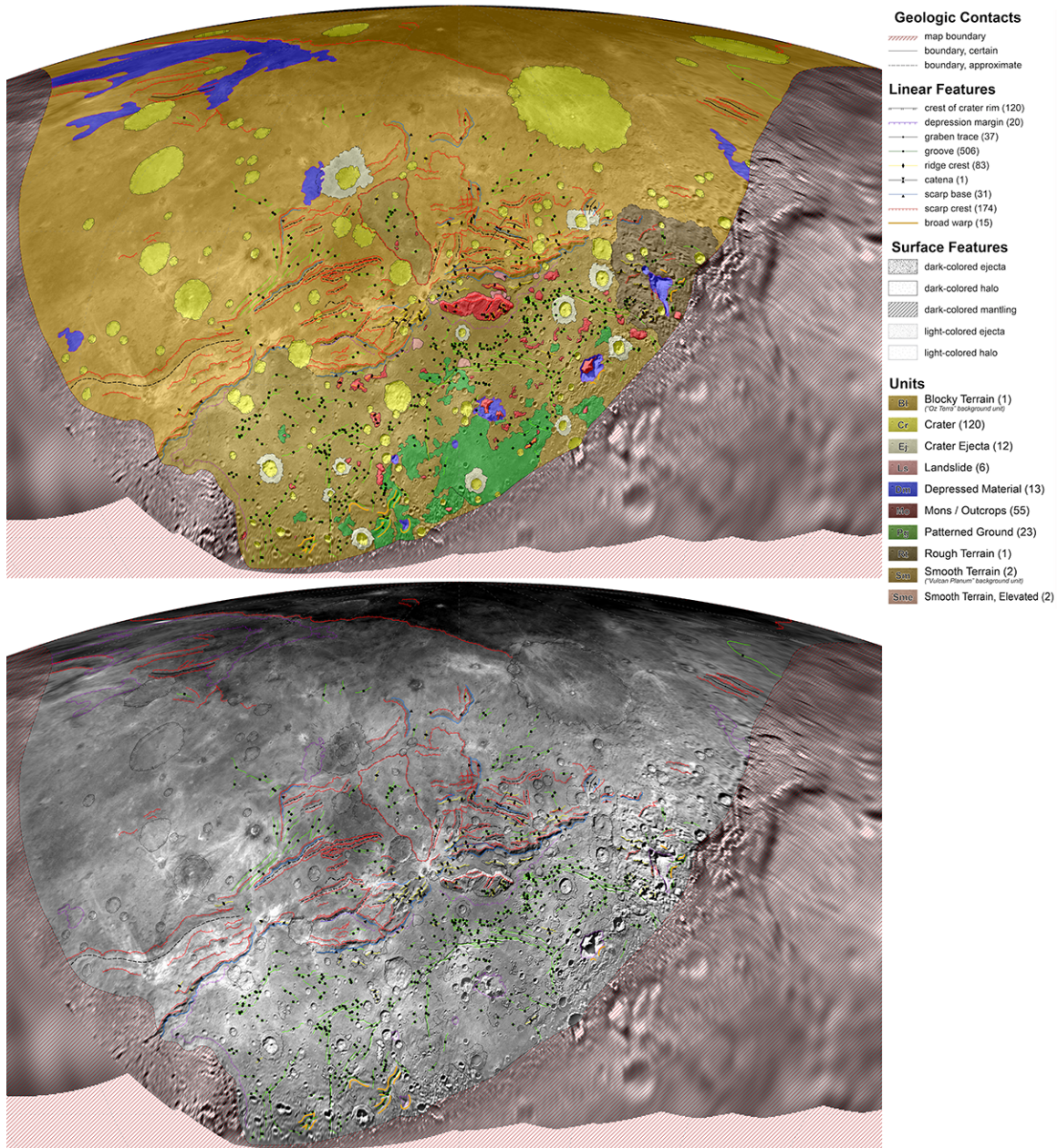


Figure 2: Map of the encounter hemisphere with geomorphologic units (top) and linear features (bottom) over greyscale basemap.

MINERALOGY OF HUYGENS BASIN, MARS: A TRANSECT OF NOACHIAN HIGHLANDS CRUST.

K. D. Seelos¹, S. E. Ackiss^{2,1}, F. P. Seelos¹, J. A. McBeck^{3,1}, D. L. Buczkowski¹, C. D. Hash⁴, C. E. Viviano¹, and S. L. Murchie¹, ¹JHU Applied Physics Laboratory, Laurel, MD (kim.seelos@jhuapl.edu); ²Purdue University, West Lafayette, IN; ³University of Oslo, Norway; ⁴Applied Coherent Technology Corporation, Herdon, VA.

Introduction: Huygens crater is an Early Noachian peak ring basin situated in the northwest rim region of Hellas (centered at 13.5°S, 55.5°E) (Fig. 1A). With a diameter of ~450km, Huygens uplifted and exhumed Noachian crustal materials from depths greater than 30 km, penetrating well below Hellas ejecta. Although the general highland crustal composition is dominated by mafic minerals (e.g., pyroxenes, olivine) [e.g., 1-3], numerous small outcrops of aqueously altered minerals, including phyllosilicates and carbonates, have been identified throughout the region [e.g., 4-6]. Determining the emplacement timing and stratigraphic relationships of these materials is critical for understanding the geologic history of the ancient martian highlands as a whole, and Huygens' size, age, and location is uniquely positioned to provide significant insight.

Datasets and Methods: We utilize a combination of data from the Compact Reconnaissance Imaging Spectrometer for Mars (CRISM) (180 m/pix; 20/40 m/pix) [7], Thermal Emission Imaging System (THEMIS) daytime IR and qualitative thermal inertia (100 m/pix) [8-9], and Mars Orbiter Laser Altimeter (MOLA) (128 pix/deg or ~460 m/pix) [10] to map the mineralogy and morphologic context of the materials found within and around Huygens basin. Locally, Context Camera (CTX) [11] and High Resolution Imaging Science Experiment (HiRISE) [12] data were used. ArcMap 10.5 was employed to manage these datasets and to facilitate unit delineation. In creating both the mineralogic map and morphologic sketch map, contacts were drawn where data is spatially coherent (inconsistent with noise) at 1:250K scale and using certain or approximate line styles to convey mapping confidence.

CRISM data processing. While all data are publicly available, additional processing of CRISM multi-spectral and hyperspectral, visible to near infrared (0.36-3.9 μ m) data was required. Twelve 5x5° multi-spectral map tiles (~180 m/pix), generated by a prototype processing pipeline [13], consist of calibrated, corrected, and mosaicked image strips rendered as a suite of red-green-blue (RGB) composites. RGB combinations of particular summary parameters [14-15], keyed to absorption features indicative of specific minerals, are the primary dataset for mapping the mineralogy. CRISM hyperspectral data (20 or 40 m/pix) were processed in parallel as Map-projected Targeted Reduced Data Records (MTRDRs) [16] but only used for mapping in a supplementary fashion because of their more limited spatial extent. MTRDR data, however,

were used for in depth spectral analysis to verify units and identify specific mineral species. Two main summary parameter composites were used for mapping: MAF is focused on distinguishing the mafic minerals olivine, low-calcium pyroxene (LCP), high-calcium pyroxene (HCP) and consists of the parameters OLINDEX3, LCPINDEX2, and HCPINDEX2, while PFM highlights Fe/Mg-bearing phyllosilicates or carbonates and consists of the parameters D2300, BD2355, and BD2290 [15].

Mapping Results: Morphologic Sketch Map Units. Based exclusively on THEMIS daytime IR and MOLA topography, we mapped 9 terrain types (Fig. 1B): dissected terrain, smooth intra- and intercrater plains, montes, mottled terrain, chaos-like terrains, and craters larger than 10km diameter with discernable ejecta. Intraring plains, mottled plains, and fractured mesas are all located interior to Huygens. Crater rim crests, graben traces, buried crater rims, and valley networks of order > 1 [17] are also demarcated. Due to its size, Huygens is transitional between peak rim and multiring basin, and the approximate position of a primary ring and partial second ring are indicated as well.

Mineralogic Units. Based on CRISM data and supplemented by THEMIS and MOLA, we identified four distinct mineralogic units: olivine-HCP, olivine, LCP, and altered (Fig. 1C). The latter is a short-hand to include any aqueously-altered secondary mineral; detailed spectral analysis revealed the presence of Fe/Mg smectites, chlorite, probable carbonate, and Al smectite or kaolinite. For all but the olivine-HCP unit, individual outcrops are often small and/or widely dispersed, and so are difficult to make out at the resolution of Figure 1C.

Synthesis. Mineralogy-morphologic associations in the Huygens study area mimic those found elsewhere in the surrounding highlands but with a few notable additions. The olivine-HCP unit is the most widespread and associated with the morphologic plains units (intracrater, intercrater, intraring, and mottled), suggesting there may be no significant distinction between emplacement mechanisms of these units. LCP and isolated olivine exposures typically comprise erosionally resistant knobs, and are commonly embayed by olivine-HCP-bearing plains. Altered outcrops also usually occur within older terrain, as ejecta or in the rims and/or central peaks of younger craters. Notably, there is a lack of altered or LCP outcrops within the peak ring of Huygens, suggesting that either the mafic plains here are too thick for subsequent impacts to pen-

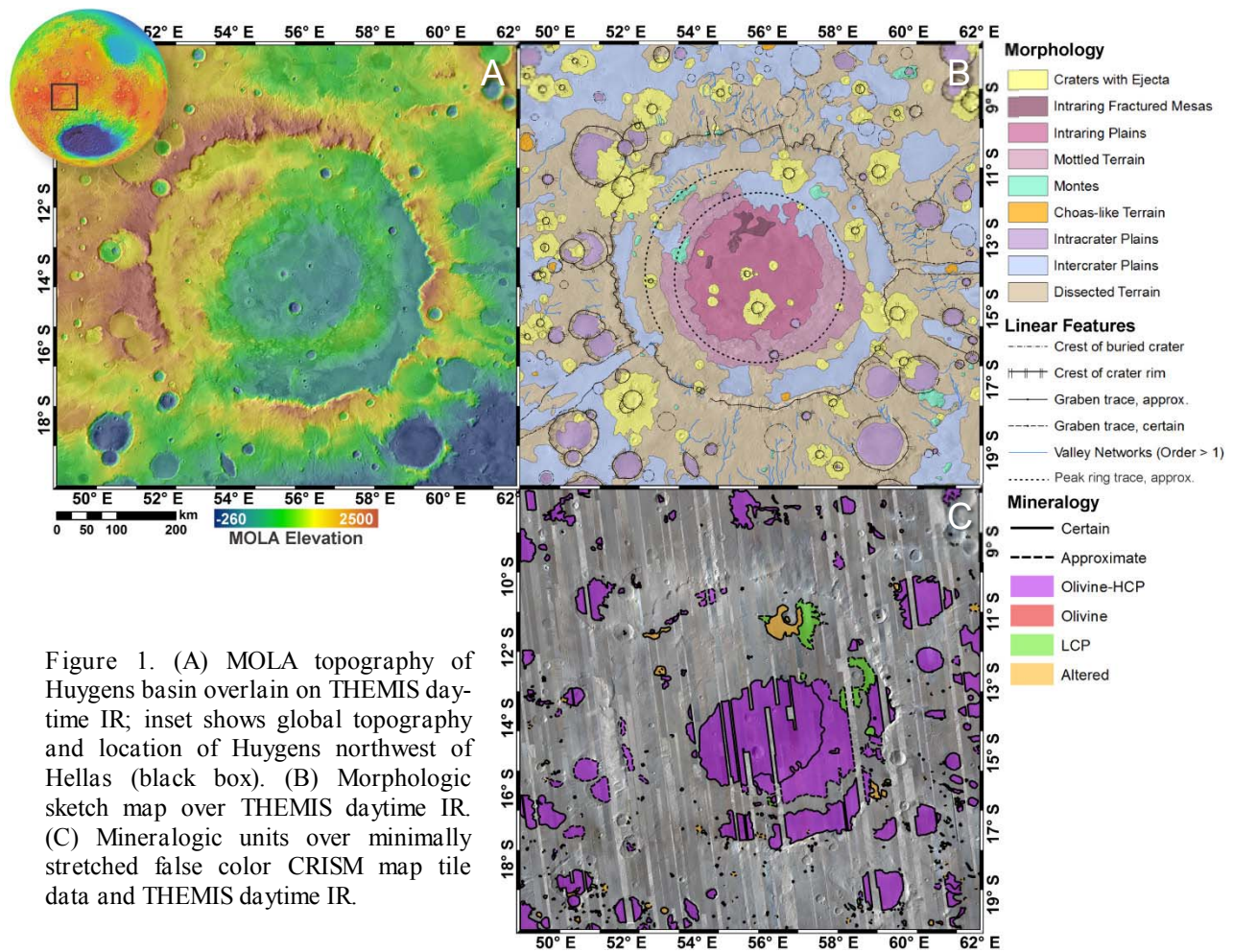


Figure 1. (A) MOLA topography of Huygens basin overlain on THEMIS daytime IR; inset shows global topography and location of Huygens northwest of Hellas (black box). (B) Morphologic sketch map over THEMIS daytime IR. (C) Mineralogic units over minimally stretched false color CRISM map tile data and THEMIS daytime IR.

-erate through, or that the uplifted peak ring materials did not host these minerals to begin with. The latter would imply that LCP- and alteration-bearing materials are limited to the upper few 10's of km of highland crust and that no additional alteration occurred post-Huygens.

Summary: Huygens crater represents a unique probe of the Noachian crust in the Hellas rim region. We have identified four mineralogic units (olivine-HCP plains, olivine and LCP knobs, and aqueously altered materials) within a morphologic context. The superposition of the olivine-HCP-bearing plains on crater floors as well as within intercrater areas is consistent with emplacement after Huygens formation, whereas knob-forming olivine- and LCP-bearing outcrops may be evidence of widespread crustal uplift or ejecta associated with Hellas [18] prior to the Huygens impact. Phyllosilicates and other alteration materials are scattered throughout the study area, exposed via subsequent cratering. However, a lack of alteration minerals interior to the peak ring, in material sourced from depth, suggests that no substantial aqueous activity persisted beyond the Early Noachian, at least in this region.

Acknowledgements: This work was supported by the NASA Mars Data Analysis Program (NNX10AO25G) and in part by an appointment to the Postgraduate Research Participation Program at JHU/APL administered by the Oak Ridge Institute for Science and Education (ORISE) program.

References: [1] Koeppen, W. C., et al. (2008) JGR, 113, E05001. [2] Mustard, J. F., et al. (2005) Sci., 307, 1594-1597. [3] Rogers, D., et al. (2011) JGR, 116, E08005. [4] Bibring, J.-P., et al. (2005) Sci., 307, 1576-1581. [5] Loizeau, D., et al. (2012) Icarus, 219, 476-497. [6] Ehlmann, B. E., et al. (2011) Nature, 479, 53-60. [7] Murchie, S. L., et al. (2007) JGR, 112, E05S03. [8] Ferguson, R. L., et al. (2013) LPSC #1642. [9] Christensen, P. R., et al. (2013) LPSC #2822. [10] MOLA [11] Malin, M. C., et al. (2007) JGR, 112, E05S04. [12] McEwen, A. S., et al., (2007) JGR, 112, E05S02. [13] Seelos, F. P., et al., (2017) 3rd Plan. Data Workshop #7113. [14] Pelkey, S. M. et al. (2007) JGR, 112, E05S14. [15] Viviano-Beck, C. E., et al. (2014) JGR, 119, 1403-1431. [16] Seelos, F. P., et al. (2012), Planetary Data Workshop. [17] Hynek, B. M., et al. (2010) JGR, 115, E09008. [18] Skok, J. R., et al. (2012) JGR, 117, E00J18.

FINAL STAGES OF THE 1:24,000-SCALE GEOLOGIC MAPPING OF BASIN DEPOSITS EXPOSED IN HADRIACUS CAVI, MARS. J. A. Skinner, Jr. and C. M. Fortezzo, Astrogeology Science Center, U. S. Geological Survey, 2255 N. Gemini Dr., 86001 (jskinner@usgs.gov).

Regional Setting: The Martian cratered highlands are generally assumed to be composed of variously intercalated units, including impact breccia, flood lavas, pyroclastic units, and eolian, fluvial, and lacustrine sediments. However, identifying these units is complicated by the limited vertical exposure of these rocks on the Martian surface and the inherent difficulty in observing lithologic characteristics via orbital data. We are finalizing a 1:24,000-scale geologic map of strata exposed along the northeastern margin of an ancient, 2300-km diameter impact basin (Hellas Planitia), located in the Martian cratered highlands. Hadriacus Cavi are a 65 km long, 15 km wide set of east-west oriented scarp-bounded depressions bordered on the south by topographic promontories interpreted as basin-related crustal massifs and on the north by Hadriacus Palus, a nearly horizontal alluvial plain. Model absolute ages indicate the surrounding highland plains were emplaced $\sim 4.1 \pm 0.1$ Ga and subsequently resurfaced $\sim 3.4 \pm 0.2$ Ga, the latter which corresponds to the age of Hadriacus Palus (3.4 ± 0.1 Ga). Small area counts within the cavi yield ages of 3.8 ± 0.2 Ga. Our map focuses on a >500 meters-thick section of strata exposed in central Hadriacus Cavi that extends south from Hadriacus Palus.

Datasets and Methods: Our mapping, descriptions, and analyses were based on a digital terrain model (DTM) (clone=78.04°E, 1.5 m/px) and associated orthoimages (0.5 m/px) generated from a HiRISE stereo-pair. Base data were supplemented by HiRISE gray-scale images (registered to DTM-derived orthoimages) and CTX image mosaics to help link local observations to surrounding terrains and assist with unit identification and description. Data were displayed and mapping completed in Esri's ArcGIS software. We identified, described, and subdivided local strata based on dominant grayscale tone, texture, and lateral continuity as observed in the base data (Fig. 1). Three unit groups form the volumetric bulk of Hadriacus Cavi and one group constitutes the strata of southern Hadriacus Palus. Throughout, light-toned strata form steep ($>40^\circ$) slopes and scarps, implying increased erosional resistance compared to intervening dark-toned strata, which form shallower slopes and source pervasively-occurring surficial cover. We identify no widespread angular unconformities within or between any of the mapped units, though discontinuities may exist. Lineaments, interpreted as near-vertical joints and faults with minor offset, mapped

throughout the area, parallel E-W and NE-SW regional trends.

Mapping Results: We mapped four groups of stratified units in Hadriacus Cavi. The basal group is topographically and stratigraphically the lowest group in the study region, and crops out between -2492 and -2838 m elevation. It consists of mostly massive, dark-toned material that is subdivided by three widespread light-toned, <10 -meter thick, scarp-forming layers. The bulk of the basal group is slope-forming, heavily obscured by dark-toned colluvium and dunes, and has a paucity of internal textures or features at orthoimage resolution. Basal group strata dip $2-4^\circ$ to the west with no obvious trend in variation. The cavi group superposes the basal group, forms the upper walls of the canyons in the study area, and crops out between -2185 and -2812 m elevation. This group contains a lowermost unit of non-interlocking, meter-scale angular blocks capped by ~ 10 -meter tall columnar joints (appearing as hexagonal polygons on horizontal surfaces), a light-toned, mostly massive unit containing asymmetrical lenses with flat tops and parabolic bottoms, and an uppermost unit characterized by rhythmic sequences of light- and dark-toned strata that forms a reference surface occurring throughout the map region. The cavi group forms scarps and slopes, and dips $\sim 4-6^\circ$ to the northwest. The mons group forms and crops out at the margins of irregularly-shaped hills located above the cavi group reference surface, and crops out between -2117 and -2505 m elevation. This group includes mostly massive, light-toned units that often contain meter-scale angular blocks, and forms continuous steep slopes with intermittent scarps and infrequent meters-thick, dark-toned strata. Though discrete meter-scale layers are locally apparent in this group, they are not as consistently traceable as other unit groups. Mons group strata show an average dip of 3° to the northwest, though dip direction of strata vary significantly without any obvious spatial trend. The palus group crops out in the northern part of the map area along the topographic scarp separating Hadriacus Palus from Hadriacus Cavi, and crops out between -2640 and -2802 m elevation. It consists of a lowermost, light-toned stratified to massive unit, a light-toned unit composed of meter-to decameter-scale fracture-bound blocks, and an uppermost light- and dark-toned stratified unit. Palus group strata show an average dip of $1-3^\circ$ to the south, though layers in lower sections show slight north dip.

Discussion: Mapping reveals a series of predominantly conformable, massive to stratified, variably-toned rock units that exhibit a range of geomorphic textures, suggesting an active and perhaps rapidly-changing volcanic and intermittent fluvial history during the earliest periods of Mars' evolution. We interpret the geologic units mapped in central Hadriacus Cavi as a nearly continuous record of deposition in Hellas impact-formed annular topographic basins. Though massif-related units do not occur in the map region, lateral continuity of mapped units into abutting areas of Hadriacus Cavi demonstrates these units superpose bounding promontories. A slight northward

dip of the basal, cavi, and mons groups implies south to north deposition. E-W trending sets of near vertical fractures and joints transect all of these unit groups, indicating post-depositional faulting deformed all accumulated strata into broad, monocline like structures. Faulting may be related to reactivation of Hellas-related crustal faults. The palus group is generally distinct in morphology and orientation from other mapped groups. This group superposes – and possibly interfingers – all other units in the map region. All mapped groups were deposited prior to exhumation and exposure of strata to form the current cavi depressions.

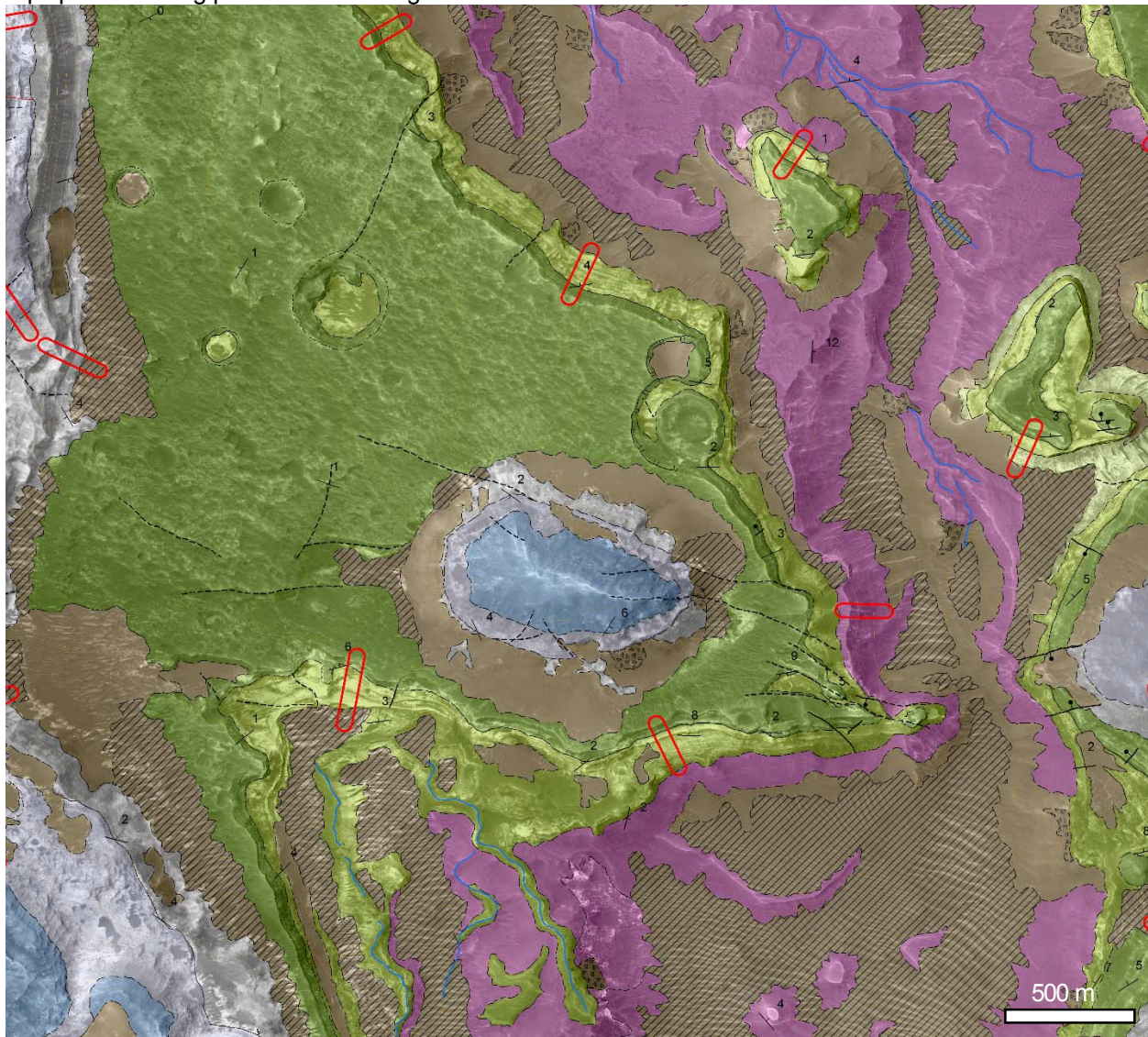


Figure 1. Excerpt of the 1:24,000-scale geologic map of central Hadriacus Cavi, Mars, showing ~230 meters of strata within the canyon system. Purple=basal group. Green=Cavi group. Blue=Mons group. Dunes, non-duneform sands, and talus are shown in brown with stipple patterns. Red boxes show locations of compiled vertical sections. Mapped lines show locations of near vertical joints, some with meter-scale offset, which forms a broad monocline structure.

GEOLOGIC MAPPING AT 1:60K SCALE OF WESTERN AEOLIS MONS, GALE CRATER. B. J. Thomson¹, D. L. Buczkowski², L. S. Crumpler³, and K. D. Seelos², ¹Department of Earth and Planetary Sciences, University of Tennessee, Knoxville, TN (bthom@utk.edu), ²Johns Hopkins University Applied Physics Lab, Laurel, MD, ³New Mexico Museum of Natural History & Science, Albuquerque, NM.

Introduction: This report encapsulates progress on the creation of a 1:60,000 scale map of the western portion of Aeolis Mons (informally known as Mt. Sharp) in Gale crater. The focus of this geologic mapping effort is to better understand the stratigraphy and mode of formation of unconformable units on Mt. Sharp. Progress has been made in two different areas. First, we have completed reconnaissance maps of our study area to delineate the major units and contacts present. Second, we have conducted a mass balance analysis of the sediment budget in Mt. Sharp to provide bounds as to how much of the central mound is attributable to fluvial and/or lacustrine processes.

Reconnaissance mapping: We have completed two reconnaissance geologic maps by PI Thomson and Co-I Crumpler. Co-I Buczkowski led the task of comparing and contrasting these two reconnaissance maps with a particular emphasis of areas where there is disagreement (Fig 1a). These areas have been targeted for further attention and analysis in subsequent mapping. As presented at the 2016 Annual Planetary Geologic Mappers Meeting [1], we also compared our reconnaissance maps to existing, published geologic maps [e.g., 2] (Fig. 1b).

Gale sediment balance: We have also submitted a manuscript to the journal *Geology* entitled "How much of the sediment in Gale crater's central mound was fluvially transported?" We are currently finalizing revisions to the three reviews received on the manuscript. This contribution measures the volume of material eroded by the contributing valley network into Gale crater and compares it with the volume of the mound itself, thus setting constraints on the proportion of the mound that could plausibly be attributed to fluvial transport processes. Figure 2 is an example figure from this publication and presents the results of some of our valley network measurements. A pre-print of this manuscript is available upon request.

Future work: The PI has recently moved from Boston University to the University of Tennessee Knoxville. Now that this project has been successfully transferred to UTK, work will renew upon completion of the final geologic map product. The current timeline is to submit it for USGS review in the fall of 2018.

References:

[1] Thomson B.J. et al. (2016) Planetary Geologic Mappers Meeting, abstract #7022. [2] Le Deit L. et al. (2013) *JGR*, 118, 2439-2473.

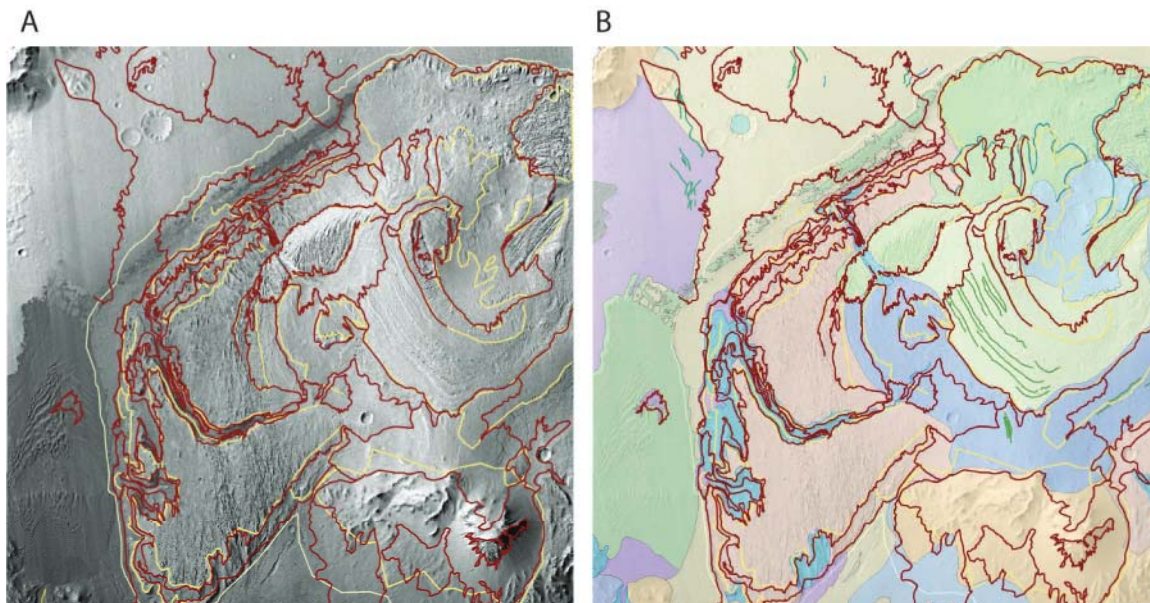


Figure 1. (a) CTX mosaic overlain with Crumpler (red) and Thomson (yellow) geologic contacts in reconnaissance mapping efforts. (b) Same contacts given in Fig. 1a overlying Gale geologic map from Le Deit et al. [2013].

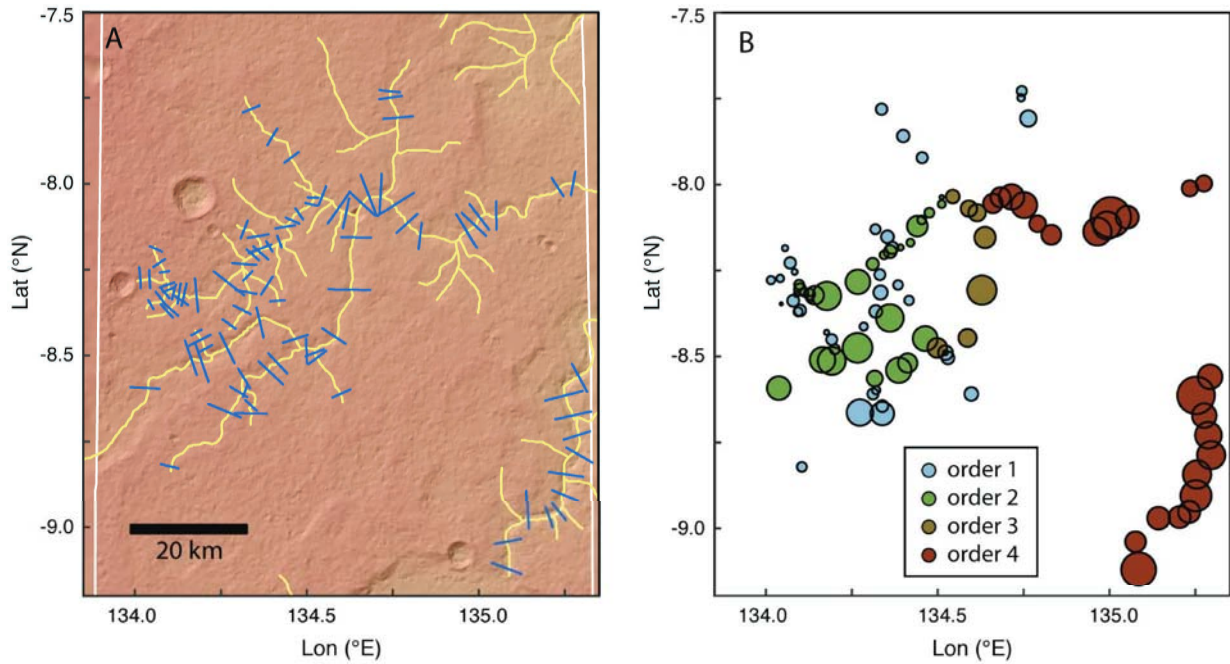


Figure 2. (a) Mapped valley networks with locations of cross-sectional profiles given with blue bars. (b) Locations of N=96 profiles from Fig. 2a with points colored according to Strahler stream order (1–4) and diameters sized according to relative cross-sectional area, i.e., larger 2D area.

NASA'S SOLAR SYSTEM TREKS IMAGE MOSAIC PIPELINE. M. R. Trautman¹, S. Malhotra¹, C. Nainan¹, R. M. Kim¹, B. X. Bui¹, S. Sadaqathullah¹, P. Sharma¹, N. Gallegos¹, E. S. Law¹, and B. H. Day², ¹Jet Propulsion Laboratory, California Institute of Technology, M/S 301-250D, 4800 Oak Grove Dr. Pasadena, CA, USA 91109 (marshall.r.trautman@jpl.nasa.gov), ²NASA Solar System Exploration Research Virtual Institute, NASA Ames Research Center, M/S 17-1, Moffett Field, CA, USA, 94035

Introduction: An unprecedented and growing number of high resolution orbital images of the Moon and Mars are available in the form of Narrow Angle Camera images from the Lunar Reconnaissance Orbiter as well as Context Camera (CTX) and High Resolution Imaging Science Experiment (HiRISE) images from the Mars Reconnaissance Orbiter. There are sufficient HiRISE, CTX, and NAC data coverage to produce a far greater number of high resolution image mosaics than are currently available to the planetary science community. This study details the efforts of the NASA Solar System Treks project to design a framework for automated systems capable of bridging this gap.

Solar System Treks Portals: NASA's Solar System Treks provide a growing number of online data and visualization portals for planetary scientists, engineers, mission planners, and educators. The portals enable the easy visualization and download of different map projected, georeferenced, and mosaiced datasets with full metadata.

There are currently three publicly available portals: Moon Trek (<https://moontrek.jpl.nasa.gov>), Mars Trek (<https://marstrek.jpl.nasa.gov>), and Vesta Trek (<https://vestatrek.jpl.nasa.gov>). A Titan Trek portal is planned for release in September 2018.

Image Mosaic Pipeline: The image mosaic pipeline consists of input selection, pre-processing, image registration, and mosaicing components (figure 1). For each type of data being processed, the procedures change depending on processing level of downloadable data, the instrument specific functions used for pre-processing in ISIS3, localization error (and requirements), and the relative tones/colors of the data.

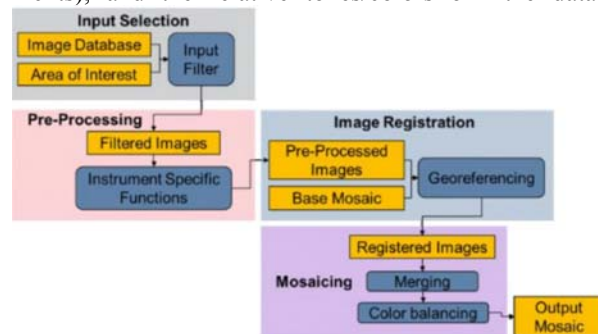


Figure 1: Diagram of Generalized Image Mosaic Pipeline

Three causes of seams were identified and addressed by the system: 1) seams due to significant differences in lighting, atmospheric conditions, or resolution, 2) seams from misaligned images due to poor registration, 3) seams from differences in tone/brightness/color between images. Each of these causes of seams are handled by input selection, image registration and color balancing, respectively.

Input Selection: Input selection begins with inspection of data product footprints from the PDS Geoscience Node at Washington University in St. Louis (<http://ode.rsl.wustl.edu>) in a desktop GIS client. This allows for many different images to be quickly filtered without the time cost of inspecting map-projected images.

Spatial Selection. The first step of filtering inputs is to determine which datasets are available in the area of interest with a spatial query. If there are numerous overlapping images available, they are then filtered down based on lighting condition attributes.

Attribute Selection. After images are selected, the season, acquisition time, phase, emission, incidence angles are taken into consideration for choosing which combinations of inputs will have the least differences in lighting condition. This is especially the case for NAC images and Polar CTX/HiRISE images.

Visual Inspection. The last step of input selection is to visually inspect each image for noise, and image artifacts. In the case of Mars, images must be inspected for haziness due to atmospheric condition.

Pre-Processing: Images are automatically processed in parallel using python, shell, and ISIS3. The general procedure entails downloading images from PDS, importing to ISIS3, attaching SPICE kernel information, calibrating and correcting with instrument specific functions, and map projecting.

Image Registration: Level 2 and Level 3 images are inspected for offset and georeferenced if necessary. For CTX and HiRISE (which are almost always offset), the automated georeferencing software Mars_Nest [1] is used to control HiRISE images to CTX, and CTX images to HRSC, MDIM2.1, or THEMIS Day IR depending on coverage.

Mosaicing: After images are satisfactorily processed and registered, they are merged together and color balanced if necessary. The current method of choice is Distributed Gradient-Domain processing [2].

Meta Data Ingestion: As products are created, metadata compliant with Federal Geographic Data Consortium (FGDC) standards are generated and updated to accompany the product.

Conclusions: The pipeline described in this study represents a generalized approach for creating image mosaics intended to be applicable as more high resolution orbital data become available. Future work includes developing more streamlined and consistent automations between components, investigating image metrics that can be used for automated input quality control, and incorporating block adjustment techniques.

References: [1] Logan T. L. et al. (2018) *LPS XLIX*, Abstract #1178. [2] Kazhdan M. (2010) *ACM Transactions on Graphics*, 29, 14:1-14:11.

GEOLOGIC MAPPING AND STUDIES OF DIVERSE DEPOSITS AT NOCTIS LABYRINTHUS, MARS. Catherine M. Weitz¹, Dan Berman¹, Alexis Rodriguez¹, and Janice L. Bishop², ¹Planetary Science Institute, 1700 E Fort Lowell, Suite 106, Tucson, AZ 85719 (weitz@psi.edu); ²SETI Institute, 189 Bernardo Ave., Mountain View, CA 94043.

Introduction: Noctis Labyrinthus consists of a network of intersecting linear troughs and pits along the eastern Tharsis rise that connect eastward to the continuous chasmata of Valles Marineris. The pits and troughs may have formed due to withdrawal of magmatic reservoirs at depth [1], or by collapse over conduits developed by tectonically controlled groundwater flow [2]. The age of Noctis Labyrinthus is thought to be Late Hesperian to Early Amazonian based upon disruption of the lava plains along the plateaus [3-5]. Consequently, sediments deposited within the depressions represent this age or younger materials.

Mapping Investigation: For this study, we are mapping the western portion of Noctis Labyrinthus (-6 to -14°N, -99.5 to -95.0°W; Fig. 1), which includes some of the most diverse mineralogies identified on Mars using CRISM data [6-9]. We are using THEMIS daytime IR as a basemap, with a 1:500,000 publication scale. Thus far across the Noctis Labyrinthus region, the following minerals have been identified in association with light-toned deposits (LTDs): several kinds of sulfates (monohydrated {kieserite, szomolnokite} and polyhydrated sulfates, jarosite, and Ca-sulfates {gypsum, basanite}), clays {Fe/Mg-phyllsilicates and Al-phyllsilicates}, a doublet absorption between 2.2-2.3 μm , and hydrated silica/opal. The role of water, both in the formation of the Noctis depressions and the hydrated deposits found within them, is a focus of this investigation. The diverse range of sulfates and phyllosilicates within the depressions of Noctis Labyrinthus likely resulted from localized aqueous activity [8,9], and may have been part of a broader synoptically driven period of late activity during the Late Hesperian to Amazonian [e.g., 10-12].

Constraints from geologic mapping and morphologic and stratigraphic analyses will be key contributions toward deciphering the geologic diversity and history of this portion of Noctis Labyrinthus, with specific implications regarding the role and history of water. In particular, the timing, duration, nature, and spatial extent of the influence of water-related processes in the region is a focus on this study. An understanding of the history of deformation and collapse within this region will also be key to deciphering the timing of sedimentary deposition and aqueous alteration.

Mapping Progress: We have completed mapping of all geologic units and linear features (Fig. 1). Numerous structural features, including grabens and fault scarps, are found throughout the mapping region.

Mapping of normal faults and grabens indicates multiple episodes of collapse.

Eolian debris and dust cover much of the plateau, trough floors, and wallrock, obscuring geologic contacts between different units at these locations. The dust mantle thins to the east and south, where individual lava flows are evident along the plateau. Two volcanic shields have been mapped in the southwestern plateau and both are embayed by younger lava flows. Beneath the plateau plains unit is the gullied and layered wallrock unit, which is similar in morphology to the layered gullied upper wallrock observed throughout Valles Marineris. Light-toned deposits occur in only one location along the plateau and they are only visible as small patches because a dark mantle and eolian ripples cover much of the plateau, including the light-toned deposits, in this region. CRISM spectra show the presence of opal in association with these plateau deposits.

Floor units within the troughs and pits include light-toned deposits, many of which also exhibit spectral hydration features, and mass wasting deposits, including landslides. Lava flows with Amazonian ages [13] have been mapped on two trough floors. Floor morphology can either be smooth or rough, with the rough morphology from collapsed materials and the smooth morphology typically the result of eolian fill. No fluvial channels have yet been identified either along the plateau or within the depressions, but a possible volcanic channel sourced by a collapsed rounded depression within one of the troughs indicates younger volcanism occurring after formation of the trough. Dark dunes have been mapped in two troughs.

The light-toned deposits observed within the pits and troughs can be one homogeneous bed or numerous layers with variable lithologies (e.g., brightness, fracturing, and lithification differences). Where CRISM data is available, the layered deposits display a wide range of mineralogies, indicating a complex aqueous history within this region. Topographic profiles reveal that the light-toned deposits within the pits and troughs all occur below 4 km in elevation, consistent with hydrologic resurfacing by water sourced from aquifers beneath the Tharsis rise [2].

References: [1] Mege D. et al. (2003) *J. Geophys. Res.*, 108(E5), doi:10.1029/2002JE001852; [2] Rodriguez, J.A.P. et al. (2016) *Planetary and Space Science*, 124, 1-14. [3] Tanaka K.L. and P.A. Davis (1988) *J. Geophys. Res.* 93, 14893-14917; [4] Witbeck et al.,

(1991) USGS Map I-2010, scale 1:2,000,000; [5] Tanaka K.L. et al. (2014) Geologic Map of Mars, USGS Map 3292; [6] Weitz C.M. and J.L. Bishop (2014) Mars 8th Conference, Abstract 1222; [7] Weitz C.M. and J.L. Bishop (2013) Planet. Space Sci., doi:10.1016/j.pss.2013.08.007; [8] Weitz C.M. et al. (2011) Geology, 39:899-902, doi: 10.1130/G32045.1; [9] Thollot P. et al. (2012) J. Geophys. Res., 117,

E00J06, doi:10.1029/2011JE004028; [10] Moore J.M. and A.D. Howard (2005) J. Geophys. Res., 110, E04005, doi:10.1029/2005JE002352; [11] Fassett C.I. and J.W. Head (2008) Geophys. Res. Letts., 32, L14201, doi:10.1029/2005GL023456; [12] Grant J.A. and S.A. Wilson, (2011) Geophys. Res. Letts., 38, L08201, doi:10.1029/2011GL046844. [13] Mangold N. et al. (2009) Earth Planet.. Sci. Letts. 294, 440-450.

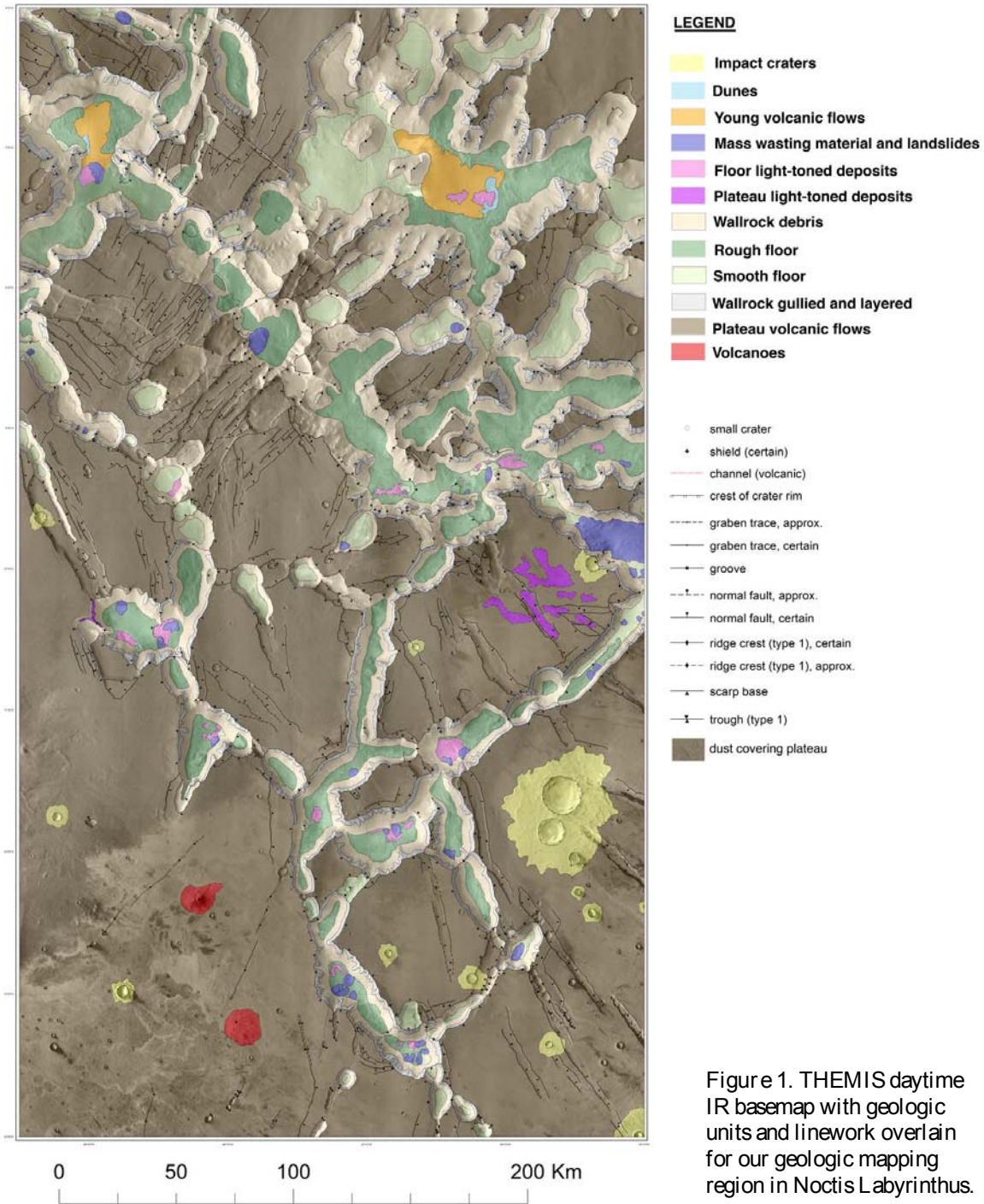


Figure 1. THEMIS daytime IR basemap with geologic units and linework overlain for our geologic mapping region in Noctis Labyrinthus.

GEOLOGIC MAP OF THE DERAIN (H-10) QUADRANGLE ON MERCURY: THE CHALLENGES OF CONSISTENTLY MAPPING THE INTERCRATER PLAINS UNIT. J. L. Whitten¹, C. I. Fassett², and L. R. Ostrach³, ¹Center for Earth and Planetary Studies, Smithsonian Institution, MRC 315, PO Box 37012, Washington, DC 20013 (whittenj@si.edu), ²NASA Marshall Space Flight Center, Huntsville, AL 35805 (caleb.i.fassett@nasa.gov), ³U.S. Geological Survey, Astrogeology Science Center, 2255 N. Gemini Dr., Flagstaff, AZ 86001 (lostrach@usgs.gov).

Introduction: Mercury is dominated by three major geologic units: crater materials (crater rim, ejecta, etc.), smooth plains, and intercrater plains [1, 2 and references therein]. Of these three geologic units, the intercrater plains cover the largest surface area on Mercury and are generally identified as gently rolling plains with a high density of superposed craters, especially small secondary craters <15 km in diameter [1]. The distribution and crater statistics indicate that the intercrater plains record an ancient resurfacing event [3, 4], which may have been caused by either volcanism or impact-related processes. Various formation mechanisms have been proposed for the intercrater plains, from volcanic events, to basin ejecta [1, 5–8].

Using the latest MErcury Surface, Space ENvironment, GEochemistry and Ranging (MESSENGER) datasets, several authors have proposed that the intercrater plains represent volcanic deposits that have been highly modified post-emplacment [e.g., 9, 10]. However, it is possible that a portion of the intercrater plains were formed via impact-related processes. There are several large smooth plains deposits, like the circum-Caloris and circum-Rembrandt plains [7, 11, 12], that have an uncertain origin. Perhaps these circum-basin plains represent a portion of the intercrater plains sourced from impact events, rather than volcanic activity. Mercury has a high average impact velocity (~42 km/s) [13] that would produce large volumes of melt during impact events.

Here, we discuss production of a 1:5M USGS map of the Derain (H-10) Quadrangle of Mercury to assess the importance of melt and other ejecta materials on resurfacing Mercury. This map was recently funded through the 2016 DDAP program and is in its first year. This H-10 region was not imaged by the Mariner 10 mission (Figure 1). Thus, this map will be the first USGS geologic map of the region. H-10 was selected for its “ordinary” character: it does not contain any recent impact basins, nor does it contain expansive smooth plains deposits. H-10 represents morphologically average Mercury crust, which enables a thorough analysis of the intercrater plains and their formation mechanisms.

Data: Image datasets collected during the MESSENGER mission will be used to produce the H-10 quadrangle map. The Mercury Dual Imaging System (MDIS) monochrome mosaic at 166 m/pixel will be the primary dataset used to delineate different geologic units at a map scale of 1:1.25M. Other image datasets that will be used to assist with unit definition include the MDIS color mosaic (665 m/pixel), and MDIS East and West Illumination mosaics (166 m/pixel). The H-10 quadrangle extends from 25°N to 25°S, and 288°W to 360°W (Figure 1).

In addition to using the image data, crater statistics will be calculated across the quadrangle to assist with defining geologic units. All craters >8 km in diameter will be mapped to determine the N(10) and N(20) areal

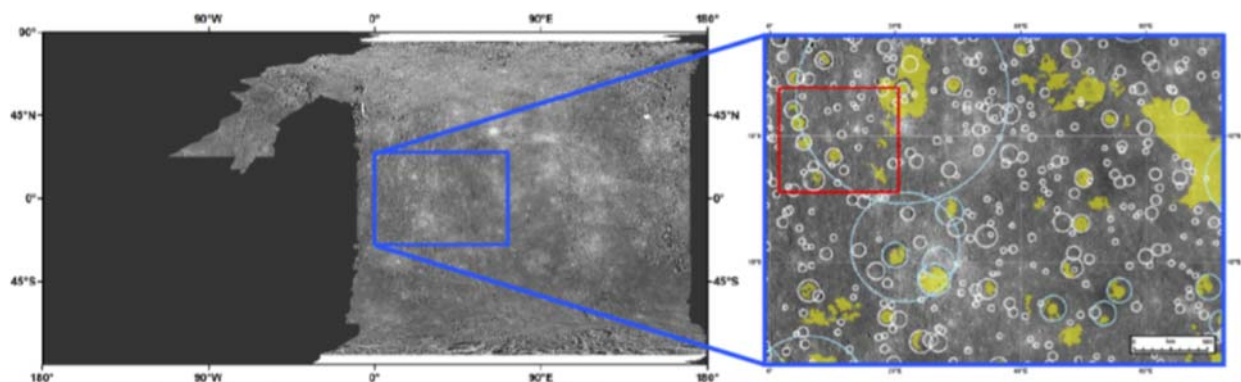


Figure 1. The Derain (H-10) quadrangle on Mercury. (Left) Blue box denotes the location of the H-10 quadrangle. The dark grey regions are the areas that were imaged by and have been mapped using the Mariner 10 dataset. (Right) Close view of the H-10 quadrangle, with the smooth plains mapped by [7] in yellow. Craters ≥ 30 km in diameter are shown in white and those > 150 km are also outlined in blue. Red box shows the location of the map sub-region (see Figure 2). MDIS monochrome (750 nm) 166 m/pixel global mosaic.

crater density values (the number of craters $>D$ per 10^6 km^2 [14]) and derive a relative stratigraphy for the different map units. Both the crater mapping and the geologic unit mapping builds on datasets compiled by previous studies [e.g., 7, 15].

Approach: The boundary of intercrater plains is difficult to define because the unit gradually transitions into smooth plains in many locations across Mercury. There are other locations on Mercury where smooth plains are hummocky to variable degrees. In Mariner 10 maps, an intermediate plains unit was used to delimit these more ambiguous regions. However, this definition of unit was not consistently applied across the surface and creates confusion surrounding plains units on Mercury. Researchers proposed to discontinue the use of this unit [10], which necessitates the clear definition of smooth and intercrater plains. To start, the least complicated materials are mapped first in H-10, which includes smooth plains and crater materials. After these units are mapped, then the remaining unmapped materials are assessed to determine how well they adhere to the morphologic definition of intercrater plains. Those that fit the standard definition of intercrater plains are mapped thus, and the remaining unmapped materials are further analyzed to determine the most fitting geologic unit.

Current progress: A subset of the H-10 quadrangle is being mapped by three members of the proposal team (L.R. Ostrach, C.I. Fassett, J.L. Whitten) (Figure 1 red box, Figure 2). This sub-region contains gradational boundaries between the smooth and intercrater plains, as well as gradational boundaries between relatively fresh crater ejecta materials (i.e., secondary crater fields) and intercrater plains. It is difficult to determine where the secondary crater field ends and where the background intercrater plains starts (Figure 3), especially given that this sub-region has five >100 km diameter craters in close proximity to one another that only further obscures the relative stratigraphy of the continuous ejecta deposits and secondary crater fields (Figure 3). Other datasets (MDIS color, MLA topography) will be integrated to help clarify geologic unit boundaries.

The color scheme used in the Mariner 10 USGS geologic maps is not diverse enough (i.e., there are many pinks and oranges) to enable quick visual assessment of the presented surface geology and deserves reanalysis and discussion. We propose to develop a consistent color scheme at this Planetary Geologic Mappers Meeting that could be used by ongoing and future researchers producing new geologic maps of Mercury.

References: [1] Trask N. J. & Guest J. E. (1975) JGR, 80, 2461–2477. [2] Frigeri A. et al. (2009) LPS XXXX, Abstract #2417. [3] Fassett C. I. et al. (2011)

GRL, 38, L10202. [4] Marchi S. et al. (2013) Nature, 499, 59–61. [5] Strom R. G. et al. (1975) JGR, 80, 2478–2507. [6] Head J. W. et al. (2011) Science, 333, 1853–1856. [7] Denevi B. W. et al. (2013) JGR, 118. [8] Oberbeck V. R. et al., (1977) JGR, 82, 1681–1698. [9] Denevi B. W. et al., (2009) Science, 324, 613–618. [10] Whitten J. L. et al., (2014) Icarus, 241, 97–113. [11] Fassett C. I. et al. (2009) EPSL, 285, 297–308. [12] Whitten J. L. & Head J. W. (2015) Icarus, 258, 350–365. [13] LeFeuvre M. & Wieczorek M. A. (2008) Icarus, 197, 291–306. [14] Crater Analysis Techniques Working Group (1979) Icarus, 37, 467–474. [15] Herrick R.R. et al. (2011) Icarus, 215, 452–454.

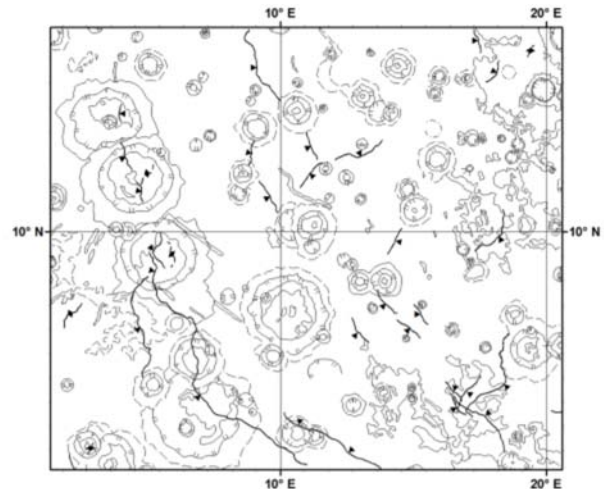


Figure 2. In progress geologic map of the sub-region of H-10 noted in red in Figure 1 (right). Linear features, such as lobate scarps (lines with triangles), have been mapped in addition to crater materials and smooth plains.

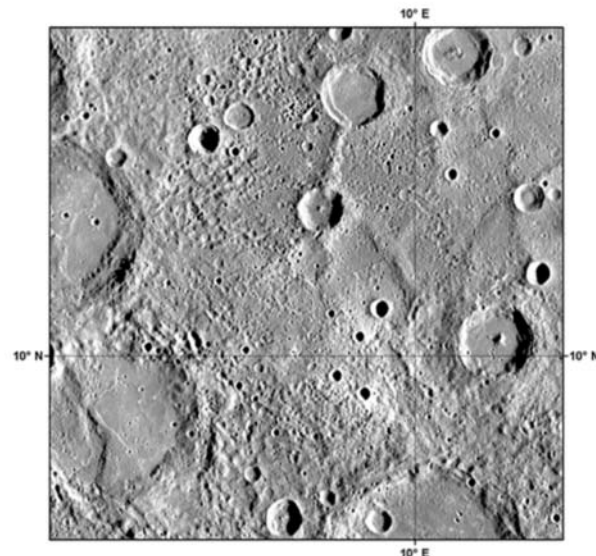


Figure 3. View of the overlapping ejecta deposits associated with four of the five >100 km diameter craters in the H-10 sub-region. This region is in the upper left part of Figure 2. MDIS monochrome (750 nm) 166 m/pixel global mosaic.

HIGH-RESOLUTION GLOBAL GEOLOGIC MAP OF CERES FROM NASA DAWN MISSION. D.A. Williams¹, D.L. Buczkowski², D.A. Crown³, A. Frigeri⁴, K. Hughson⁵, T. Kneissl⁶, K. Krohn⁷, S.C. Mest³, J.H. Pasckert⁸, T. Platz⁹, O. Ruesch¹⁰, F. Schulzeck⁷, J.E.C. Scully¹¹, H.G. Sizemore³, A. Nass⁷, R. Jaumann⁷, C.A. Raymond¹¹, C.T. Russell⁵. ¹School of Earth and Space Exploration, Arizona State University, Box 871404, Tempe, AZ 85287 (David.Williams@asu.edu); ²Johns Hopkins University Applied Physics Laboratory, Laurel, MD; ³Planetary Science Institute, Tucson, AZ; ⁴National Institute for Astrophysics, Rome, Italy; ⁵UCLA, Los Angeles, CA; ⁶Formerly at Freie Universität, Berlin, Germany; ⁷German Aerospace Center (DLR), Berlin, Germany; ⁸University of Münster, Münster, Germany; ⁹MPI for Solar System Research, Goettingen, Germany; ¹⁰ESA-ESTEC, Noordwijk, The Netherlands; ¹¹Jet Propulsion Laboratory, California Institute of Technology, Pasadena, CA.

Introduction: The science team from NASA's Dawn mission has completed a geologic mapping campaign for dwarf planet (1) Ceres. The purpose of this abstract is to serve as a citable source for our high resolution geologic map of Ceres derived from Low Altitude Mapping Orbit (LAMO) images (Figure 1) until a USGS-publishable global map can be completed. The lower-resolution, HAMO-based global geologic map and Ceres chronostratigraphy is discussed in Mest et al. [1].

Ceres Mapping Campaign: The geologic mapping campaign for Ceres using Dawn Framing Camera images is described in [2]. In summary, we conducted an iterative mapping campaign using images with increasing spatial resolution from Dawn's Survey orbit, High Altitude Mapping Orbit (HAMO), and LAMO. The first Survey map was published in Science [3]. The HAMO map with the chronostratigraphy and geologic timescale for Ceres is currently in review. The 15 individual LAMO quadrangle geologic maps of Ceres are published online and will be in a special issue of Icarus coming later in 2018 [4-17].

The objectives for geologic mapping using the LAMO mosaics were to investigate geologic features/topics identified from the global mapping in more detail and to refine the geologic history. As discussed in [2], there were challenges with this approach, most significantly coordination of 14 individual mappers and their mapping styles and objectives relative to efforts by other Dawn Science Team members. In the end, for the final published maps and mapping papers, individual quadrangles were combined when needed based on the distributions and extents of geologic units and features on the cerean surface. For example, the Urvara and Yalode quadrangle maps were combined because of the proximity of these two large basins and overlap of their deposits and structures [16]. In all, eleven papers are being published that discuss important cerean geologic features and processes, including the north polar cratered terrain and Yamor Mons [4]; the smooth impact melt-like deposits in Ikapati crater in Coniraya quadrangle [5]; the complex crater materials in Dantu crater [6]; water ice-based lobate flows in Ezinu quadrangle [7]; six possibly cryovol-

canic tholi (domes) in Fejokoo quadrangle [8]; the bright rayed and complex ejecta materials of Haulani crater [9]; the nature of the smooth material around Kerwan, Ceres' oldest impact basin [10]; the diversity of old cratered terrain in Nawish quadrangle [11]; the nature of floor fractures in craters in Occator quadrangle [12]; the interplay of cryovolcanic domes (e.g., Ahuna Mons), Yalode and Haulani ejecta in Rongo quadrangle [13]; the complex stratigraphy of crater materials in the adjacent large basins Urvara and Yalode [15]; and the wide diversity of crater morphologies found in the Sintana, Toharu, and Zadeni quadrangles [14, 16, 17]. These eleven papers along with an introductory paper discussing the Ceres mapping campaign can be accessed at links below, and will be published in an upcoming 2018 special issue of Icarus.

References: [1] Mest S.C. et al. (2018), *49 Lunar Planet. Sci. Conf.*, Abstract #2730, Lunar and Planetary Institute, Houston. [2] Williams D.A. et al. (2018) Icarus, <https://doi.org/10.1016/j.icarus.2017.05.004>. [3] Buczkowski D.L. et al. (2016) Science, 353, <http://dx.doi.org/10.1126/science.aaf4332>. [4] Ruesch O. et al. (2018) Icarus, <https://doi.org/10.1016/j.icarus.2017.09.036>. [5] Pasckert J.H. et al. (2018) Icarus, <https://doi.org/10.1016/j.icarus.2017.06.015>. [6] Kneissl T. et al. (2016) 47th LPSC, Abstract #1967. [7] Scully J.E.C. et al. (2018) Icarus, <https://doi.org/10.1016/j.icarus.2017.10.038>. [8] Hughson K.H.G. et al. (2018) Icarus, <https://doi.org/10.1016/j.icarus.2017.09.035>. [9] Krohn K. et al. (2018) Icarus, <https://doi.org/10.1016/j.icarus.2017.09.014>. [10] Williams D.A. et al. (2018) Icarus, <https://doi.org/10.1016/j.icarus.2017.08.015>. [11] Frigeri, A. et al. (2018) Icarus, in revision. [12] Buczkowski D.L. et al. (2018) Icarus, <https://doi.org/10.1016/j.icarus.2017.05.025>. [13] Platz T. et al. (2018) Icarus, <https://doi.org/10.1016/j.icarus.2017.08.001>. [14] Schulzeck F. et al. (2018) Icarus, <https://doi.org/10.1016/j.icarus.2017.12.007>. [15] Mest S.C. et al. (2016) 47th LPSC, Abstract #1561. [16] Crown D.A. et al. (2018) Icarus,

<https://doi.org/10.1016/j.icarus.2017.08.004>. [17] Platz T. et al. (2016) 47th LPSC, Abstract #2595.

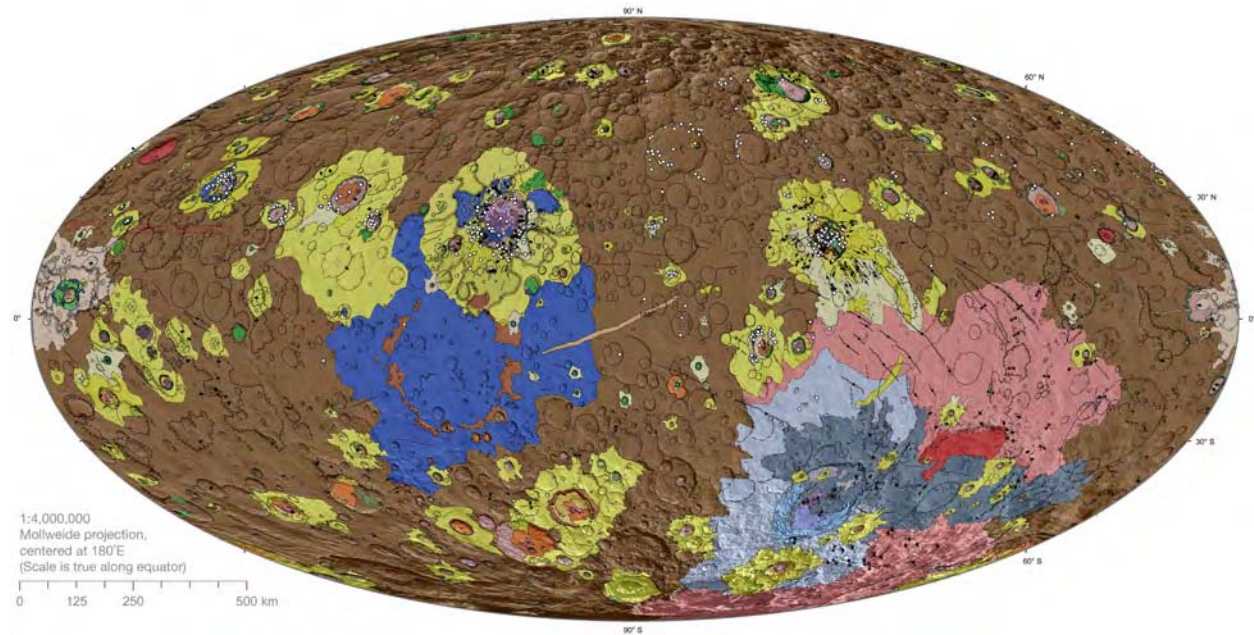


Figure 1a. Draft LAMO-derived global geologic map of dwarf planet (1) Ceres (1:4,000,000, Mollweide projection, center long. = 180°, IAU-approved Dawn Kait coord. system). This map was produced using ArcGIS™ software through integration of 15 individual quadrangle maps produced by the coauthors. GIS and cartographic issues, as well as the shown figures are supported by Andrea Nass, DLR. For citation of the Dawn Ceres LAMO-based map, please use this abstract. For a poster-sized version of the final map, please contact David Williams (David.Williams@asu.edu).

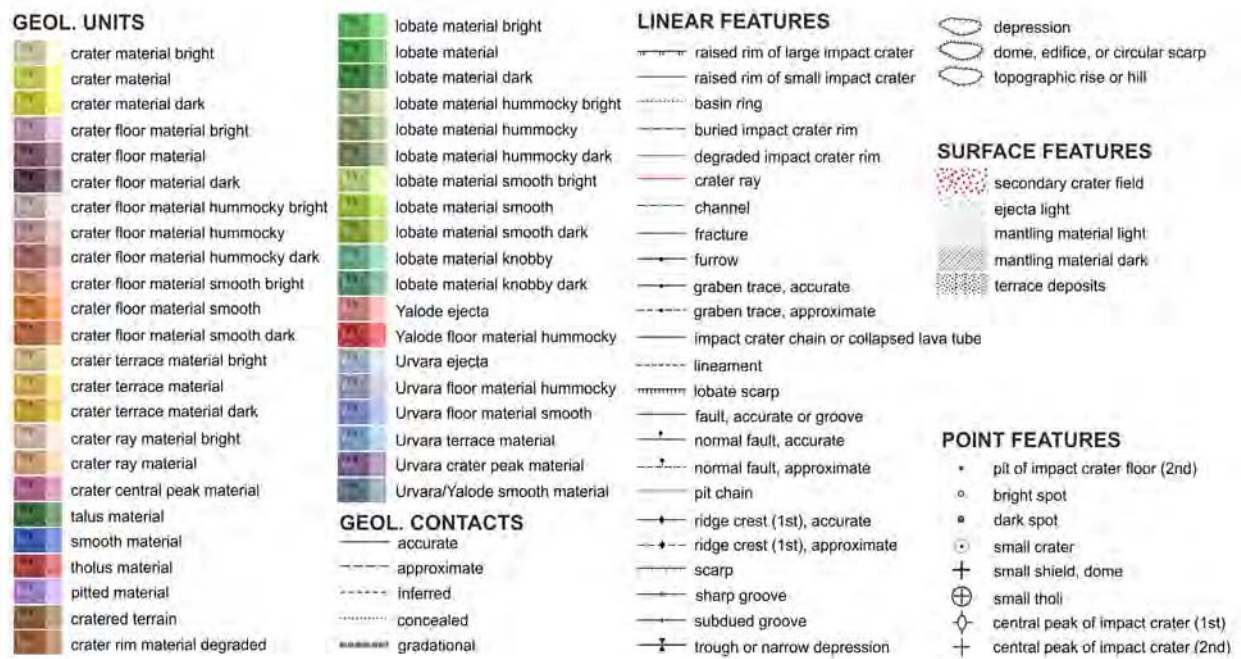


Figure 1b. Legend for Ceres unified LAMO geologic map. After [2].

HIGH-RESOLUTION GEOLOGIC MAPPING OF MARTIAN TERRACED FAN DEPOSITS. Jeannette M. Wolak, Amber B. Patterson, Shelby D. Smith, and Natalie N. Robbins, Department of Earth Sciences, Tennessee Tech University, 1 William L. Jones Drive, Cookeville, TN, 38505; jwolak@tntech.edu.

Introduction: Terraced fans are a subset of unique fan-shaped features documented on the Martian surface. Unlike other point-source geomorphic terrains—e.g. alluvial fans and deltas—terraced fans are characterized by concentric, stepped topography without clear terrestrial analogs. In general, these features tend to be small with diameters less than 10 km and concave-up profiles that alternate between steep and shallow slopes. Less than two dozen terraced fans have been identified, and all of them occur in late Noachian to early Hesperian geologic units [1]. Thus, terraced fans may provide a temporally-constrained geomorphic record of the evolution from hydrospheric-dominated processes to cryospheric-dominated processes.

The primary goal of this project is to use high-resolution geologic mapping to test competing hypotheses proposed for terraced fan formation. These hypotheses range from fluid-poor models to fluid-rich models and include: (1) mass movements [2]; (2) dense, low turbulence flows [3]; (3) sustained flows [4, 5]; and (4) periglacial or glacial processes [3, 4]. Most recently, workers have posited that fan terracing may record erosional processes not linked to deposition [6]. To determine which of these scenarios is most plausible, we will investigate the sedimentological processes responsible for terracing and map small-scale geomorphic features including boulders, incised valleys, small distributary systems, narrow levees, and barforms.

Study Locations: We have identified two terraced fans with exemplary datasets to support high-resolution mapping efforts. Both systems have adequate Context Camera (CTX) coverage and high-resolution stereo pair imagery from the High-Resolution Science Experiment (HiRISE). The first fan is located in an unnamed crater at 6.50°S and 141.14°E, approximately 250 km east-southeast of Gale Crater in the Aeolis Mensae region. Regional geologic mapping places this fan in the Hesperian-Noachian transition (HNt) unit, a formation located along the Martian hemispherical dichotomy [1]. The fan is asymmetrical in map view and characterized by older lobate terraces that fan out to the east and younger terraces that fan to the north (left image, Figure 1). The source of the fan sediments is a feeder canyon oriented roughly north-south; changes in terrace orientation are interpreted as back-stepping or filling of the open canyon topography.

To complement our study of the Aeolis Mensae system, we are also mapping an idealized terraced fan located at 11.73°N and 307.07°E (right image, Figure 1).

In terms of geologic setting, this system is located at the distal end of Subur Vallis in Xanthe Terra, a Noachian highland terrain that has been eroded by younger valley systems [5]. While the former study location is directly adjacent to the hemispherical dichotomy boundary, the latter is positioned approximately 350-500 km south of the transition from southern highlands to northern lowlands. We speculate that depositional processes responsible for these two systems may be similar, and we aim to determine the role of fluids in each area during fan formation.

Geologic Mapping: Our first task is generating HiRISE digital terrain models (DTMs) over the two targeted fans. To date, we have used the NASA Ames Stereo Pipeline and methodology outline in [7]; however, we plan a comparison of DTMs generated via this workflow with DTMs created using Bae System's SOCET SET software and methodology available at [8]. The goal of DTM production is two-fold and includes: (1) creating models on which we can take morphometric measurements; and (2) creating high-resolution orthoimages for use as base map(s).

Concurrently, we are mapping the two study areas at a scale of 1:18k, similar to recent high-resolution geologic mapping efforts over structurally complex regions in Candor Chasma [9]. All mapping is done digitally in ArcGIS at a consistent scale of 1:4k, approximately four times the proposed map publication scale. Vertex spacing is 4 m, and map units are defined based on tone, visual characteristics, terrain roughness, presence or absence of boulders, and stratigraphic context. Our initial results show a general stratigraphy common to both terraced fan systems that includes, from youngest to oldest: (1) aeolian deposits; (2) feeder channel and proximal (upper) fan terraces; (3) distal (lower) fan terraces; and (4) crater floor and wall terrains.

Aeolian Deposits. Like most fan-shaped features on Mars, the surfaces of terraced fans appear strikingly smooth except for post-depositional aeolian structures such as ripples and dunes. In the two study areas, aeolian deposits are especially common in topographically sheltered areas; for example, in broad-based feeder channels and the lee side of steep terraces. Thus, although aeolian deposits mask deeper stratigraphy, they are useful tools to characterize young wind-driven processes and define topographically shielded zones.

Feeder Channel and Proximal Fan Terraces. In both of the study areas, feeder channels breach steep crater walls and surfaces of the channel are assumed to grade from disconformities updip (erosion) to

progressively conformable contacts downdip (deposition). The uppermost terrace surfaces are generally smooth; however, the Subur Vallis system is characterized by multiple, sinuous incised channels [10]. Terraces appear to onlap older surfaces; however, without DTM data it is impossible to determine if these are progradational or aggradational features, i.e., clinoforms or horizontal surfaces, respectively.

Distal Fan Terraces. A marked change in slope occurs from steep proximal fan terraces to gently sloping distal fan terraces. In general, these units cover a much broader aerial extent than proximal terraces and tend to be smooth, light-colored, planar features that cover underlying rugged topography of the crater floor. In places, distal fan terraces 'fill in' gaps between older topographic highs along the edge of the crater.

Crater Floor and Wall Terrains. The oldest mappable units in both regions are exposed in the rugged topography along crater walls. These areas are distinguished by dark, craggy slope deposits with many boulders. Within the crater, smooth fan surfaces onlap the older crater floor which shows evidence of many small impacts and aeolian erosion.

Future Work: The next step in this project is to determine which of the two study locations provides the

most compelling evidence to distinguish between fluid-poor and fluid-rich formative processes. Over the next three years, we will generate a 1:18k Scientific Investigation Map (SIM) of a terraced fan system. Currently, we prioritize our work in the Aeolis Mensae region because it has more extensive HiRISE coverage and is located less than 250 km from the Mars Science Laboratory Rover in Gale Crater. We note that full-scale integration of these two datasets, i.e. resolving the stratigraphy using rover and orbital data, is beyond the scope of this project; however, it may prove to be an exciting follow-up given that workers recently documented a small terraced fan on Gale Crater's western escarpment [11].

References: [1] Tanaka et al. (2014) USGS SIM 3292. [2] Malin and Edgett (2003) *Science*, 302, 1931-1934. [3] Ori et al. (2000), *JGR: Planets*, 105, 17629-17641. [4] Weitz et al. (2006), *Icarus*, 184, 436-451. [5] Hauber et al. (2009), *PSS*, 57, 944-957. [6] Grindrod et al. (2017) *Icarus*, 1-21. [7] Mayer and Kite (2016), *LPSC 47*, Abstract 1241. [8] Kirk et al. (2008), *JGR*, 113, E00A24. [9] Okubo (2014) USGS SIM 3309. [10] Wolak and Patterson (2018), *SE GSA Abstract*, 50, 1p. [11] Palucis et al. (2016), *JGR: Planets*, 119, 705-728.

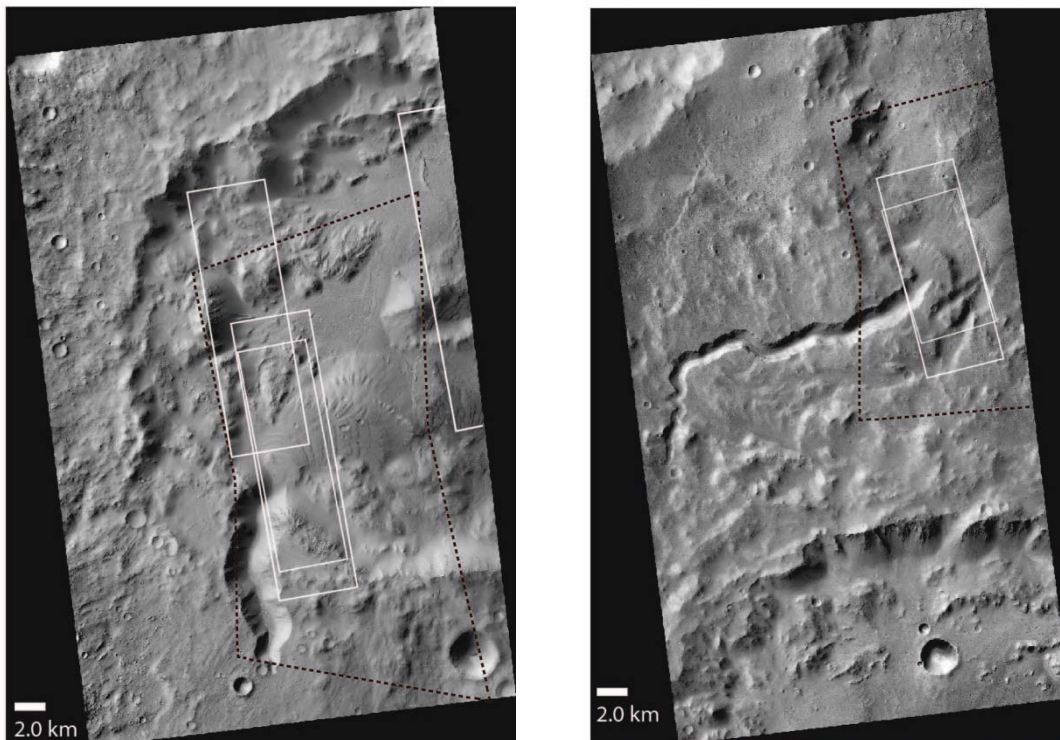


Figure 1. Footprints of HiRISE and spectral data on CTX images in the two study locations, Aeolis Mensae (left) and Subur Vallis (right). White rectangles are HiRISE image footprints centered over the terraced fan which will be used to create DTMs and base map orthoimages. Dashed black lines are hyperspectral CRIISM data footprints. Both locations also have visible and infrared THEMIS coverage (not shown) and adequate CTX regional coverage (>10 images).

GEOLOGIC MAPPING OF VESTA: EARLY RESULTS. R. A. Yingst¹, S. C. Mest¹, D. A. Williams², W. B. Garry³, and D.C. Berman¹, ¹Planetary Science Institute (1700 E. Fort Lowell, Suite 106, Tucson, AZ 85719; yingst@psi.edu); ²Arizona State University; ³NASA Goddard Space Flight Center.

Introduction: The most recent maps of Vesta were created during the active phase of the Dawn Vesta mission, to inform the immediate needs of the Dawn team [e.g., 1-3]. Such mapping represents a first, rapid assessment of gross geology, providing geologic context within a timeframe that allows a map to inform data analysis on a mission timeline. However, revealing the interrelationships of geologic characteristics requires a more comprehensive integration of multiple processes, unit boundaries, information from disparate regions, structures, features and characteristics to be adequately addressed. We are constructing a global geologic map of Vesta at 1:300,000-scale for mapping and digital publication, and 1:1,500,000-scale for the print version. Compared to previous maps, this map will incorporate available, calibrated elemental and mineralogical data.

Geologic Setting: Vesta is an ellipsoidal asteroid of approximately 286 km long axis [4]. Earth-based and Hubble Space Telescope data suggested it had sustained large impacts, including one that produced a large crater at the south pole. Measured and inferred mineralogy results indicated that Vesta has an old, differentiated surface, with spectrally-distinct regions that can be geochemically tied to the HED meteorites [5-7]. Dawn data confirmed that Vesta has a heavily-cratered surface, with large craters evident in numerous locations. The two largest impact structures resolved are the degraded Veneneia crater, and the younger, larger Rheasilvia crater, both located near the south pole. Vesta's surface is also characterized by a system of deep troughs and ridges. Notwithstanding previous spectroscopic observations, no volcanic features have been unequivocally identified.

Data: The Dawn Framing Camera (FC) Low-Altitude Mapping Orbit (LAMO) images constitute the basemap. The Digital Terrain Model (DTM), derived from High-Altitude Mapping Orbit (HAMO) FC stereo data of 93 m/pxl horizontal resolution [8], provides topography, while DTM-derived slope and contour maps yield the shape of the surface and assist in evaluating the extent of geologic materials and features. High-resolution, calibrated spectroscopic data obtained by the Dawn VIR and Dawn Gamma Ray-Neutron Detector Spectrometer (GRaND) allow compositional and elemental information about Vesta's surface materials to be evaluated. VIR provides spectral data in the visible and near infrared wavelengths. GRaND yields abundances for rock-forming elements (O, Si, Fe, Ti, Mg, Al and Ca), radioactive elements (K, U and Th),

trace elements (Gd and Sm), and H, C and N (major constituents of ices).

Mapping Procedure: We began by following the methods developed and described by [10-13]. Units were initially defined and characterized based on morphology, surface textures, and albedo. We are using color data from the FC (and later VIR) to refine unit boundaries where the morphologic characteristics provide more than one possible interpretation, or the interpretation of the unit type is ambiguous. Where unit boundaries are obscured by subsequent geologic activity (typically through emplacement of impact ejecta, or through vertical or lateral mixing of the surface regolith), ejecta from craters that post-date the activity may be used as a proxy for the unmodified composition of the unit (e.g., lunar dark halo and other craters). Craters down to 2 km diameter are also being mapped and classified based on preservation state and the presence and distribution of ejecta, rim, and floor units.

Progress: The initial mapping linework (Figure 1), shows a variety of structures, geocontacts, and crater locations. Important potential units outlined by this linework include heavily-cratered, presumably ancient terrain, and hummocky and curvilinear trough terrain associated with the Rheasilvia impact structure. Heavily-cratered surfaces contain a range of crater morphologies. Small fresh craters, are characterized by sharp-crested, narrow rims and bowl shapes; larger fresh craters have flat floors and may display slumping of rim walls, some finer-textured floor fill, or visible ejecta material. Degraded craters have subdued but distinct continuous rims and varying internal shapes. A large percentage of the heavily-cratered terrain is intersected by two series of ridges and troughs (near the equator and to the north); further mapping and data analysis will determine whether this dissected terrain should be mapped as a standalone unit or not.

The Rheasilvia formation is characterized by (a) bounding arcuate scarps; (b) a central mound with smoother, less cratered regions; (c) a linear set of ridges and troughs running through either side of the central mound; and (d) a more arcuate set swirling out from and around the central mound.

Unit Definition: Defining the boundary criteria for rock units on a small, airless, rocky body has its own particular challenges. Where the primary geologic process for the bulk of a body's history is impact cratering, traditional approaches to mapping can be inadequate, because the difference in morphological characteristics among the various cratered surfaces can be

subtle to absent. For Vesta, as for many such bodies, the surface morphology is muted by the physical and mechanical properties of the regolith. Our approach at this stage has been to be conservative in choosing definite versus approximate boundaries. If we detected a boundary either structurally, topographically, or by changes in the smoothness or level of cratering of a surface, we considered this a potential boundary to be noted. If we did not have confidence in being able to clearly define the morphological distinction between one unit and another, an approximate boundary was used. Further, even if the topography indicated the presence of a boundary, but the morphology did not, an approximate boundary was utilized.

We continue to debate other issues relevant to small, airless bodies. For example, in many cases ejecta mantles but does not bury ancient cratered terrain. It is not clear how this ejecta should be mapped. As another example, there are a number of “colors” in the FC data that might or might not indicate unique compositions (e.g., light teal ejecta, darker mantling, orange material). While we do not use these data to define units, the information must be taken into account in interpretation. However, it is currently unclear at what point these “colors” should be used to refine boundaries. The fundamental question is which is more important to this effort - the definition of the rock body boundaries, or the definition of the rock body boundaries as expressed on the surface.

Future work: Once our first draft is complete, we will overlay VIR 1 μm and 2 μm band depth and posi-

tion data, to better understand the relationships between the unit boundary map and potential VIR compositional information. For those units where portions of the boundary are unsure, we will determine whether the color and/or multispectral data can clarify which is the more accurate interpretation of the morphologic data. Lastly, upwards of 10,000 craters 1 km diameter and above have been cataloged as a preliminary step to utilizing them for crater dating statistics.

References: [1] Yingst, R.A., et al. (2012) LPSC, abs. 1359. [2] Williams, D.A., et al. (2014), *Icarus*, 244, 1-12. [3] Yingst, R.A., et al. (2014) *Planet. Space Sci.*, <http://dx.doi.org/10.1016/j.pss.2013.12.014>. [4] Russell, C.T. et al. (2012) *Science*, 684–686, <http://dx.doi.org/10.1126/science.1219122>. [5] Binzel, R.P. et al. (1997) *Icarus*, 128, 95-103. [6] Gaffey, M.J. (1997) *Icarus*, 127, 130-157. [7] Li, L. et al. (2010) *Icarus*, 208, 238-251. [8] Jaumann, R., et al. (2012) *Science*, 336, 687-690. [9] Preusker, F. et al. (2012) LPSC, abs. 2012. [10] Shoemaker, E.M. and Hackman, R.J. (1962) *The Moon*, Kopal, Z., Mikhailov, Z.K. (Eds.), Internat. Astronomical Union Symposium 14, Academic Press, London, UK, pp. 289–300. [11] Wilhelms, D.E. (1990) *Planetary Mapping*, Greeley, R. and Batson, R.M. (Eds.), Cambridge Univ. Press, pp. 208–260. [12] Tanaka, K.L. et al. (2010) *The Planetary Geologic Mapping Handbook*, USGS Open File Report, 21 pp. [13] Greeley, R. and Batson, R.M. (1990) *Planetary Mapping*, Cambridge Univ. Press, p. 296.

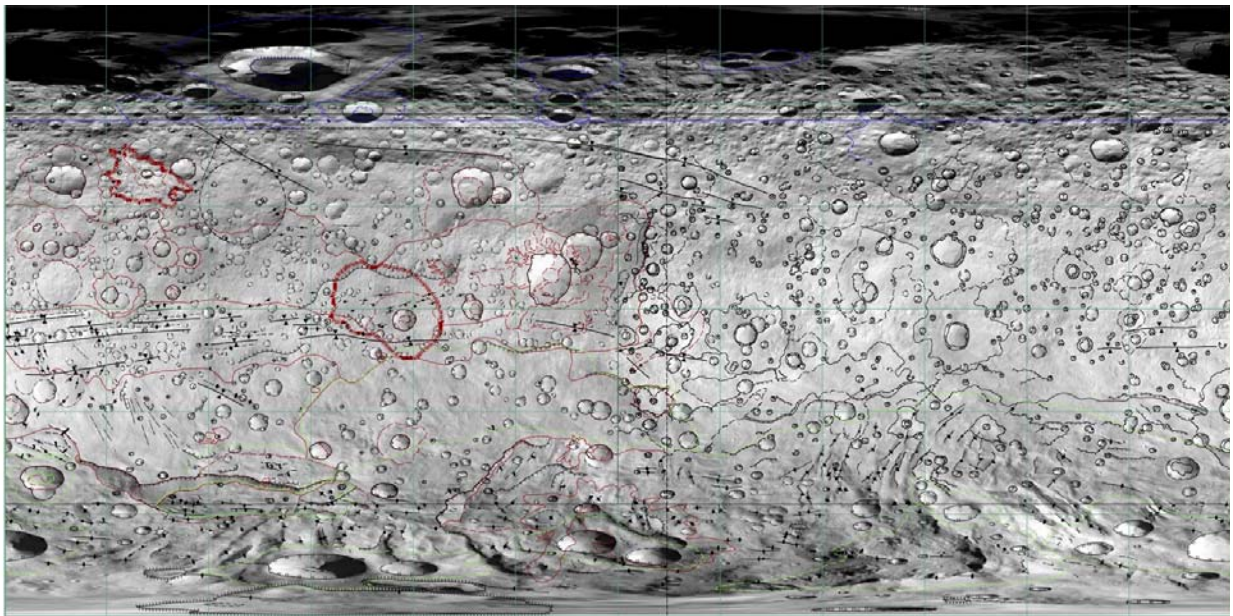


Figure 1. Preliminary linework for global map of Vesta.